

INFORMATION TO USERS

This manuscript has been reproduced from the microfilm master. UMI films the text directly from the original or copy submitted. Thus, some thesis and dissertation copies are in typewriter face, while others may be from any type of computer printer.

The quality of this reproduction is dependent upon the quality of the copy submitted. Broken or indistinct print, colored or poor quality illustrations and photographs, print bleedthrough, substandard margins, and improper alignment can adversely affect reproduction.

In the unlikely event that the author did not send UMI a complete manuscript and there are missing pages, these will be noted. Also, if unauthorized copyright material had to be removed, a note will indicate the deletion.

Oversize materials (e.g., maps, drawings, charts) are reproduced by sectioning the original, beginning at the upper left-hand corner and continuing from left to right in equal sections with small overlaps.

Photographs included in the original manuscript have been reproduced xerographically in this copy. Higher quality 6" x 9" black and white photographic prints are available for any photographs or illustrations appearing in this copy for an additional charge. Contact UMI directly to order.

**Bell & Howell Information and Learning
300 North Zeeb Road, Ann Arbor, MI 48106-1346 USA
800-521-0600**

UMI[®]

**SUBSURFACE STRUCTURE OF THE VOLCANOES IN KATMAI NATIONAL
PARK, ALASKA**

A

THESIS

Presented to the Faculty

of the University of Alaska Fairbanks

in Partial Fulfillment of the Requirements

for the Degree of

DOCTOR OF PHILOSOPHY

by

Arthur D. Jolly, B.S., M.S.

Fairbanks, Alaska

December 2000

UMI Number: 9992688

UMI[®]

UMI Microform 9992688

Copyright 2001 by Bell & Howell Information and Learning Company.

**All rights reserved. This microform edition is protected against
unauthorized copying under Title 17, United States Code.**

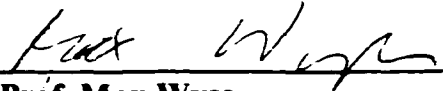
**Bell & Howell Information and Learning Company
300 North Zeeb Road
P.O. Box 1346
Ann Arbor, MI 48106-1346**

**SUBSURFACE STRUCTURE OF THE VOLCANOES IN KATMAI NATIONAL
PARK, ALASKA**

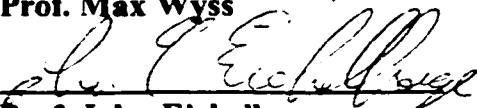
by

Arthur D. Jolly

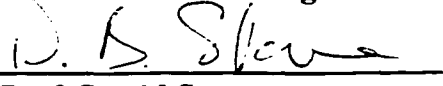
RECOMMENDED



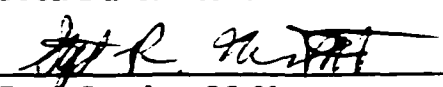
Prof. Max Wyss



Prof. John Eichelberger

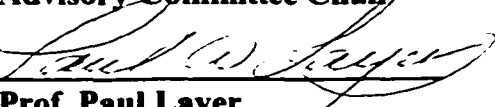


Prof. David Stone



Prof. Stephen McNutt

Advisory Committee Chair



Prof. Paul Layer

Department Head

APPROVED



Prof. David Woodall

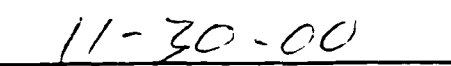
Dean, College of Sciences,

Engineering and Mathematics



Prof. Joseph Kan

Dean of the Graduate School



Date

Abstract

The three-dimensional velocity, attenuation and b -value structure is mapped beneath the Katmai group volcanoes, located in south-central Alaska. Data for these studies include 4320 earthquakes recorded in the period July 26, 1995 to November 30, 1999 on a 5-18 station short-period seismograph array.

The velocity structure is determined by inversion of P-wave travel-times for 8041 rays from 815 earthquakes. The inversion revealed the lowest velocities (3.6-5.0 km/s) centered beneath Novarupta, Trident and Mageik volcanoes between the surface and 4 km below sea level and moderately lower velocities at 0-6 km depth between Martin volcano and Katmai caldera (4.5-6.0 km/s). Higher relative velocities (5.0-6.5 km/s) prevail outboard of the volcanic axis and at Griggs volcano.

The attenuation structure is determined by inversion of the amplitude spectra roll off to obtain t^* for 1301 rays from 230 earthquakes in the magnitude range ($0.8 < M_L < 1.8$). The inversion, which is well constrained in the depth range 0-6 km, reveals higher attenuation along the volcanic axis $1/Q = 0.008-0.018$ ($55 < Q < 125$) and lower attenuation in non-volcanic regions of the study area $1/Q = 0.01-0.000$ ($100 < Q < \infty$). The attenuation is greatest beneath Mageik, Trident and Novarupta ($1/Q = 0.018$; $Q = 55$) between the surface and 6 km below sea level.

Frequency-magnitude distributions are determined by mapping b -values for ~1300 earthquakes larger than the magnitude of completeness ($0.7 M_L$). The analysis reveals high b -values at Mageik volcano (1.2-2.2), intermediate b -values at Martin (1.0-1.6) and Katmai caldera (1.2-1.4) and low b -values at Trident (0.6-1.2).

Results point to the existence of a large region of partially molten rock centered beneath Mageik, Novarupta and Trident volcanoes at 0-4 km depth. The localized nature of the high b -value zone at Mageik volcano suggests that the magma is discontinuous, occurring as several distinct bodies. The deeper high attenuation anomaly might mark the now solidified but highly fractured plumbing system associated with the 1912 Novarupta eruption.

Table of Contents	
Abstract	iii
Table of Contents	v
List of Figures	ix
List of Tables	xiii
Acknowledgements	xiv
Chapter 1	
1.0 Introduction	1
1.1 Data	4
1.2 Thesis outline	7
1.3 Breakthroughs and results	7
1.4 References	9
Chapter 2	
2.0 Abstract	11
2.1 Introduction	12
2.2 Theory	15
2.3 Methods	17
2.3.1 Starting model	18
2.3.2 Selection of the damping parameter	19
2.3.3 Resolution and errors	21
2.4 Procedural outline	23
2.5 Inversion results	26

2.6 References	41
Chapter 3	
3.0 Abstract	45
3.1 Introduction	46
3.2 Theory	48
3.2.1 Attenuation measurement (t^*)	49
3.2.2 Inversion	50
3.3 Methods	51
3.3.1 Instrument and site	54
3.3.2 The source	59
3.4 Data for inversion	70
3.5 Procedural outline	71
3.6 Errors	73
3.7 Results	75
3.8 References	88
Chapter 4	
4.0 Abstract	92
4.1 Introduction	94
4.2 Previous studies	98
4.3 Seismic data 1995-1997	99
4.4 Seismicity	102
4.5 The October 16-25, 1996 swarm	104

4.6 Spatial variations in the frequency-magnitude distribution	107
4.7 Temporal analyses of pre- and post-swarm seismicity	109
4.8 Discussion	113
4.8.1 Interpreting intrusive events	113
4.8.2 Flow law models	118
4.9 Conclusions	122
4.10 References	122
Chapter 5	
5.0 Abstract	130
5.1 Introduction	131
5.2 Frequency-magnitude distribution using 1-D velocity model	132
5.3 Frequency magnitude distribution with a new three-dimensional velocity model	134
5.4 Temporal analysis of <i>b</i>-values and maximum depths of seismicity	139
5.5 Discussion	141
5.6 References	144
Chapter 6	
6.0 Introduction	146
6.1.0 Variations in the frequency-magnitude distribution	147
6.1.1 Velocity in the volcanic environment	148
6.1.2 Attenuation and volcanoes	149
6.2 Integrated analysis	149

6.3 Models for the 1912 eruption	161
6.4 Conclusions	163
6.5 References	164

List of Figures

Chapter 1

Figure 1.1: Location map of study area.	2
Figure 1.2: Katmai seismograph stations.	5
Figure 1.3: Map and cross-section of seismicity in the Katmai region.	6

Chapter 2

Figure 2.1: Map and cross-section for 885 earthquakes for P-wave velocity study.	14
Figure 2.2: Final velocity for layer 1 (-3-0 km).	27
Figure 2.3: Checkerboard resolution (a) and jackknife error (b) maps for layer 1 (-3-0 km).	28
Figure 2.4: Final velocity for layer 2 (0-2 km).	29
Figure 2.5: Checkerboard resolution (a) and jackknife error (b) maps for layer 2 (0-2 km).	30
Figure 2.6: Final velocity for layer 3 (2-4 km).	31
Figure 2.7: Checkerboard resolution (a) and jackknife error (b) maps for layer 3 (2-4 km).	32
Figure 2.8: Final velocity for layer 4 (4-6 km).	33
Figure 2.9: Checkerboard resolution (a) and jackknife error (b) maps for layer 4 (4-6 km).	34
Figure 2.10: Final velocity of layer 5 (6-8 km).	35
Figure 2.11: Checkerboard resolution (a) and jackknife error (b) maps for layer 5 (6-8 km).	36
Figure 2.12: Map and cross-section of relocated hypocenters.	39

Chapter 3

Figure 3.1: Example velocity function for event 98010191003p at station KCE.	52
Figure 3.2: Amplitude spectra for typical earthquake.	53
Figure 3.3: Spectra for event 980217200639.p.	55
Figure 3.4: Site amplification factor for 18 stations of the Katmai network.	56
Figure 3.5: Spectra for event 980217200639.p with site amplification, instrument, and geometric spreading corrections applied.	61
Figure 3.6: Log averaged spectra for earthquakes at given source regions.	63
Figure 3.7: Log averaged spectra for earthquakes at given source regions.	64
Figure 3.8: Grid map of earthquake spectra for depth range of 3 km above sea level to 4 km below sea level.	65
Figure 3.9: Grid map of earthquakes spectra for depth range of 4 km below sea level to 12 km below sea level.	66
Figure 3.10: Stress drop (dyne/cm²) versus corner frequency (Hz) for three earthquakes, 0.8 M_L (top), 1.2 M_L (middle) and 1.8 M_L (bottom).	69
Figure 3.11: Attenuation model for layer 1 (-3.0 to 0.0 km depth).	76
Figure 3.12: Hitcount map (a) and jackknife errors (b) for layer 1, (-3.0 to 0.0 km depth range).	77
Figure 3.13: Attenuation model for layer 2 (0.0 to 2.0 km depth).	78
Figure 3.14: Hitcount map (a) and jackknife errors (b) for layer 2, (0.0 to 2.0 km depth range).	79
Figure 3.15: Attenuation model for layer 3 (2.0 to 4.0 km).	80

Figure 3.16: Hitcount map (a) and jackknife errors (b) for layer 3, (2.0 to 4.0 km depth range).	81
Figure 3.17: Attenuation model for layer 4 (4.0 to 6.0 km).	82
Figure 3.18: Hitcount map (a) and jackknife errors (b) for layer 4 (4.0 to 6.0 km depth range).	83
Figure 3.19: Attenuation model for layer 5 (6.0 to 8.0 km).	84
Figure 3.20: Hitcount map (a) and jackknife errors (b) for layer 5 (6.0 to 8.0 km depth range).	85
 Chapter 4	
Figure 4.1: Index map of the study area in the Alaska Peninsula, south central Alaska, and station map showing the locations of seismic stations used in this study.	95
Figure 4.2: Seismicity map and WSW-ENE cross-section of earthquakes located in the regions between July 27, 1995 and December 31, 1997.	96
Figure 4.3: Space-time plot along the volcanic axis showing seismicity and station use through time.	100
Figure 4.4: Number of events per hour (A), magnitudes (B) and cumulative seismic moment release (C) for October 16-25 Martin-Mageik swarm.	105
Figure 4.5: Earthquake decay vs. time for October 16-25 Martin-Mageik swarm.	106
Figure 4.6: Spatial b-values determined within a cross-section Shown by dashed line in Figure 4.2.	108
Figure 4.7: The b-value vs. time and depth vs. time for pre- and post-swarm seismicity located in the vicinity of Martin-Mageik volcanoes.	110

Figure 4.8: Frequency-magnitude distributions for Martin-Mageik area.	111
Figure 4.9: Shear rock strength (MPa) with depth (km) for brittle and plastic flow.	121
Chapter 5	
Figure 5.1: Map and cross-section of seismicity in the Katmai region.	133
Figure 5.2: Map (a) and cross-section (b) of b-value variation in space for earthquakes located between July 1995 to November 1999.	135
Figure 5.3: Map and cross-section for relocation of earthquakes using the final three-dimensional velocity model.	136
Figure 5.4: Map (a) and cross-section (b) of b-value variation in space for earthquakes located between July 1995 to November 1999.	138
Figure 5.5: Depth versus time and b-value versus time for the period July 26, 1995 to November 30, 1999.	140
Chapter 6	
Figure 6.1: Velocity (a) and attenuation (b) for layer 2 (0.0-2.0 km).	151
Figure 6.2: Velocity (a) and attenuation (b) for layer 3 (2.0-4.0 km).	152
Figure 6.3: Velocity (a) and attenuation (b) for layer 4 (4.0-6.0 km).	153
Figure 6.4: Map of b-value variation in space for earthquakes located between July 26,1995 and November 30,1999.	154
Figure 6.5: Cross-sections along the volcanic axis from Martin to Katmai caldera for velocity (a), attenuation (b), and b-value spatial mapping (c).	155
Figure 6.6: Figure 6.6: Integration of velocity, attenuation, and b-value results for cross-section along volcanic axis.	156

List of Tables

Chapter 2

Table 2.1: New 1-dimensional velocity model for tomography study. 18

Table 2.2: Station corrections for P-arrival times. 19

Table 2.3: Parameter reduction and average model error reduction at selected damping values. 20

Table 2.4: Cumulative chi-squared misfit reduction with iteration number. 37

Chapter 3

Table 3.1: Site amplification correction for each station. 60

Chapter 4

Table 4.1: Velocity model used for locations in the Katmai region (Fogleman et al., 1988). 101

Table 4.2: Summary of seismicity rates b -values and magnitude of completeness. 103

Table 4.3: Steady-state parameters (A , n , H^*) used in flow-law models. 119

Acknowledgements

A thesis has only one author, but could not be completed without the assistance of many people. I would like to thank Steve McNutt, my principal advisor, for his countless hours of assistance, support and friendship. My advisory committee, John Eichelberger, Max Wyss and David Stone, provided additional scientific advice and unwavering support. The Alaska Volcano Observatory under the U. S. Geological Survey-Volcanic Hazards Program funded all phases of this research. Seth Moran provided the code for inversion of the velocity structure and provided sound scientific advice and support. Jonathan Lees and Stefan Wiemer provided the attenuation and *b*-value analysis code respectively. They are gratefully thanked. John Paskievitch, Tim Plucinski, Seth Moran, John Power, Dave Schneider and Eliot Endo worked in the field at Katmai and suffered cold, wind and snow to keep the Katmai network operating. Steve Estes, Guy Tytgat, Mitch Robinson, John Lahr, John Power, Bob Hammond and Chris Stephens provided assistance in the lab. Scott Stihler is especially acknowledged for countless hours of data analysis. I would not have completed this thesis without the support of my friends who encouraged me as I traveled 'down that long and dusty road'. I thank especially Barbara Trost, Pete Stelling, Dorte Mann, Vicky McConnell, Hilary Fletcher, John Power, Dave Covey, Ned Rozell, Martin LeFevers, Michelle Burrell, Stefan Wiemer, Dalia Chatterjee, Jim Clippard, and John Benoit. Finally, I wish to thank my family: Gillian, Cahill, Mom and Dad. This thesis is dedicated to them.

Chapter 1: Introduction

1.0 Introduction

The largest volcanic eruption of the 20th century occurred in the Valley of Ten-Thousand Smokes, Alaska on June 6th-9th, 1912. The event produced $\sim 30 \text{ km}^3$ of eruptive materials (Hildreth, 1983) from a new vent at Novarupta and induced the collapse of Katmai peak about 10 km to the east. The large spatial offset between the eruptive vent and the caldera collapse site requires a magma system of great lateral extent. For this reason the subsurface structures in the vicinity of Novarupta dome and Katmai caldera (Figure 1.1) have been topics of great scientific interest in the past several decades (e.g. Matumoto and Ward, 1967; Kienle, 1970; Matumoto, 1971; Hildreth, 1983; Fierstein and Hildreth, 1992; Ward and others; 1991, Abe, 1992).

The Katmai group of volcanoes is located on the Alaska Peninsula 80 km south east of King Salmon (Figure 1.1). The volcanoes of the group include, from southwest to northeast: Martin, Mageik, Trident, Novarupta, Katmai caldera, Griggs and Snowy volcanoes.

Matumoto and Ward (1967), Kubota and Berg (1967) and Matumoto (1971) were the first to identify variations in the subsurface structure in the Katmai region. They identified regions where S-waves were attenuated. The attenuation was generally greatest in the vicinity of the volcanic axis and at both shallow and mid-crustal depths. At about the same time, Kienle (1970) observed a $\sim 35 \text{ Mgal}$ gravity low located in the vicinity of

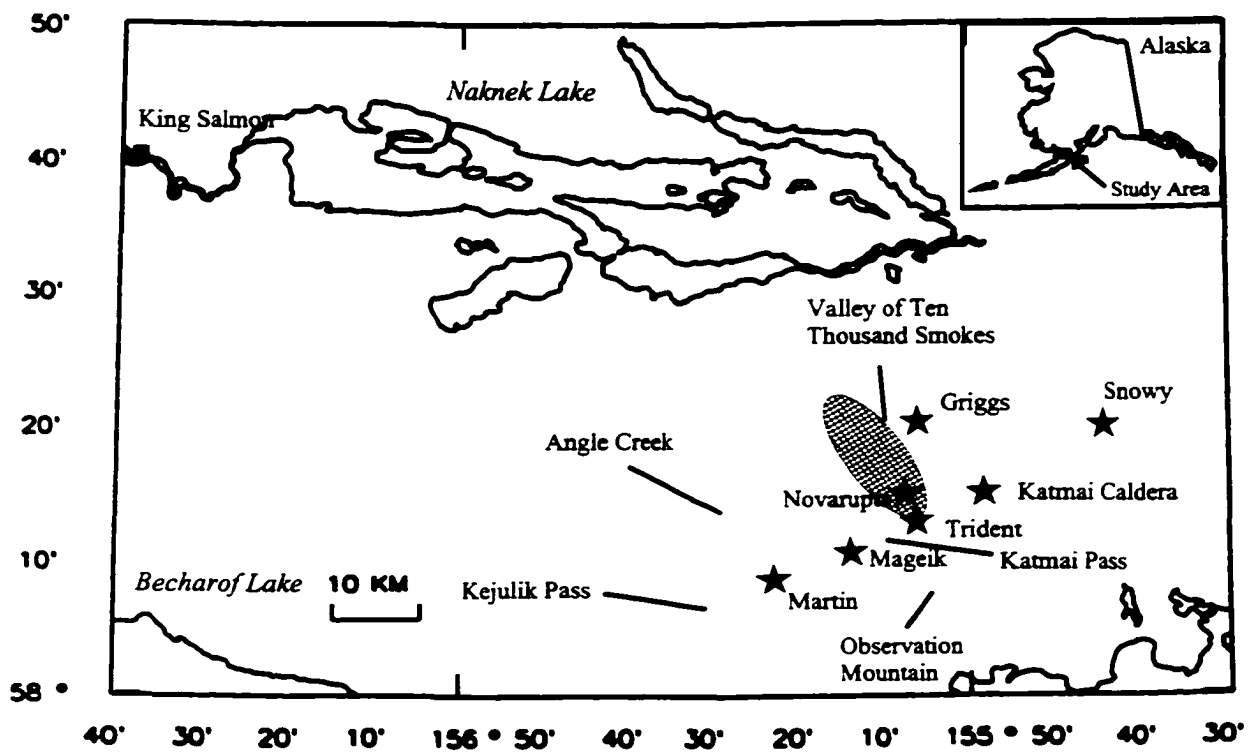


Figure 1.1: Location map of the study area. Volcanoes (stars), and important place names are shown for clarity. Latitude and longitude are in degrees and minutes north and west respectively.

Katmai pass. Saltus et al. (1991) modeled this gravity anomaly as a spherical body centered about 7-9 km below sea level, having a volume of 280 km³ and a density contrast of 500 Kg/m³. Later, Ward et al., (1991) observed significant travel-time delays for a seismograph station south of Katmai pass. These delays were azimuth dependent and were greatest for rays coming from the north of the station. However, the location or extent of the anomaly could not be determined. Recently, Lu et al., (1997) observed an interferometric anomaly near Southwest Trident volcano from Synthetic Aperture Radar (SAR) images acquired between 1993 and 1995. They interpreted the anomaly as being caused by a surface inflation of several centimeters. From the uplift gradient, Lu et al., (1997) inferred a pressure source located 0.8 to 2.0 km below the surface.

These earlier studies suggested that Katmai is a good target for three-dimensional imaging of the subsurface using modern seismological techniques. The present investigation uses three well known techniques (P-wave velocity tomography, P-wave attenuation tomography, and *b*-value spatial mapping) to image the sub-surface structure. Multiple techniques are applied to reduce the inherent ambiguity associated with the interpretation of results from individual methods. The formal thesis, then, is to determine if magma is resident in the subsurface, and if so, to examine its extent and character.

1.1 Data

On July 26, 1995, the Alaska Volcano Observatory began continuously recording data from a 5-station seismograph network resurrected from an existing United States Geological Survey (USGS) network in the Valley of Ten Thousand Smokes (VTTS). This network was further augmented in September 1996 when 6 new stations were added around Martin and Mageik volcanoes. In August 1998 the network was augmented a third time when 7 new stations were added in the northern portion of the network to bring the total network to 18 stations and 24 components (Figure 1.2). The network includes 15 single component short-period instruments with a 1 Hz natural frequency and 3 three-component short-period instruments with a 2 Hz natural frequency. For the period July 26, 1995 to November 30, 1999, 4320 tectonic and volcano-tectonic earthquakes were recorded with magnitudes ranging from -0.5 to $4.5 M_L$ (Figure 1.3).

Upper-crustal seismicity in the Katmai region forms 4 distinct clusters: 1) beneath Martin and Mageik volcanoes, 2) Trident volcano, 3) about 2 km west of Katmai caldera, and 4) about 5 km due west of Snowy volcano. Additional diffuse seismicity occurred along the volcanic axis in an ENE-WSW belt about 20 km in width (Figure 1.3). Earthquake depths were generally shallowest at Trident volcano where seismicity was concentrated above 5 km, and reached seismogenic depths of about 10 km to the northeast near Snowy and to the southwest at Martin. Isolated earthquakes having depths greater than 10 km were also observed. Griggs volcano and Novarupta, site of the paroxysmal 1912 eruption, each had little seismic activity beneath them. Anomalous seismicity at 1.0 km above sea level (Figure 1.2, cross-section) may result from a location artifact associated with the location program HYPOELLIPSE (Lahr, 1989). The artifact is probably caused by earthquakes that were unable to iterate off the -1.0 km initial trial

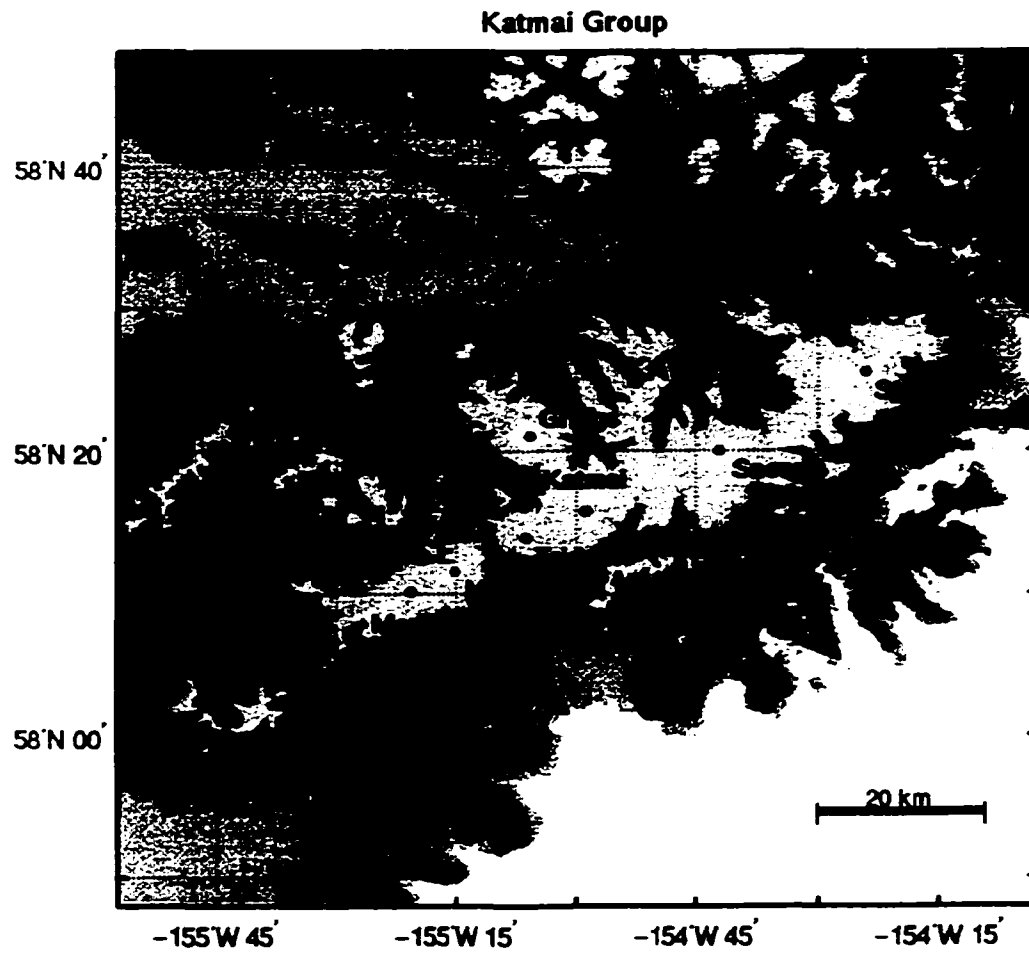
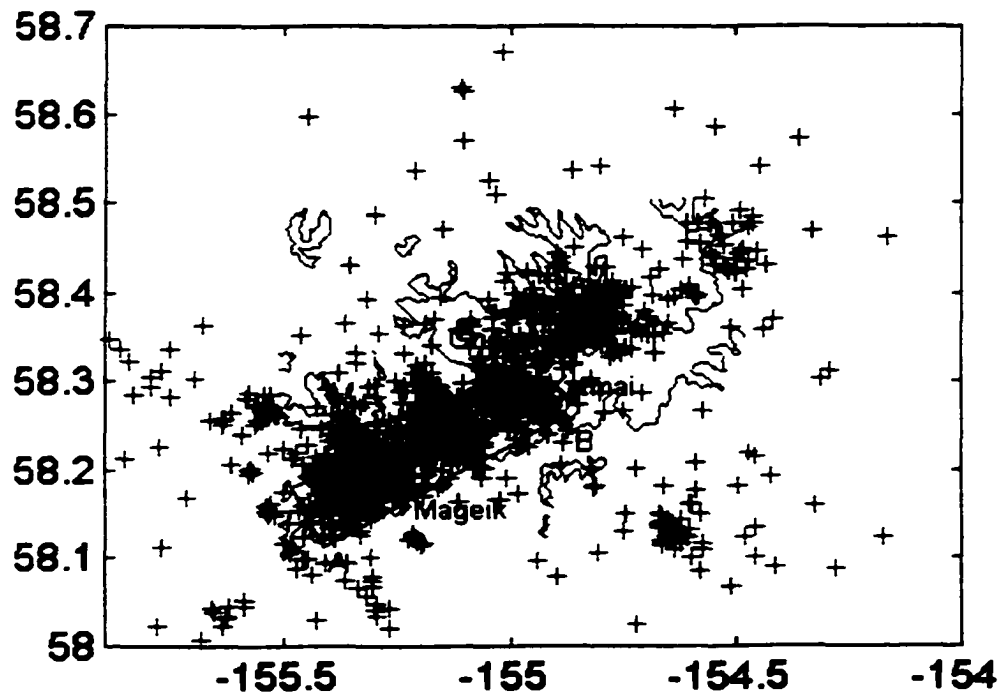


Figure 1.2: Katmai seismograph stations. Small black circles represent volcanoes while large black circles represent seismic stations.

a)



b)

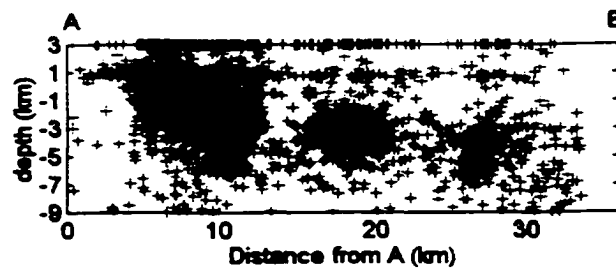


Figure 1.3: Map and cross-section of seismicity in the Katmai region. Seismicity is from the period July 20, 1995 to November 31, 1999. Lines are the 3000 foot elevation contour. The box in (a) is the cross-section projection for (b).

depth. A new velocity model and high quality earthquake locations, eliminate this artifact (Chapter 5).

1.2 Thesis outline

This thesis is presented in 6 chapters including the Introduction (Chapter 1) and the Discussion and Conclusions (Chapter 6). Two chapters are devoted to *b*-value analysis techniques (Chapter 4 and 5) and one each for the P-wave velocity (Chapter 2) and attenuation (Chapter 3). It is noted for clarity that the *b*-value analysis in Chapter 4 was the first study completed because the *b*-value analysis included earthquakes located with as few as 4 local stations (Chapter 4) while the velocity inversion required at least 8 P-wave arrival-times for inclusion. However, the development of the new velocity model provided high quality earthquake locations which might change the *b*-value results presented in Chapter 4. This required a new examination of the *b*-value results using the new earthquake locations and additional data. In Chapter 5, earthquakes are relocated, and compared with the earlier published results (Jolly and McNutt, 1999).

1.3 Breakthroughs and results

This thesis presents new results and methods that are worth specific mention. First, a new method for removing the site amplification factor from each amplitude spectrum is applied (Section 3.3.1). This is the first time that a 'site specific' correction has been applied in a three-dimensional attenuation inversion. In addition, this thesis

presents a new method for examining earthquake spectra at their source regions (Section 3.3.2). This method allows observation of systematic features at the source and proved useful for mitigating the effect of features not related to attenuation in the subsequent inversion.

The principle scientific results of the thesis include the identification of a general low velocity (Sections 2.5 and 6.2), high attenuation (Sections 3.6 and 6.2) region beneath Katmai, Trident, Novarupta, and Mageik volcanoes, and a high b -value region beneath Mageik volcano (Sections 4.6, 5.3 and 6.2). This is the first time that the subsurface structures of Katmai have been mapped for these three parameters. This thesis also provides the first case study in which b -value spatial mapping was determined before and after a full three-dimensional velocity inversion (Sections 5.2 and 5.3). It is thus an important benchmark for studies of this type.

Finally, hazards associated with volcanic eruptions are potentially great, as demonstrated at Mount St. Helens, Pinatubo, and Montserrat. The effects of these hazards might be mitigated via analysis of data acquired during a volcano's quiescent pre-eruptive period. This thesis is important as a hazard mitigation resource because earthquake locations, seismicity rates, swarm decay rates, and static b -value estimates offer a baseline for comparison to future activity. In addition, the three-dimensional tomographic images offer an important indicator of subsurface magma potential and hence the future eruptive potential in the area.

1.4 References

Abe, K., Seismicity of the great eruption of Mount Katmai, Alaska, in 1912, *Bull. Seis. Soc. Amer.*, 82, 175-191, 1992.

Fierstein, J. and Hildreth, W., The plinian eruptions of 1912 at Novarupta, Katmai National Park, Alaska, *Bull. Volcanology*, 54, 646-684, 1992.

Hildreth, W., The compositionally zoned eruption of 1912 in the Valley of Ten Thousand Smokes, Katmai National Park, Alaska, *J. Volc. and Geotherm. Res.*, 18, 1-56, 1983.

Jolly, A.D. and McNutt, S.R., Seismicity at the volcanoes of Katmai National Park, Alaska; July 1995-December 1997, *J. Volc. Geotherm. Res.*, 93, 173-190, 1999.

Kienle, J., Gravity traverses in the Valley of Ten-Thousand Smokes, Katmai National Monument, Alaska, *J. Geophys. Res.*, 75, 6641-6649, 1970.

Kubota, S. and Berg, E., Evidence for magma in the Katmai volcanic range, *Bull. Volcanologique*, 31, 175-214, 1967.

Lahr, J.C., HYPOELLIPSE/Version 2.0: A Computer program for determining local earthquake hypocentral parameters, magnitude, and first motion patterned: U.S Geol. Surv., Open-File Report, 89-116, 89p, 1989.

Lu, Z., Fatland, R., Wyss, M., Li, S., Eichelberger, J., Dean, K., Freymueller, J., Deformation of New Trident Volcano measured by ERS-1 SAR interferometry, Katmai National Park, Alaska, *Geophys. Res. Lett.*, 24, 695-698, 1997.

Matumoto, T. and Ward, P.L., Microearthquake study of Mount Katmai and vicinity, Alaska, *J. Geophys. Res.*, 72, 2557-2568, 1967.

Matumoto, T., Seismic body waves observed in the vicinity of Mount Katmai, Alaska, and evidence for the existence of molten chambers, *Geol. Soc. Amer. Bull.*, 82, 2905-2920, 1971.

Saltus, R.W., Stone, D.B., Kienle, J., and Goodliffe, A.M., New gravity data at Katmai National Park, Alaska, suggest a magma body analogous to that at Geysers-Clear Lake region, California, *EOS Trans., Amer. Geophys. U.*, 429, 1991.

Ward, P.A., Pitt, A.M. and Endo, E., Seismic evidence for magma in the vicinity of Mt. Katmai, Alaska, *Geophys. Res. Letts.*, 18, 1537-1540, 1991.

Chapter 2: P-wave velocity inversion

2.0 Abstract

The three-dimensional P-wave velocity structure beneath the Katmai group volcanoes is determined by inversion of 8041 rays from 815 earthquakes recorded on a local 18 station short-period network. The inversion is well constrained from sea level to about 6-8 km below sea level and encompasses all of the Katmai volcanoes; Martin, Mageik, Trident, Griggs, Novarupta and Katmai.

The inversion, which converged after the 3rd inversion step, reveals a prominent low velocity zone (3.6-5.0 km/s) centered at Katmai pass and extending from Mageik to Trident volcano. The anomaly is about 20-25% slower than velocities outboard of the region (5.0-6.5 km/s). Moderately low velocities (4.5-6.0 km/s) are observed along the volcanic axis between Martin and Katmai caldera. Griggs volcano, located about 10 km behind the volcanic axis, has unremarkable velocities (5.0-5.7 km/s) compared to non-volcanic regions. The highest velocities are observed between Snowy and Griggs volcano (5.5-6.5 km/s). The results yield a 27% reduction in RMS travel-time residual over the standard velocity model.

These results provide evidence in favor of partially molten rock at shallow depth beneath the Mageik-Katmai-Novarupta region. Moderately low velocities beneath Martin and Katmai suggest that old, mostly solidified intrusions exist beneath these volcanoes. Higher relative velocities beneath the Griggs and Snowy vents suggest that no magma is resident in the shallow crust at these volcanoes.

2.1 Introduction

Ray inversion tomography is now a standard tool for identification of velocity anomalies below the Earth's surface. The method was first pioneered in the medical fields to image the interior of the human body (Gilbert, 1972; Houndsfield, 1973) and was later applied in seismology to image the interior of the earth (Aki and Lee, 1976; Aki et al., 1977). High resolution subsurface imaging proved valuable, leading to numerous other tomographic studies with the same general goal: To determine the variation of a property (in this case the P-wave velocity) within a volume, through an analysis of the integral of that property along each of many ray-paths.

Volcanoes provide good targets for tomographic studies because magma is likely beneath active and recently active volcanic systems. This magma should have fundamentally different elastic properties than the surrounding rock. As an example, the P-wave velocity, α is given by

$$\alpha = [(\kappa + (4\mu/3))/\rho]^{1/2} \quad 2.0$$

where κ is the bulk modulus, μ is the rigidity or shear modulus, and ρ is the density.

Equation 2.0 shows that the presence of liquids, which do not support shear, and a reduction in the shear modulus μ , will produce a reduction in the elastic wave velocity.

Thus, the velocity in partially melted rock should be slower than the velocity in un-melted

rock of the same composition (Mavco, 1980). For this reason, observed low velocity zones beneath volcanic regions are commonly ascribed to the presence of magma (Lorenzen, 1994; Benz et al., 1996; Power et al., 1998).

Katmai is a good target for tomographic study. The region produced the largest eruption of the 20th century at Novarupta, and numerous smaller eruptions from Trident volcano. The area exhibited strong S wave attenuation along the volcanic axis (Matumoto, 1971) and a strong low velocity anomaly centered at Katmai pass (Ward et al., 1991). The latter is approximately coincident with a -35 Mgal gravity low (Kienle, 1970) and localized uplift (Lu et al., 1997) found using SAR interferometry. These independent lines of evidence point to Katmai as a region that might hold magma at shallow depths.

In this study, the travel-time residuals for 885 local earthquakes (Figure 2.1) were available for inversion to determine the three dimensional velocity structure at the Katmai group of volcanoes (Martin, Mageik Trident, Novarupta, Katmai, Griggs, and Snowy). These events had at least 8 P-phases for the earthquake location, an azimuthal gap of less than 180 degrees and the nearest station within 15 km of the earthquake. S-phases were not used for the earthquake location process. In subsequent inversion steps the selection criteria were reapplied, thus the number of events and rays available for an inversion step was variable. This study uses the algorithm of Moran (1997), which was modified from an original algorithm by Lees (1989). Moran's (1997) improvements to the original computational methods include: 1) the ability to trace rays above sea level, 2) application of an annihilation operator to the parameter separation technique (Spencer

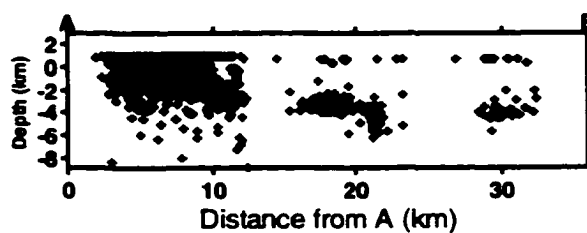
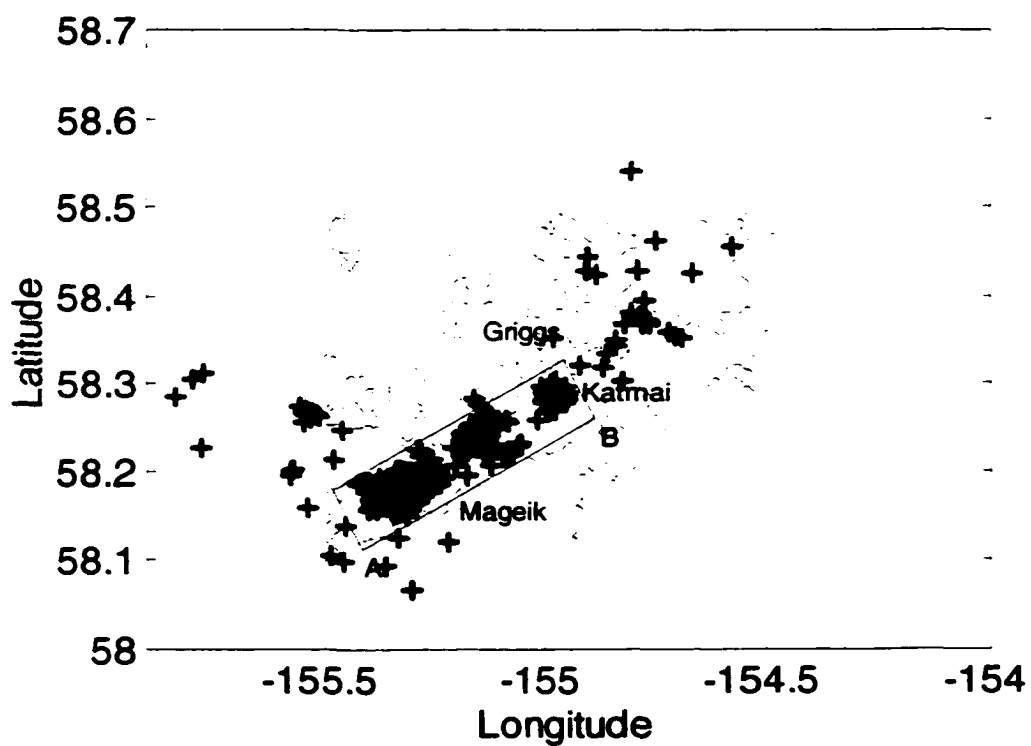


Figure 2.1: Map and cross-section for 885 earthquakes for P-wave velocity study. The earthquakes needed 8 or more arrival times, an earthquake to station azimuthal gap of less than 180 degrees and a nearest station within 15 km.

and Gubbins, 1980 and Pavlis and Booker, 1980) to further mitigate errors associated with earthquake mis-locations and 3) improved methods for projecting the latitude, longitude, depth pairs into xyz coordinates. The techniques of this thesis closely follows Moran's (1997).

2.2 Theory

The travel-time of a ray in the earth can be represented by the path integral

$$t(E,R) = \int_{L(E,R)} S(x,y,z)dl, \quad 2.1$$

where t is the travel-time, L is the path length between the earthquake E and the receiver R , and $S(x,y,z)$ is the slowness (reciprocal velocity) of the medium along a path segment dl . The equation is non-linear because the raypath and earthquake location are dependent on the unknown slowness. The problem is linearized by assuming that the actual slowness S is close to a reference slowness S_o

$$\Delta S = S - S_o. \quad 2.2$$

Then a travel-time t can be estimated from the reference slowness and compared to the observed travel-time t_o , producing a travel-time residual

$$\Delta t = t - t_o. \quad 2.3$$

The form of the path integral then becomes

$$\Delta t(E,R) = \oint_{Lo(E,R)} \Delta S(x,y,z) dl_o. \quad 2.4$$

where Δt is a travel-time residual, and ΔS is a departure in slowness from a reference slowness for a segment of the ray dl_o . The problem is then linear because raypath is known relative to the reference model.

Consider, next, a multitude of rays traversing a region. If the velocity is anomalously slow in some part of that region (relative to the reference velocity model), then rays which traverse the anomaly will have longer travel-times t , and by Equation 2.3, positive travel-time residuals Δt . This system of equations can be solved by means of a matrix inversion

$$r = C \cdot S, \quad 2.5$$

where r is a vector of travel-time residuals Δt , C is a matrix of ray lengths dl_o , and S is a vector of unknown slowness values. In practice, the region of interest is subdivided into numerous blocks, then earthquakes are located and the rays are traced through each block as a forward problem. Travel-time residuals and ray lengths are calculated for each block and these data are inverted using Equation 2.5 to produce a new slowness model.

Further, the new model can be used to relocate the earthquakes and trace a new set of rays and theoretical travel-times. By multiple iterations, the non-linear inversion is reduced to a series of linear inversions for the velocity. This is the generalized goal of this study.

2.3 Methods

Equation 2.5 can be solved using various mathematical schemes, the most common of which is the method of damped least squares.

$$S^* = (C^T C + \lambda^2 I)^{-1} C^T r, \quad 2.6$$

where S^* is the model parameter estimate and λ is the damping parameter. Direct solution of Equation 2.6 is unrealistic for large matrix systems. As a result, a host of approximate inversion methodologies have been developed. This study uses the LSQR method (Paige and Saunders, 1982a and 1982b) to determine an approximate solution to the matrix system in Equation 2.5. The method offers strong computational advantages over direct inversion methods like Singular Value Decomposition (Press et al., 1996), but does not provide a method of determining model resolution and errors. This shortfall is traditionally overcome via empirical reconstruction of synthetic anomalies, called “checkerboards” (Humphreys and Clayton, 1988) and subset re-sampling, called “jackknife” (Lees, 1989).

Ray tracing represents a second important aspect in the tomographic method. This study uses an approximate ray-tracing method developed by Um and Thurber (1987). This method assumes that the ray origin and end points are known and that the velocity function is smooth and differentiable. The technique offers a fast approximation of the raypath by iteratively defining a set of mid-points along a ray segment, and perturbing the location of the mid-points based on the velocity gradient. Successive

iterations yield more ray segments and refined ray trajectories until the traveltimes are minimized within an established criterion.

2.3.1 Starting model

Earthquakes in the Katmai region were initially located using the program HYPOELLIPSE (Lahr, 1989) and the southern Alaska regional velocity model (See Chapter 4; Table 4.1) (Fogleman, 1988). This model was used by Ward et al., (1991) to locate seismicity occurring between September, 1987 and December, 1990, and is the standard model for earthquake locations at Katmai. To assess the validity of this starting model, 394 well recorded shocks from the period August 1997 and October 1998 were selected. For these events, the layer boundaries and velocities were perturbed while monitoring the average RMS residual. The best model determined from this forward method had P-wave velocities as summarized in Table 2.1.

For data used in the inversion, the new model reduced the RMS residual from 0.18 seconds to 0.15 seconds, a reduction of 16%. Next the earthquakes were relocated and station corrections determined. The final one-dimensional locations had station corrections as summarized in Table 2.2.

Table 2.1: New 1-dimensional velocity model for tomography study. Positive depths are below sea level and the top of the model is 3 km above sea level. HS is a half-space.

Layer	Velocity (km/sec)	Layer boundary (km)
1	5.0	0.0
2	5.3	3.0
3	5.6	5.0
4	5.9	7.0
HS	6.1	9.0

Table 2.2: Station corrections for P-arrival times.

<u>STATION</u>	<u>P-DELAY</u>	<u>STATION</u>	<u>P-DELAY</u>
ACH	-0.09	KARR	0.39
ANCK	-0.05	KAWH	0.08
CAHL	-0.09	KBM	-0.04
CNTC	0.46	KCE	0.21
KABR	-0.08	KCG	0.00
KAHC	0.54	KEL	0.28
KAHG	0.43	KJL	-0.04
KAIC	0.23	KVT	-0.03
KAPH	0.93	MGLS	-0.12

2.3.2 Selection of the damping parameter

The least squares problem of Equation 2.7 is further parameterized by the addition of smoothing L , damping λ , and weighting W parameters to the matrix system (Equation 2.6), giving

$$\begin{bmatrix} WC \\ \lambda L \end{bmatrix} \delta B = \begin{bmatrix} W\delta t \\ 0 \end{bmatrix}. \quad 2.8$$

The smoothing parameter, L , is called the 2-D Laplacian operator that applies nearest neighbor smoothing in two dimensions. The event weighting matrix, W , is applied based on both the arrival time pick quality and earthquake-station distance. The latter weighting scheme improved the inversion of local upper-crustal seismicity in the

tomographic analysis of the greater Mt. Rainier area (S. Moran, personal communication, 2000).

The damping parameter λ , the final constraint, adds model smoothing. If λ is large, then more weight will be given to the constraint equations relative to the data. If λ is small then greater weight is given to the data. Highly damped inversions vary little from the starting model but also yield little residual reduction. Alternatively, underdamped inversions yield highly variable models, including data errors, and have high residual reductions.

The selection of λ is very important and, as the discussion above implies, is a great source of ambiguity. The selection of the 'best' model must balance model errors against residual reduction in a meaningful way. This study uses an analysis of the tradeoff between the damping parameter and the amount of error reduction for the linear inversion (Table 2.3) to determine the 'correct' damping.

Table 2.3: Parameter reduction and average model error reduction at selected damping (λ) values.

damping (λ)	χ^2 reduction(%)	model error (km/s)
25	38.60	0.13
50	37.85	0.12
100	36.78	0.10
125	36.20	0.10
150	35.67	0.08
200	34.43	0.06
400	29.54	0.03
800	23.61	0.02

For several trial λ values, model error and associated residual reduction was monitored. Model errors were monitored via the jackknife method (Lees, 1989) and the residual reduction was monitored via the combined misfit of data δt and model constraints L, W and λ , which are lumped into a measure of parameter reduction (Equation 2.8) called chi-squared (χ^2).

$$\chi^2 = \left[\left[\frac{WC}{\lambda L} \right] \delta B - \left[\frac{W\delta t}{0} \right] \right]^2 \quad 2.9$$

In the end, a damping of $\lambda = 125$ was selected as the optimal value. This value provided a 36% chi-squared misfit reduction in the linear inversion with average model errors of about 0.1 km/s. It is important to note, however, that the strongest velocity anomalies interpreted here were successfully resolved at a wide variety of damping values and so the inversion results are considered robust.

2.3.3 Resolution and errors

This study used the checkerboard (Humphreys and Clayton, 1988) and jackknife (Lees, 1989) methods as indicators of the resolution and errors associated with the inversion. The resolution of data is controlled by raypath distribution, model parameterization, and smoothing (Moran, 1997). Raypath distribution is critical to resolution of anomalies, as blocks which are not hit by rays will not be used in the inverse problem, while blocks with many rays traversing from many directions will be well constrained. The model parameterization provides a measure of the resolving capabilities

of the interpreted blocks. For example, a 1-km anomaly will not be successfully imaged in a 10-km by 10-km block inversion, and highly smoothed inversions cannot resolve structures the scale of the minimum block size. This is because high λ 's yield highly smoothed inversions that may miss strong velocity contrasts.

The checkerboard procedure used here involves defining many spiked regions with 10% variability in the velocity structure (compared to the one-dimensional reference model), and calculating a new set of travel-times through this hypothetical velocity structure. Using these new travel-times, the data are inverted for the slowness structure. The resulting inversion indicates the ability of the existing ray coverage to reproduce the hypothetical velocity structure. Well-resolved regions of the model will retain the structure of the many spikes model, while in poorly resolved regions, the anomalies will become smeared out and the hypothetical structure will become incoherent.

The variance of the inversion is controlled by errors in the data including mis-picks and incorrectly determined raypaths. Mis-picks also result in mis-located earthquakes, an important problem which is mitigated in both the earthquake relocation and the data filtering processes. A common measure of the variance is given by the jackknife method. In this method, the data set is cut into k subsets, each containing $(n - n/k)$ earthquakes. An inversion is completed on each subset and the standard deviation in each slowness block is determined. For blocks traversed by many rays having well described characteristics the standard deviations of the inversions are small and the blocks are well determined. For poorly sampled blocks, or blocks with highly variable travel times, the standard deviations are large.

One drawback to the jackknife inversion method is that it is only useful for estimating errors in a linear inversion (Moran, 1997). To estimate the errors of a full non-linear inversion, one must compute k^m jackknife models where m is the number of steps to complete the inversion. For example, if you wished to find an estimate of the errors associated with the fifth iteration of a non-linear inversion, and you separated the model into 20 jackknife models, then you would need to compute $20^5 = 3200000$ inversions and average the results. To attempt such an analysis is unrealistic and is not completed in this study. For this study, and others, the jackknife errors are determined for the linear inversion. This error estimate represents an approximate measure of the errors of the whole non-linear inversion under the assumption that errors of the linear inversion are of the same order as the errors of subsequent inversion steps.

2.4 Procedural outline

The following outline provides the method used in this inversion study. The procedures follow closely those of Moran (1997) and include:

- 1) Select earthquakes for inversion.
- 2) Select subset of high-quality events for forward modeling.
 - 2a) Iteratively perturb layer boundaries and velocities from top of model downward while monitoring average RMS.
 - 2b) Select best one-dimensional velocity model based on minimum average RMS.

- 3) Relocate all earthquakes in best one-dimensional model and compute station corrections.
 - 3a) Fix old locations and compute residuals in reference one-dimensional model.
 - 3b) Compute P-wave station corrections for all recording stations.
 - 3c) Relocate earthquakes with new station corrections.
 - 3d) Repeat step 3b and 3c until station corrections stop changing.
- 4) Compute final locations in one-dimensional model using station corrections of step 3.
- 5) Perform initial inversion for velocity parameters.
 - 5a) Re-compute travel-time residuals without station corrections and using locations derived in step 4.
 - 5b) Remove all raypaths outside study area.
 - 5c) Remove all events outside the initial selection criteria of step 1.
 - 5d) Invert the data for new velocity model.
- 6) Select damping parameter based on trade-off analysis.
- 7) Redo step 5 at the selected damping parameter.
- 8) Perform next inversion step.
 - 8a) Relocate the earthquakes using prior inversion model.
 - 8b) Trace rays and calculate new residuals using inversion model.
 - 8c) Invert for new velocity model.

- 8d) Monitor resultant model and misfit reduction. If models stop changing and misfit reduction is minimized then go to step 9, otherwise repeat step 8a.
- 9) Select the final model and estimate resolution and errors using checkerboard and jackknife methods.

2.5 Inversion results

Nine iterations for the velocity structure were completed on the data. For each model, the reduction in the chi-squared misfit (χ^2) was monitored (Table 2.4). The model selected for interpretation (Figure 2.2-2.11) and further study was iteration step 5. This inversion step included 8041 rays from 815 earthquakes and had the lowest misfit reduction of all models (Table 2.4). It is noted, however, that this inversion step is not significantly different from prior or following inversion steps, and the interpretation and subsequent analysis would not change with use of another step. The final model (iteration 5) yielded an average RMS travel-time residual of 0.13 s. This is a reduction of 13 % over the best one-dimensional velocity model (Table 2.1) which had an average RMS of 0.15 seconds, 27 % reduction in the average RMS compared to the one-dimensional model used in standard processing (Table 4.1). Tomographic results for the final model (iteration 5) are shown in Figures 2.2, 2.4, 2.6, 2.8 and 2.10. In addition, for each layer, the associated jackknife and checkerboard tests are shown (Figure 2.3, 2.5, 2.7, 2.9, and 2.11).

Checkerboard and jackknife analysis (Figure 2.3, 2.5, 2.7, 2.9 and 2.11) are used as a basis to interpret the tomographic results at Katmai. The interpretation is limited to regions with adequate reconstruction of the many-spikes model and lower than average model errors (< 0.1 km/sec). In the depth range 0-2 km (Figure 2.4), the velocity structure is interpretable in a 20-30 km swath between Martin volcano and Trident

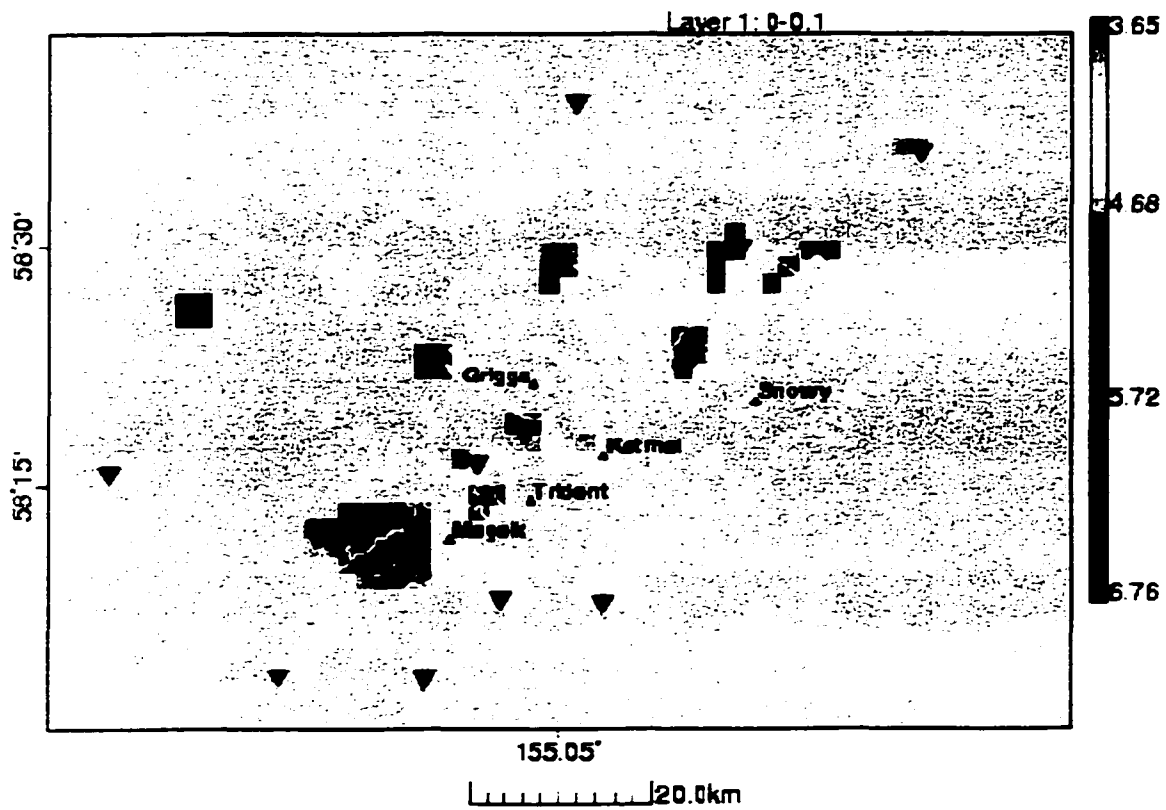
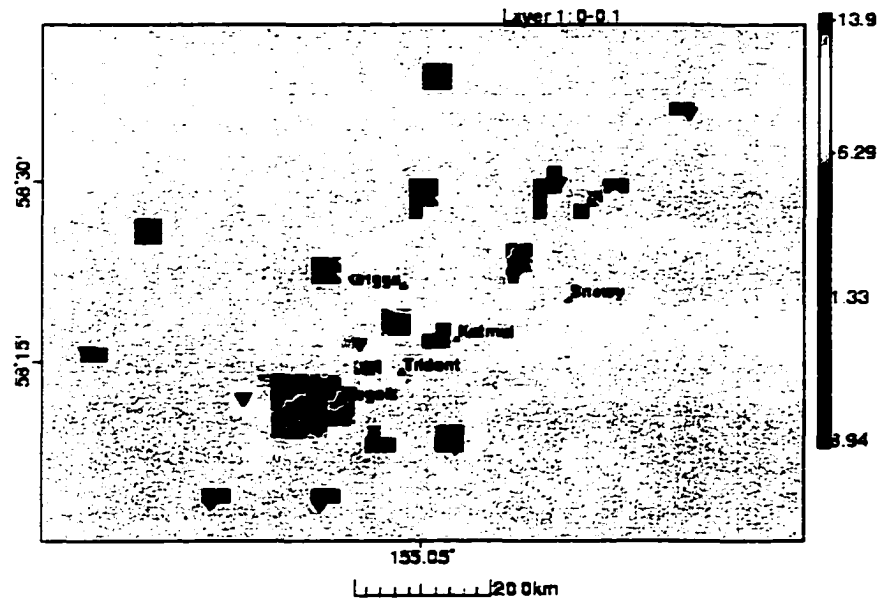


Figure 2.2: Final velocity for layer 1 (-3-0 km). Color scale is in km/s.

a)



b)

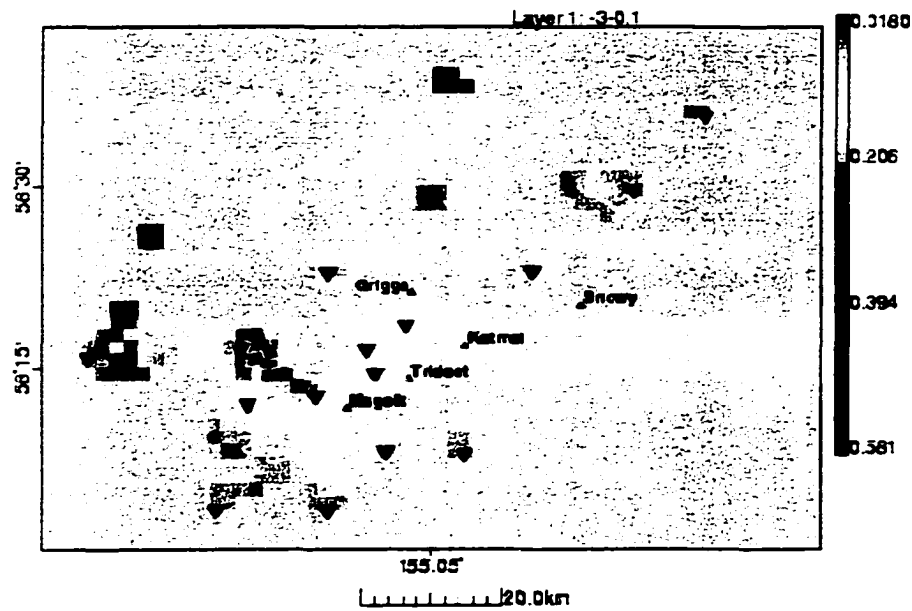


Figure 2.3: Checkerboard resolution (a) and jackknife error (b) maps for layer 1 (-3-0 km). The color scale for checkerboard is % velocity (a) and velocity (b) in (km/s).

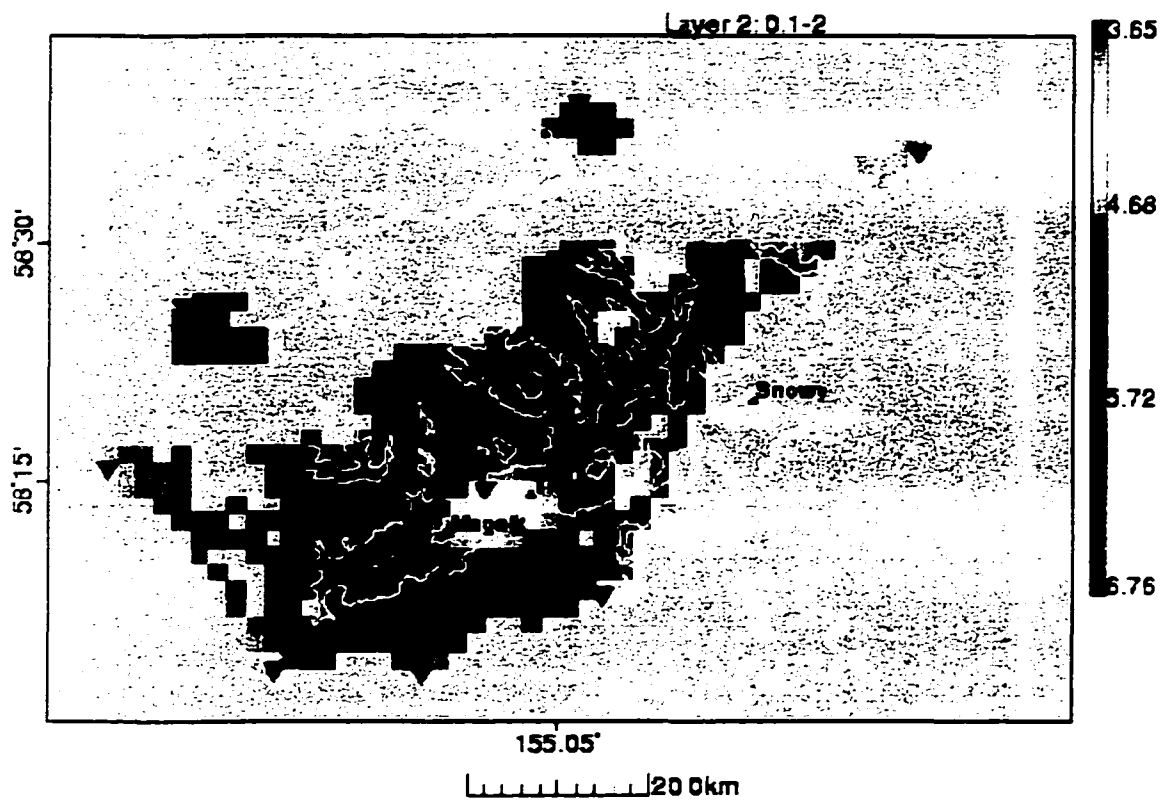
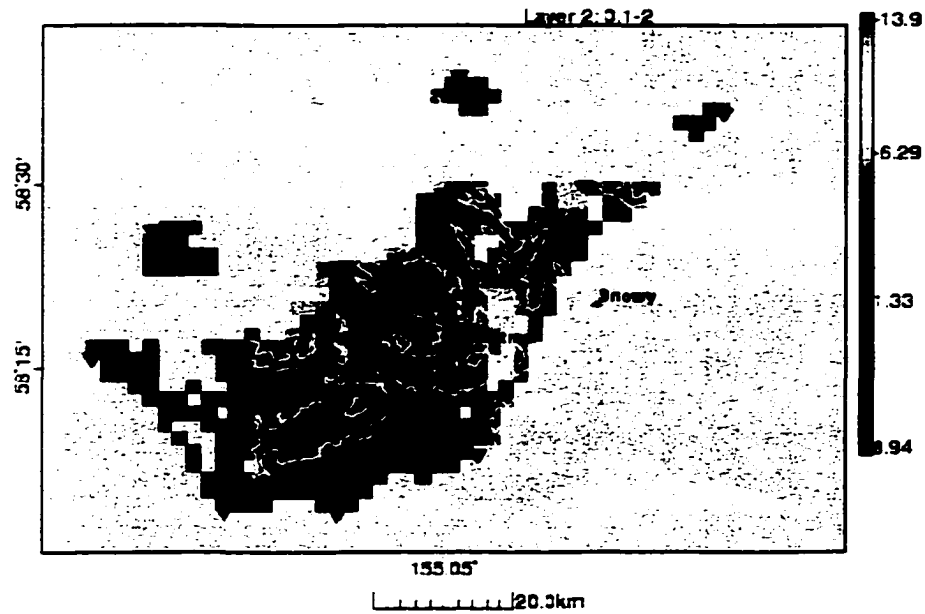


Figure 2.4: Final velocity for layer 2 (0-2 km). Color scale is in km/s.

a)



b)

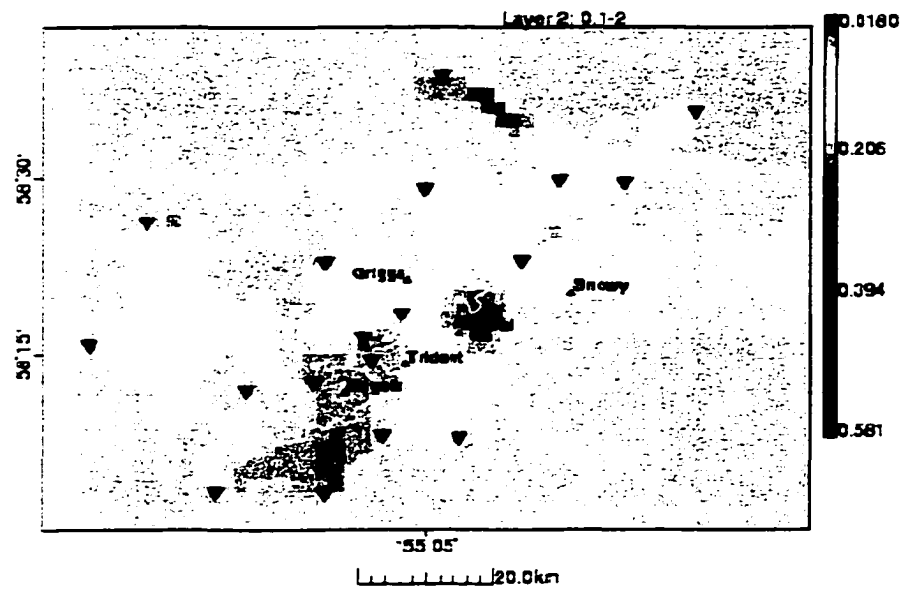


Figure 2.5: Checkerboard resolution (a) and jackknife error (b) maps for layer 2 (0-2 km). Color scale is % velocity (a) and km/s (b).

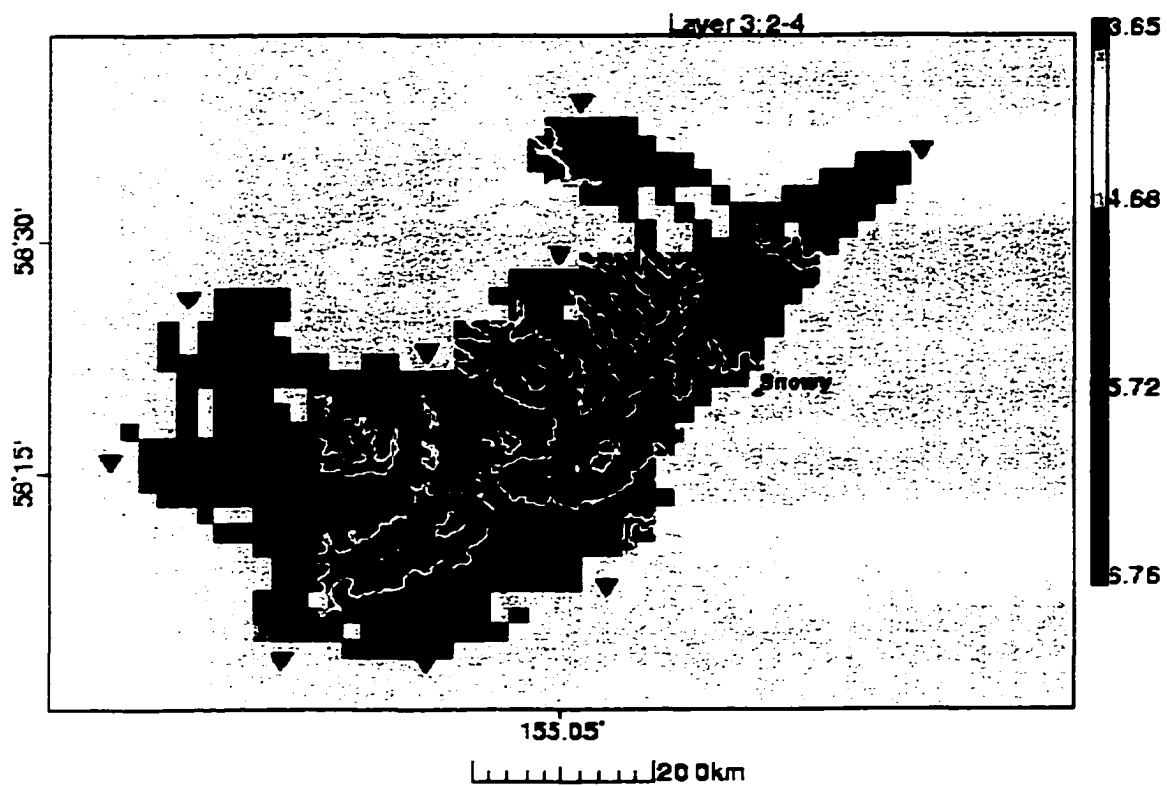
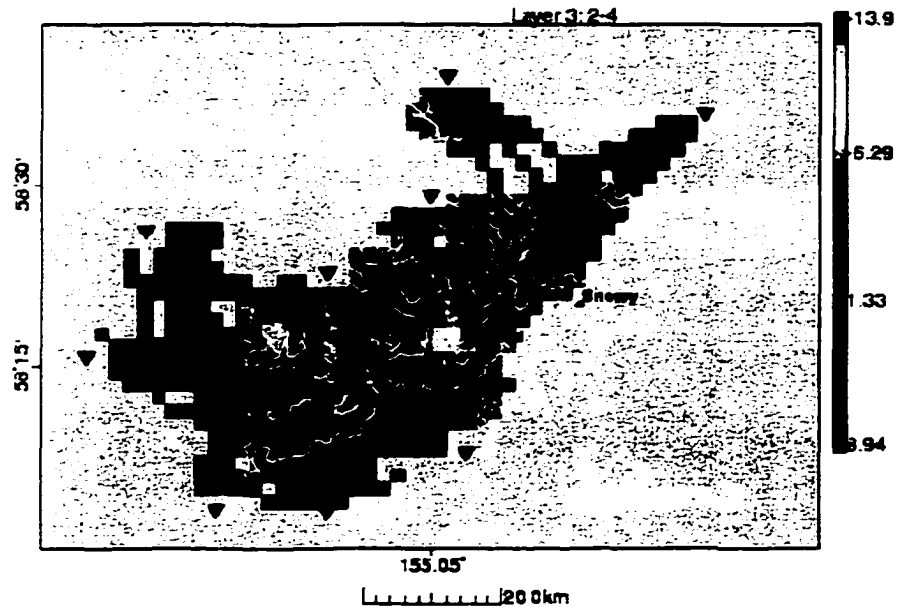


Figure 2.6: Final velocity for layer 3 (2-4 km). Color scale is in km/s.

a)



b)

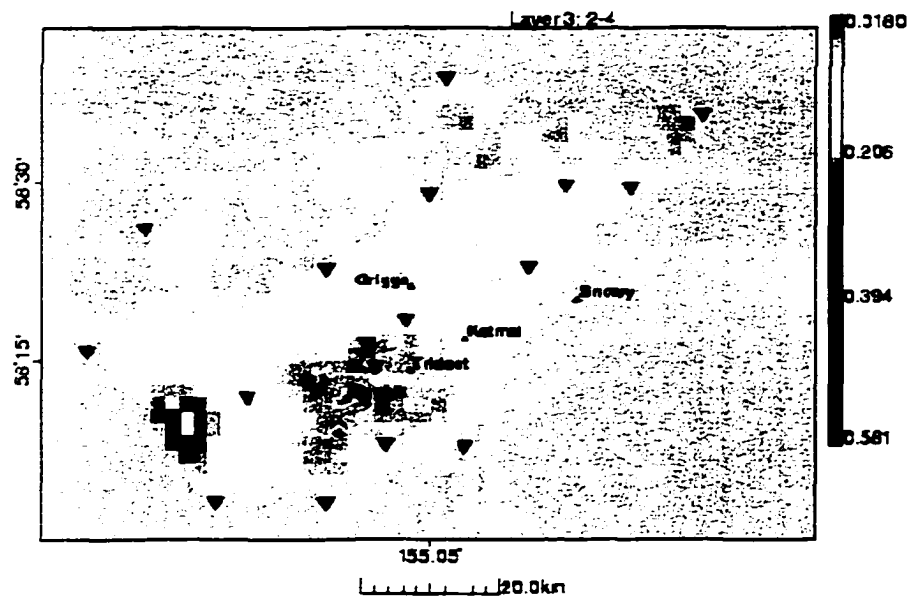


Figure 2.7: Checkerboard resolution (a) and jackknife error (b) maps for layer 3 (2-4 km). Color scale is in % velocity (a) and km/s (b).

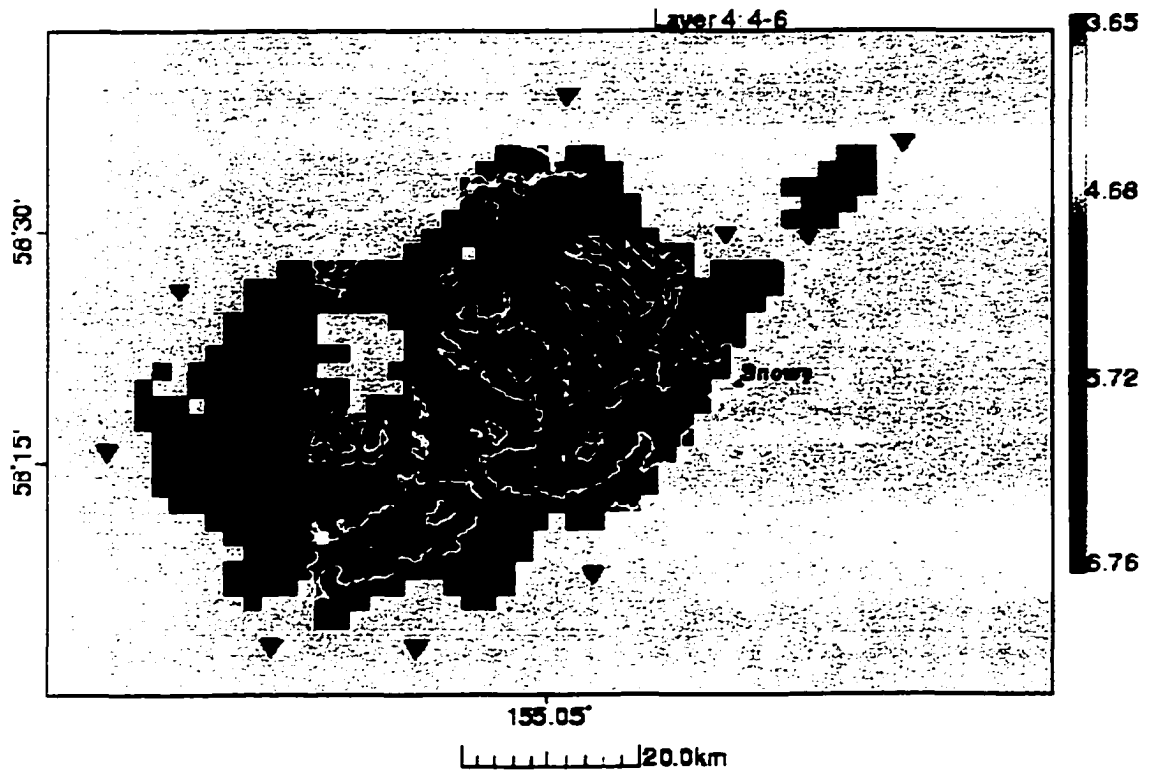
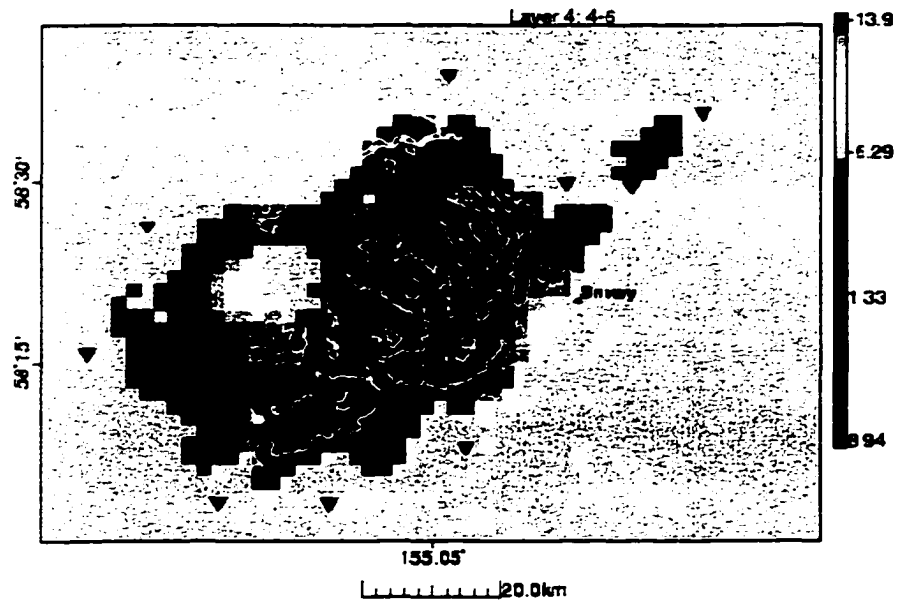


Figure 2.8: Final velocity for layer 4 (4-6 km). Color scale is in km/s.

a)



b)

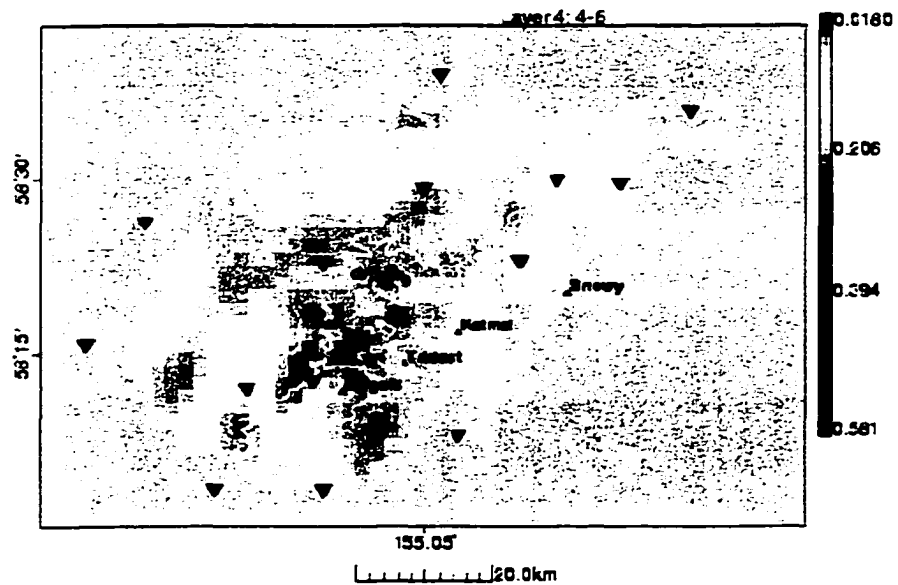


Figure 2.9: Checkerboard resolution (a) and jackknife error (b) maps for layer 4 (4-6 km). Color scale is % velocity (a) and km/s (b).

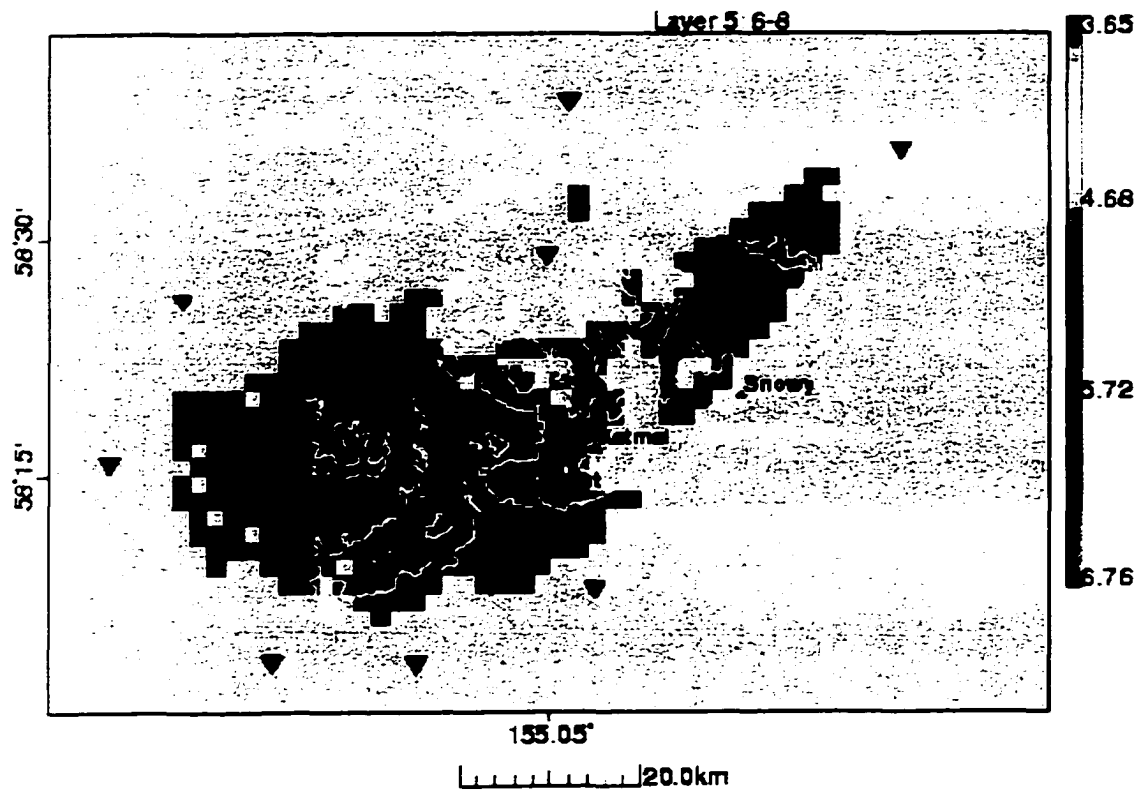
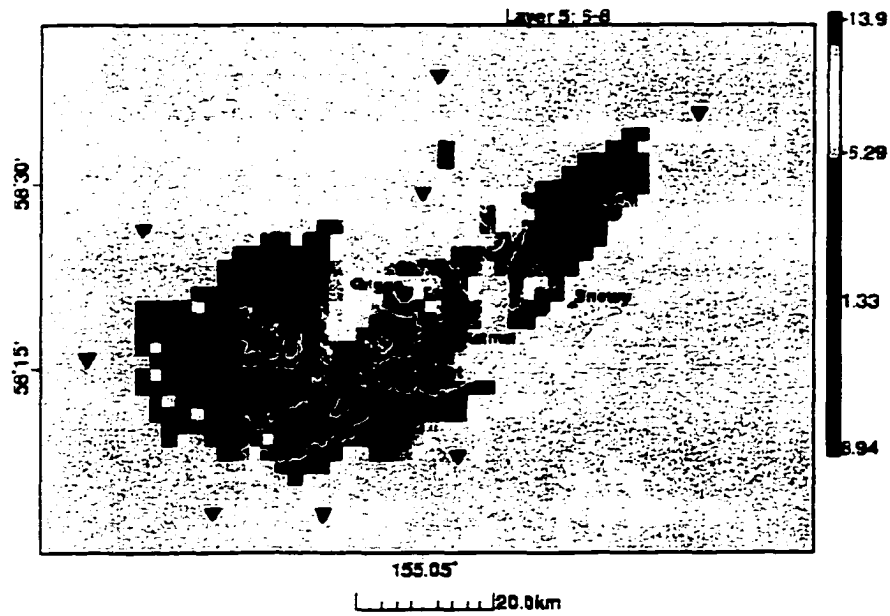


Figure 2.10: Final velocity for layer 5 (6-8 km). Color scale is in km/s.

a)



b)

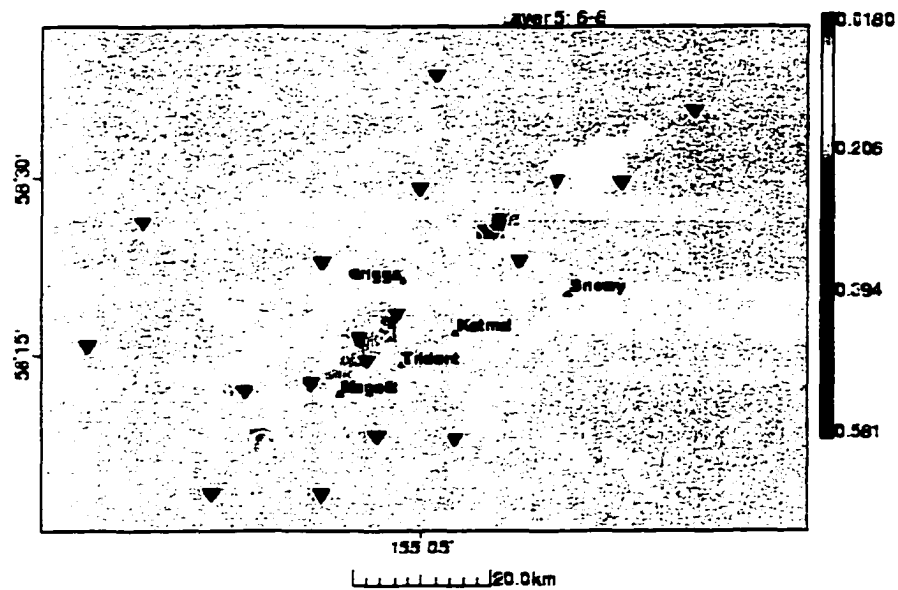


Figure 2.11: Checkerboard resolution (a) and jackknife error (b) maps for layer 5 (6-8 km). Color scale is in % velocity (a) and km/s (b). Note that jackknife is calculated using linear inversion step 0.

volcano. At 2-4 km depth, checkerboard and jackknife results (Figure 2.5) are well resolved from Martin to Katmai caldera and from Griggs volcano to about 5 km south of Martin and Mageik volcanoes. In the depth range 4-6 km, the model is less well resolved as the checkerboard inversion is poorly resolved (Figure 2.8, 2.9). The uppermost layer (Figure 2.2 and 2.3) includes mostly uni-directional rays and the results in this layer are probably associated with the static residual of the site. For example, the 0.25 sec travel-time delay at station KCE (Table 2.1) is expressed in the velocity structure as a very low velocity region in the vicinity of Katmai pass (Figure 2.3). Layer 5 (6-8 km depth) is considered poorly resolved in this inversion because the checkerboard reconstruction (Figure 2.11) is not possible and the linear jackknife has too few rays traversing the layer. For this reason, the Layer 5 velocity structure (Figure 2.10) is considered ill-resolved and un-interpretable.

Table 2.4: Cumulative Chi-squared misfit reduction with iteration number.

<u>Iteration #</u>	<u>Chi-squared reduction(%)</u>
0	36.23
1	19.58
2	10.79
3	10.33
4	7.67
5	6.98
6	9.45
7	8.70
8	10.79

Within the interpretable regions of the model, the P-wave tomography reveals a prominent low velocity zone (3.6-5.0 km/s) centered at Katmai pass, and extending along the volcanic axis between Mageik volcano and the edge of Katmai caldera (Figure 2.3, 2.5, 2.7, 2.9). In the depth range 0.0-4.0, the anomaly at Katmai pass has velocities of about 4.3 km/s while the volcanic axis has velocities of about 4.3 km/s to 5.5 km/s. These velocities are 20-25% lower than velocities observed outboard of the Katmai pass region (5.5-6.0 km/s). The Katmai pass anomaly appears to extend through all model layers but is subtle in layer 4 (4-6 km). Here, the velocities are about 5.0 km/s, a relatively low value compared to the velocities elsewhere at this depth (5.5-6.6 km/s). Mageik, Trident and Novarupta volcanoes have lower relative velocities than both Martin and Griggs volcanoes (5.0-6.0 km/s).

The regional velocities in the study area appear to be highly variable but generally increase with depth. Uppermost crust at 0-4 km depth has average velocities of about 5-6 km/s. This average is taken at stations on non-volcanic bedrock and might reflect the average velocity of the Jurassic Naknek Formation. At depths of 4-6 km below the surface the velocities are 6-7 km/s. These higher velocities might represent granitic rocks common in the basement of the Alaska Peninsula and South-central Alaska (Magoon et al., 1976). The highest velocities in the region are observed between Griggs and Snowy volcano with velocities between about 6.0-6.5 km/s in the depth range 0-6 km.

A further result of the velocity inversion is the final locations of the high quality earthquakes (Figure 2.12). The majority of the 815 events relocate in 3 clusters centered at Martin-Mageik volcanoes, Trident volcanoes and Katmai caldera. The earthquakes

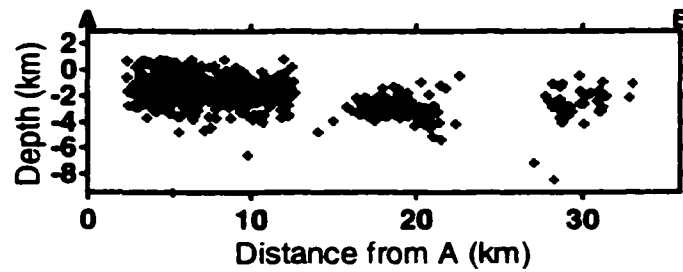
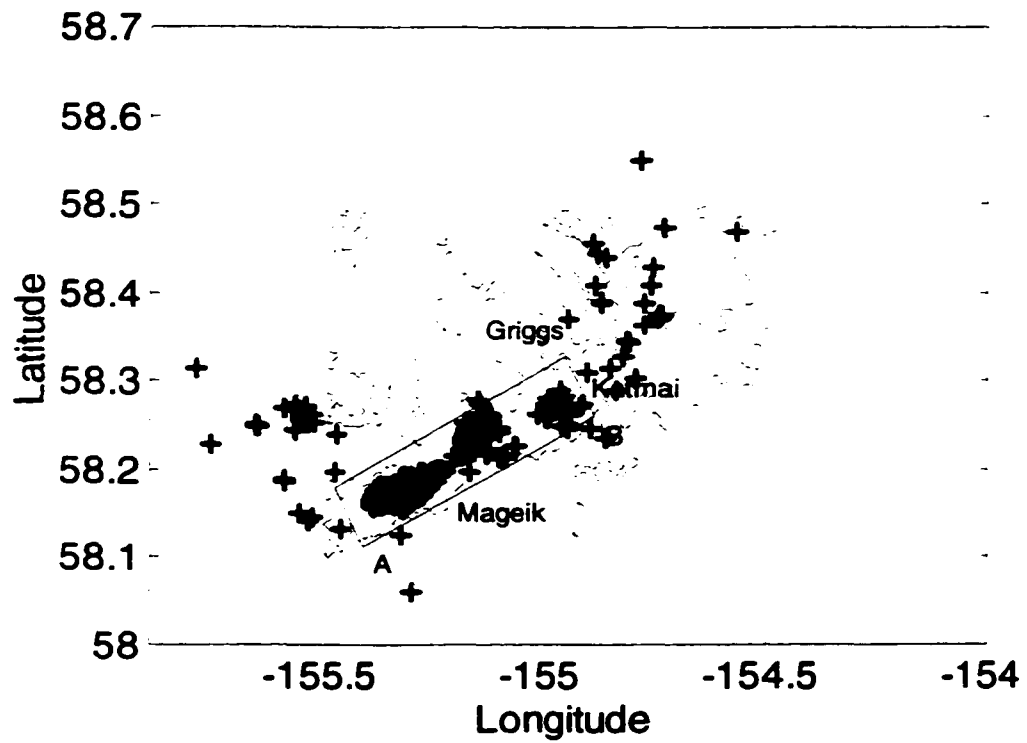


Figure 2.12: Map and cross-section of relocated hypocenters. The 5th inversion step used 815 high quality earthquakes and over 8000 rays.

(Figure 2.12), when compared to earthquakes located using the standard model (Figure 2.1) have generally tighter clustering at Martin and Mageik volcanoes and a shifting of epicenters of the Katmai caldera cluster from 2 to 3 km north of the volcano to directly beneath the volcano. An additional feature of the relocation is the elimination of a location artifact (Figure 2.1) for events located 1 km above sea level at Martin, Mageik and Trident volcano. The relocation pushed these events to depths of 0-5 km.

In summary, the new velocity model reduces the RMS travel-time residual by 27% compared to the standard velocity model. The new model yields anomalously low velocities at Katmai pass and along the volcanic axis, consistent with independently determined gravity results (Kienle, 1971). Finally, the model appears to yield better quality earthquake locations that tighten the clustering of the Martin-Mageik seismic cluster and eliminate an artifact causing earthquakes to locate erroneously at 1 km above sea level. These results taken together suggest that the inversion results are improved over the prior one-dimensional velocity model. These results in conjunction with new attenuation results (Chapter 3) and prior gravity data, provide strong evidence in favor of partially molten rock at shallow depth beneath the Mageik-Katmai-Novarupta region. Higher relative velocities at Martin and Griggs volcanoes suggest that no magma is resident in the shallow crust at these volcanoes. Detailed interpretations of the results are deferred to Chapter 6 where they are integrated with *b*-value and attenuation results of Chapters 3, 4 and 5.

2.6 References

Aki, K. and Lee, W.H.K., Determination of three-dimensional velocity anomalies under a seismic array using first P arrival times from local earthquakes 1. A homogeneous initial model, J. Geophys. Res., 81, 4381-4399, 1976.

Aki, K., Christofferson, A., Husebye, E.S., Determination of the three-dimensional seismic structure of the lithosphere, J. Geophys. Res., 82, 277-296, 1977.

Benz, H.M., Chouet, B.A., Dawson, P.B., Lahr, J.C., Page, R.A., and Hole, J.A., Three-dimensional P and S wave velocity structure of Redoubt Volcano, Alaska, J. Geophys. Res., 101, 8111-8128, 1996.

Fogleman, K.A., Stephens C.D., and Lahr J.C., Catalog of earthquakes for southern Alaska for 1985, U.S. Geol. Surv. Open File Report, 88-312, 112 pp., 1988.

Gilbert, P., Iterative methods for the three-dimensional reconstruction of an object from projections, J. Theor. Biol., 36, 105-117, 1972.

Hounsfield, G. N., Method and apparatus for measuring X or gamma radiation absorption or transmission at plural angles and analyzing the data, U.S. Patent 3-778-614, 1973.

Humphreys, E.D., and Clayton, R.W., Adaptation of back projection tomography to seismic travel time problems, *J. Geophys. Res.*, 93, 1073-1085, 1988.

Kienle, J., Gravity traverses in the Valley of Ten-Thousand Smokes, Katmai National Monument, Alaska, *J. Geophys. Res.*, 75, 6641-6649, 1970.

Lahr, J.C., HYPOELLIPSE/Version 2.0: A computer program for determining local earthquake hypocentral parameters, magnitude, and first motion pattern: U.S Geol. Surv., Open-File Report 89-116, 89p., 1989.

Lees, J.M., Seismic tomography in Western Washington, Ph.D. Thesis, 173 p., Univ. of Wash., Seattle, 1989.

Lorenzen, R.J.L., Seismic tomography of Redoubt volcano, M.S. Thesis, 78 p, Univ. Alaska-Fairbanks, 1994.

Lu, Z., Fatland, R., Wyss, M., Li, S., Eichelberger, J., Dean, K., Freymueller, J., Deformation of New Trident Volcano measured by ERS-1 SAR interferometry, Katmai National Park, Alaska, *Geophys. Res. Lett.*, 24, 695-698, 1997.

Magoon, L.B., Adkinson, W.L., Edgbert, R.M., Map showing geology, wildcat wells, Tertiary plant fossil localities, K-Ar age dates, and petroleum operations, Cook Inlet area, Alaska, U.S. Geol. Surv. Map., I-1019, 1976.

Matumoto, T., Seismic body waves observed in the vicinity of Mount Katmai, Alaska, and evidence for the existence of molten chambers, Geol. Soc. Amer. Bull., 82, 2905-2920, 1971.

Mavco, G.M., Velocity and attenuation in partially molten rocks, J. Geophys. Res., 85, 5173-5189, 1980.

Moran, S.C., Three-dimensional P-wave velocity structure in the Greater Mount Rainier area from local earthquake tomography, Ph.D. Thesis, 168 p., Univ. of Wash., Seattle., 1997.

Paige, C.C., Saunders, M.A., LSQR: An algorithm for sparse linear equations and sparse least squares, ACM Trans. Mathematical Software, 8, 43-71, 1982a.

Paige, C.C., Saunders, M.A., LSQR: Sparse linear equations and least squares problems, ACM Trans. Mathematical Software, 8, 195-209, 1982b.

Pavlis, G.L., and Booker, J.R., The mixed discrete-continuous inverse problem: Application to the simultaneous determination of earthquake hypocenters and velocity structure, *J. Geophys. Res.*, 85, 4801-4810, 1980.

Power, J.A., Villasenor, A., Benz, H.M., Seismic image of the Mount Spurr magmatic system, *Bull. Volcanol.*, 60, 27-37, 1998.

Press, W.H., Teukolsky, S.A., Vetterling, W.H. and Flannery B.P., Numerical recipes in Fortran 77: The art of scientific computing, Second Ed. Cambridge University Press, 933 p., 1996.

Spencer, C. and Gubbins, D., Travel-time inversion for simultaneous earthquake location and velocity structure determination in laterally varying media, *Geophys. J. R. Astr. Soc.*, 63, 95-116, 1980.

Um, J. and Thurber, C., A fast algorithm for two-point seismic ray tracing, *Bull. Seis. Soc. Amer.*, 77, 972-986, 1987.

Ward, P.A., Pitt, A.M. and Endo, E., Seismic evidence for magma in the vicinity of Mt. Katmai, Alaska, *Geophys. Res. Letts.*, 18, 1537-1540, 1991.

Chapter 3: P-wave Attenuation

3.0 Abstract

The three-dimensional P-wave attenuation structure of the Katmai group of volcanoes is determined between the surface and 8 km below sea level by inverting measured t^* values for the attenuation. The data included 1301 rays from 230 earthquakes recorded on a local 18 station short-period network. The t^* calculation was determined by regressing the log amplitude of the spectra in the 3.91-13.26 Hz range after deconvolving the instrument and site amplification. Linearity of the regression for t^* is assured by eliminating earthquakes with source corner frequencies below 15 Hz from the inversion. Earthquake locations and raypaths were determined using the velocity structure developed in a prior P-wave velocity study (see Chapter 2).

Results of the inversion suggest that high attenuation occurs along the volcanic axis $1/Q = 0.008-0.018$ ($Q \sim 55-125$) and centered at Katmai pass ($Q = 55$), and generally lower attenuation outboard $1/Q = 0.01-0.000$ ($100 < Q < \infty$). The attenuation results are coincident with a low velocity anomaly (~ 4.3 km/s; see Chapter 2) and low gravity anomaly (-35 mgal) also in the vicinity of Katmai pass. The results are consistent with an interpretation of partially molten rock in the vicinity of Katmai pass in the depth range 0-4 km below sea level.

3.1 Introduction

The attenuation of waves is, in the simplest terms, the decay of the wave amplitude as the wave propagates through a body. The observed decay results from either anelastic friction (also called intrinsic attenuation) or by scattering during propagation, but does not include the amplitude reduction due to geometrical spreading. Scattering off small-scale structures will reduce the amplitude of the primary wave and generally increase the amplitude of the coda, with no loss in energy from the total wavefield. The frictional amplitude decay associated with the intrinsic attenuation is given by the unitless quantity Q in terms of the fractional energy loss per cycle

$$\frac{1}{Q(\omega)} = \frac{-\Delta E}{2\pi E} \quad 3.1$$

Where E is the peak strain energy and $-\Delta E$ is the energy loss per cycle. Here $Q(\omega)$ is inversely related to the strength of attenuation. Most earth problems deal with a decay of signal amplitude with time and so the attenuation is reformulated in terms of the amplitude as,

$$A(t) = A_0 e^{\frac{-\omega t}{2Q}} \quad 3.2$$

where t is the elapsed time along the propagation direction, ω is the frequency and A_0 is the amplitude at a reference distance, usually near the source.

The generalized form of the attenuation problem discussed above has been applied as an earth science problem, and a variety of methods have been developed over the past 30 years (Tonn, 1989). The most common methods include the spectral ratios (Solomon and Toksoz, 1970; Frankel, 1982) and rise-time methods (Gladwin and Stacey, 1974). These methods are applied to individual stations, but the parallel development of new tomographic techniques (Chapter 2) has prompted research in three-dimensional attenuation structure using data from both passive (Wittlinger et al., 1983; Scherbaum, 1990; Lees and Lindley, 1994; Wu and Lees, 1996) and active sources (Evans and Zucca, 1988; Zucca and Evans, 1992). The advantage of many stations and sources can thus be used to form a three-dimensional image of the earth's attenuation structure.

Attenuation in the earth's crust is generally dependent on the frequency over a selected bandwidth (Patane et al, 1994; Aki, 1980). In these studies, the frequency dependence of Q , as given by the relation $Q=Q_0f^n$, ranged between $0.3 < n < 1.6$. Despite the apparent frequency dependence, attenuation tomography methods (Wittlinger et al., 1983; Scherbaum, 1990; Lees and Lindley, 1994) have generally assumed that attenuation is frequency independent (constant Q with frequency) over the bandwidth of interest.

A second assumption of passive source attenuation studies relates to the behavior of the source spectra. Inversion methods by Scherbaum, (1990), and Lees and Lindley, (1994) assume that the source spectra behaves according to the Brune (1970) model with a flat frequency response below the corner frequency and a $1/\omega^2$ rolloff above.

Departures from this model are then ascribed to the whole-path attenuation. However, Patane et al., (1994) have shown that attenuation-corrected spectra at Etna volcano roll off above the corner frequency according the relation $1/\omega^3$ in accordance with more complicated source models (Dahlen, 1974; Boatwright, 1980). This apparent ambiguity casts some doubt on three-dimensional tomographic techniques that model the attenuation above the corner frequency and leads to the fundamental question: are these methods inverting for variations in the attenuation, or a complex combination of both the source and the attenuation? Rather than to answer this difficult question, it is assumed that one common feature of the source models can be relied upon, namely that the source amplitude is flat below the corner frequency. Then, the only issue is to select earthquakes with corner frequencies above the bandwidth of interest and to determine the attenuation below this passband. This is the method of Wittlinger et al., (1983) and also of this study.

3.2 Theory

The observed spectra $S_p(f)$ can be represented in the form

$$S_p(f) = S_o(f)P_a(f)S_i(f)I(f), \quad 3.3$$

where $S_o(f)$ is the source, $P_a(f)$ is the path, $S_i(f)$ is the site amplification, and $I(f)$ is the instrument response. The generalized goal then is to reduce the effects of the site and

instrument, such that the whole path attenuation will be the dominant parameter of the inversion.

3.2.1 Attenuation measurement (t^*)

The amplitude spectrum of an earthquake is often exploited under the assumption of constant Q with frequency. Under this assumption, higher frequency waves decay more quickly than low frequency waves over the same path lengths and the Q can be estimated directly from the spectra. Substituting equation 3.2 into equation 3.3, the spectral amplitude is

$$S_p(f) = S_o(f) I(f) S_i(f) e^{\frac{-\omega t}{2Q}}. \quad 3.4$$

The exponent can be eliminated by taking the log of both sides, and with $\omega = 2\pi f$, the relation is expressed

$$\text{Log} (S_p(f) / S_o(f) S_i(f) I(f)) = -\pi f t / Q, \quad 3.5$$

then the relation is linear of the form

$$\text{Log} (S_p(f)) = \text{Log} (S_o(f) S_i(f) I(f)) - (\pi t / Q) f \quad 3.6$$

where $(\pi t/Q) = t^*$. Thus the slope of the log amplitude relation for the spectra gives the parameter t^* under the assumption that Q is independent of frequency. In this general relation the slope (t^*) is steeper for high attenuation and shallower for low attenuation. For the special case of no attenuation the slope would be flat and t^* would be 0. Also note from the left side of equation 3.5 that deconvolution of the instrument and site $S_i(f)$ and $I(f)$ can be completed to reduce their effect on the raw spectra. Furthermore, deconvolution of the source $S_o(f)$ is trivial as it is a constant with frequency as long as the corner frequency is higher than the frequency of interest.

3.2.2 Inversion

The attenuation inversion is analogous to the P-wave velocity inversion where the attenuation is ascribed to the path by the relation

$$t^* = \oint (1/QV) dr \quad 3.7$$

Where $1/Q$ is the unitless attenuation, $1/V$ is the slowness, and dr is an incremental path length. Consider next an abundance of rays traversing a region having an inhomogeneous attenuation structure. Then, rays traversing locales having higher attenuation will be imparted with higher t^* 's, and rays traversing locales with lower attenuation will be imparted with low t^* 's. For this general problem the region can be subdivided into

numerous blocks and l/Q values can be assigned to each of the blocks as long as the slowness and incremental path length are known. This is completed by inversion of the matrix system

$$B = C \cdot X, \quad 3.8$$

where C is a matrix of P-wave travel-time values (determined from path lengths and velocities), X is a row matrix of the unknown l/Q 's and B are the known t^* values.

Unlike the velocity inversion problem in Chapter 2, this equation is linear because the path lengths and velocities are known. Hence, only one inversion is required.

3.3 Methods

Earthquakes in the Katmai region having magnitudes from 0.8 to 1.8 M_L were selected for analysis. Each waveform was examined visually, and spectra were calculated for on-scale phases recorded at 100 samples per second on the 12-bit analog system (Figure 3.1). Spectra were calculated using a 128 sample Fast Fourier Transform (FFT) for both the P-phase and the pre-event noise (Figure 3.2). The P-phase spectral window begins 15 samples before the P-onset as determined by standard AVO processing while the noise window is determined 300 samples before the P-onset. The FFT window has a 10% Hamming taper (raised cosine) and S-phase contamination was mitigated by excluding spectra with S-P times less than 1.2 seconds. A total of 327 events were examined and 2977 spectra were calculated. The calculated spectra have a frequency resolution of 0.783 Hz, but neighboring amplitude values are averaged producing

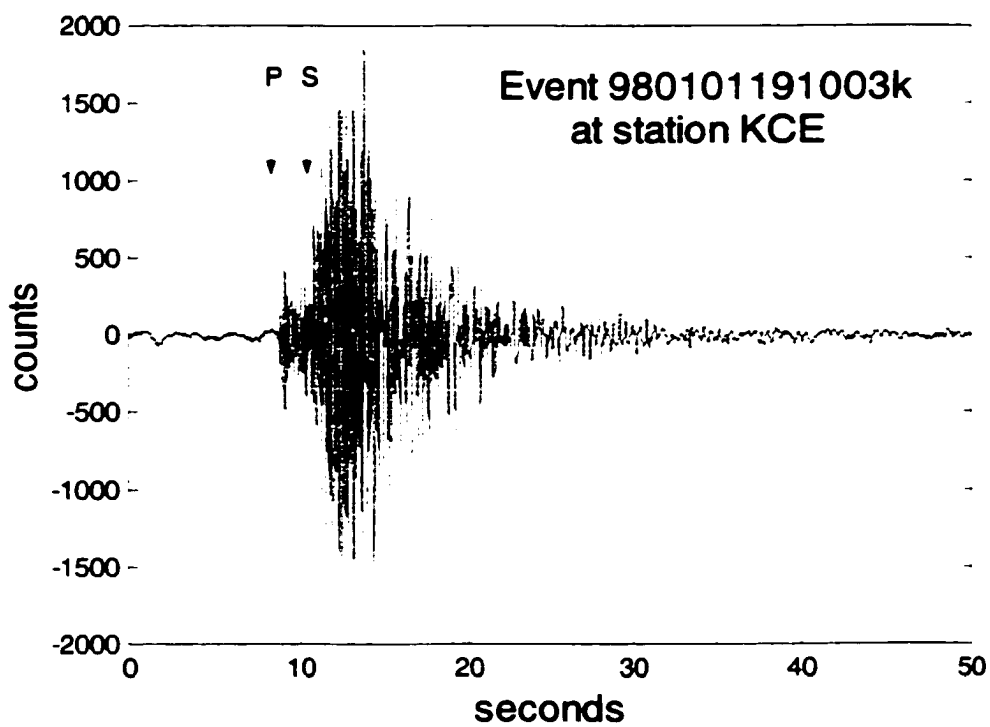


Figure 3.1: Example velocity function for event 980101191003p at station KCE.

Spectra were calculated at the analyst selected P arrival time shown.

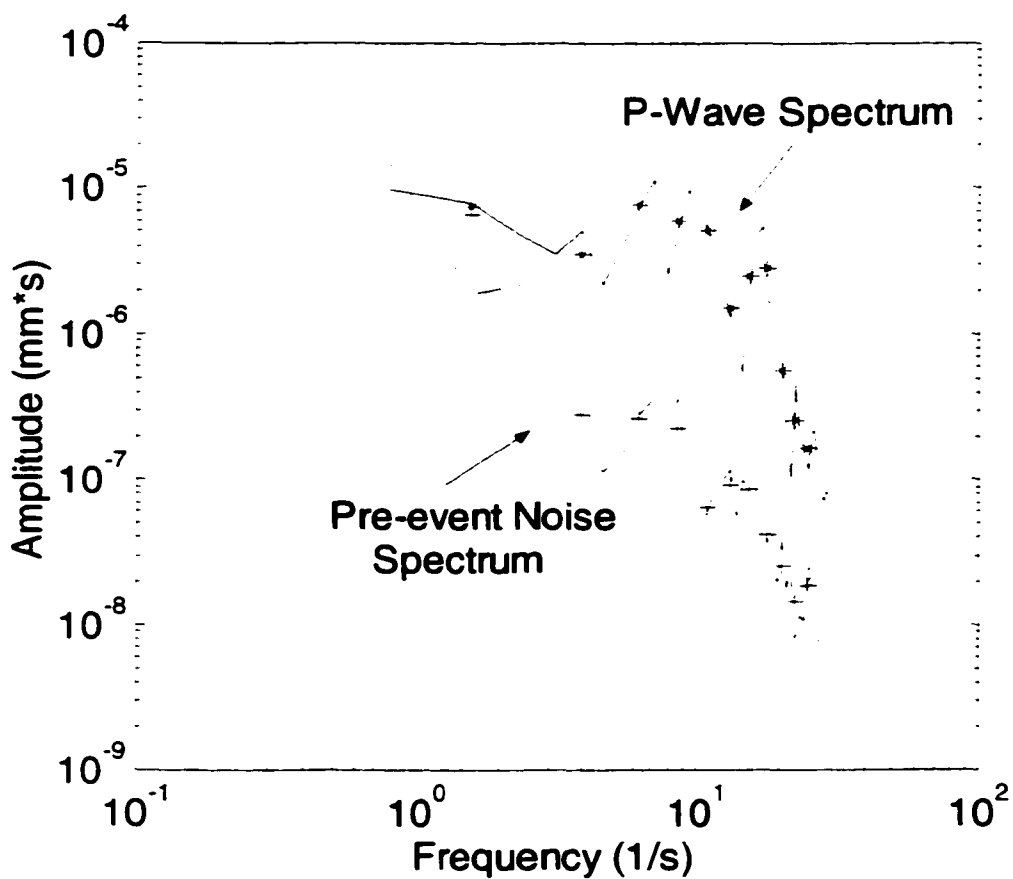


Figure 3.2: Amplitude spectra for typical earthquake. The spectra were calculated via a 128 sample Fast Fourier Transform for P-phase and pre-event noise. Stars and pluses are the averaged amplitude for the spectra at 1.56, 3.91, 6.25, 8.59, 10.94, 13.28, 15.63, 17.97, 20.31, 22.66 and 25.00 Hz. These averaged amplitude data were saved for further analysis.

smoothed spectral amplitudes at 1.56, 3.91, 6.25, 8.59, 10.94, 13.28, 15.63, 17.97, 20.31, 22.66 and 25.00 Hz (Figure 3.2). This scheme eased programming, databasing and processing of the spectra before the final inversion.

3.3.1 Instrument and site

The nominal instrument frequency response $I(f)$, is well known and deconvolved directly from the observed amplitude spectra. The site response $S_i(f)$, also called the site amplification factor, is determined in a multi-step process and then used to deconvolve the site response. As a first step, low quality spectra are removed by requiring signal to noise ratios greater than two and at least 5 good spectra per earthquake. For the 327 events analyzed, 129 earthquakes survived this requirement. For each survivor, a log-averaged spectrum was calculated (Figure 3.3) and the spectrum from each station is divided by the log-averaged spectrum, producing station amplifications relative to the average earthquake spectrum. Then, for each station, the totality of site amplification data is log-averaged. This log-average is the site amplification factor for a given station. The results for all stations in the study area are summarized in Figure 3.4 and Table 3.1. The principle result is the identification of strong amplification in the 17-20 Hz range at stations ACH, KAWH, KBM and KVT (Figure 3.4). It is surmised that high frequency amplification at these sites might result from resonance of the 1912 ignimbrite sheet or other near surface layer. If the P wave velocity is ~ 5 km/s and the resonance is 15-18 Hz, then the scale length of the resonator is ~ 0.20 - 0.29 km. This length is roughly equal to

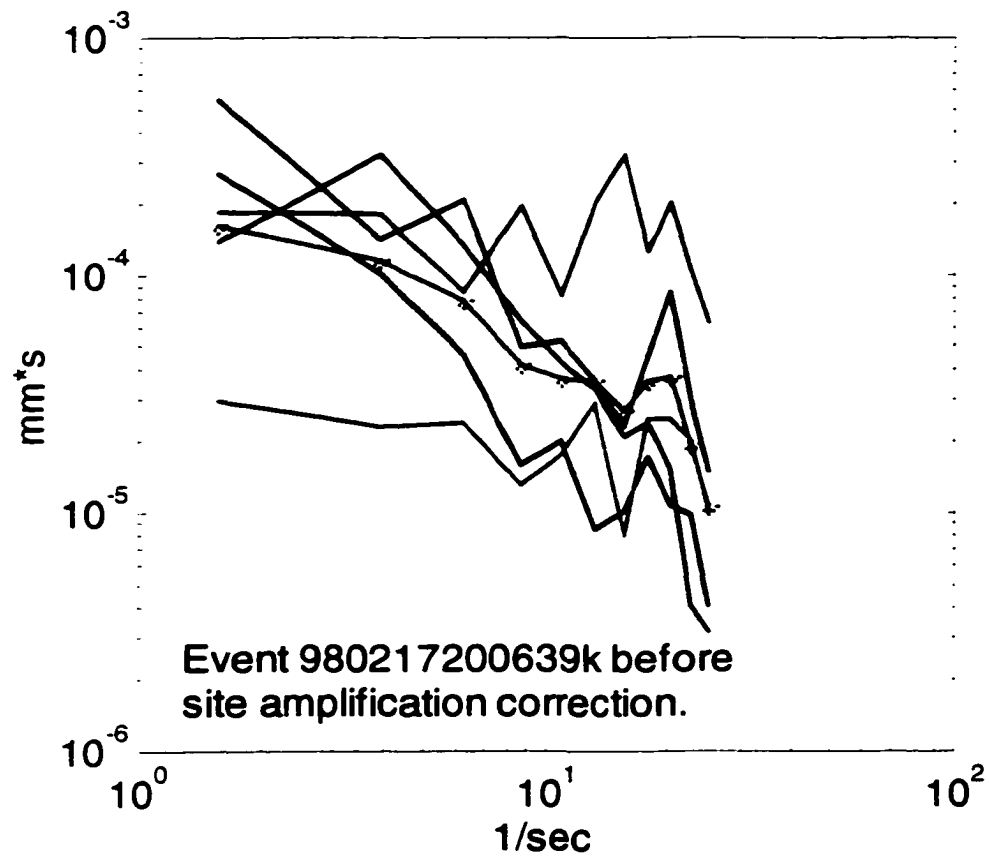


Figure 3.3: Spectra for event 980217200639.p. Stations used are KCE (green), KBM (cyan), KCG (blue), KJL (black), KVT (magenta). Connected red lines are the log average of the individual spectra. Geometric and instrument corrections are applied.

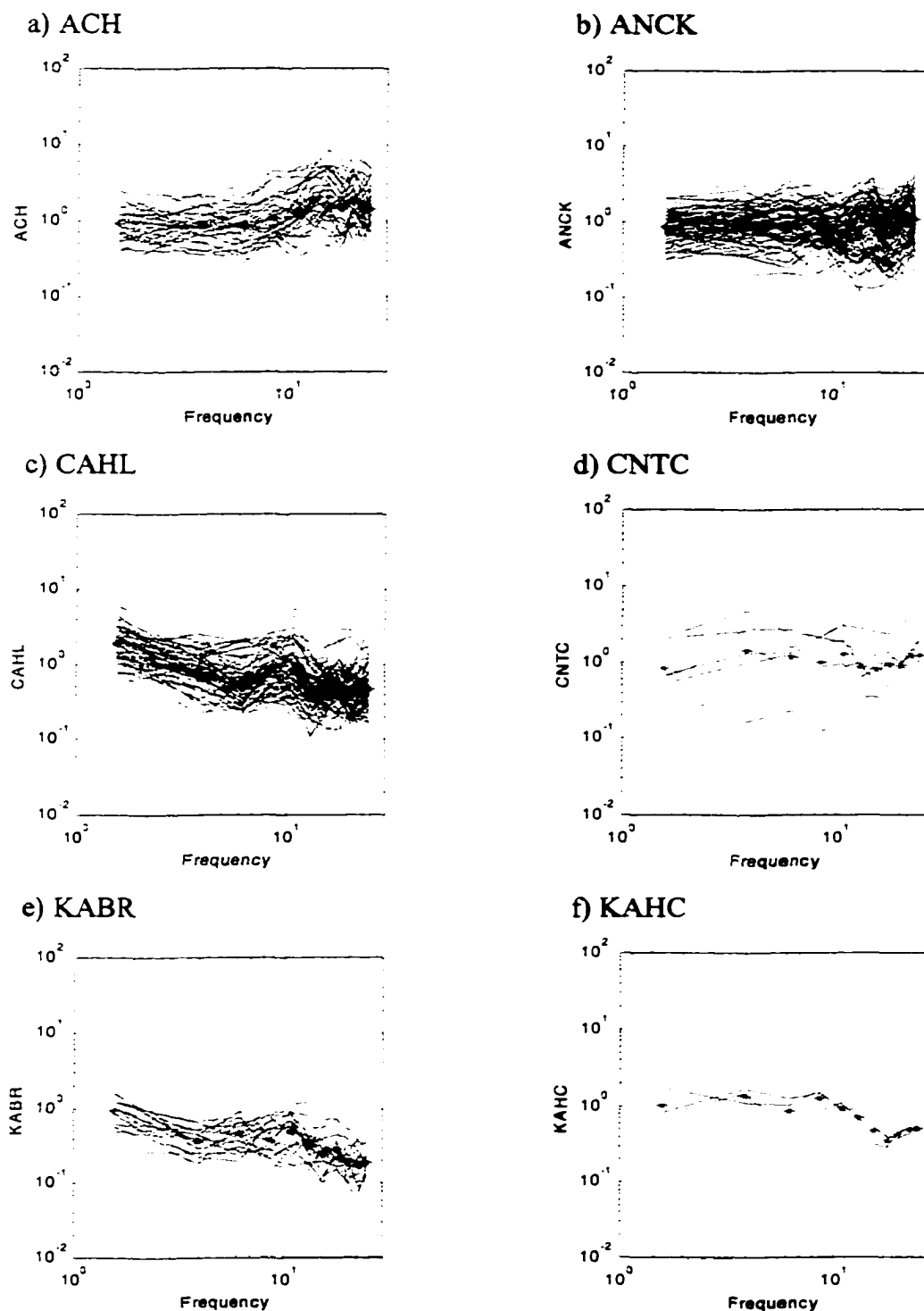


Figure 3.4: Site amplification factor for 18 stations of the Katmai network. See text for details.

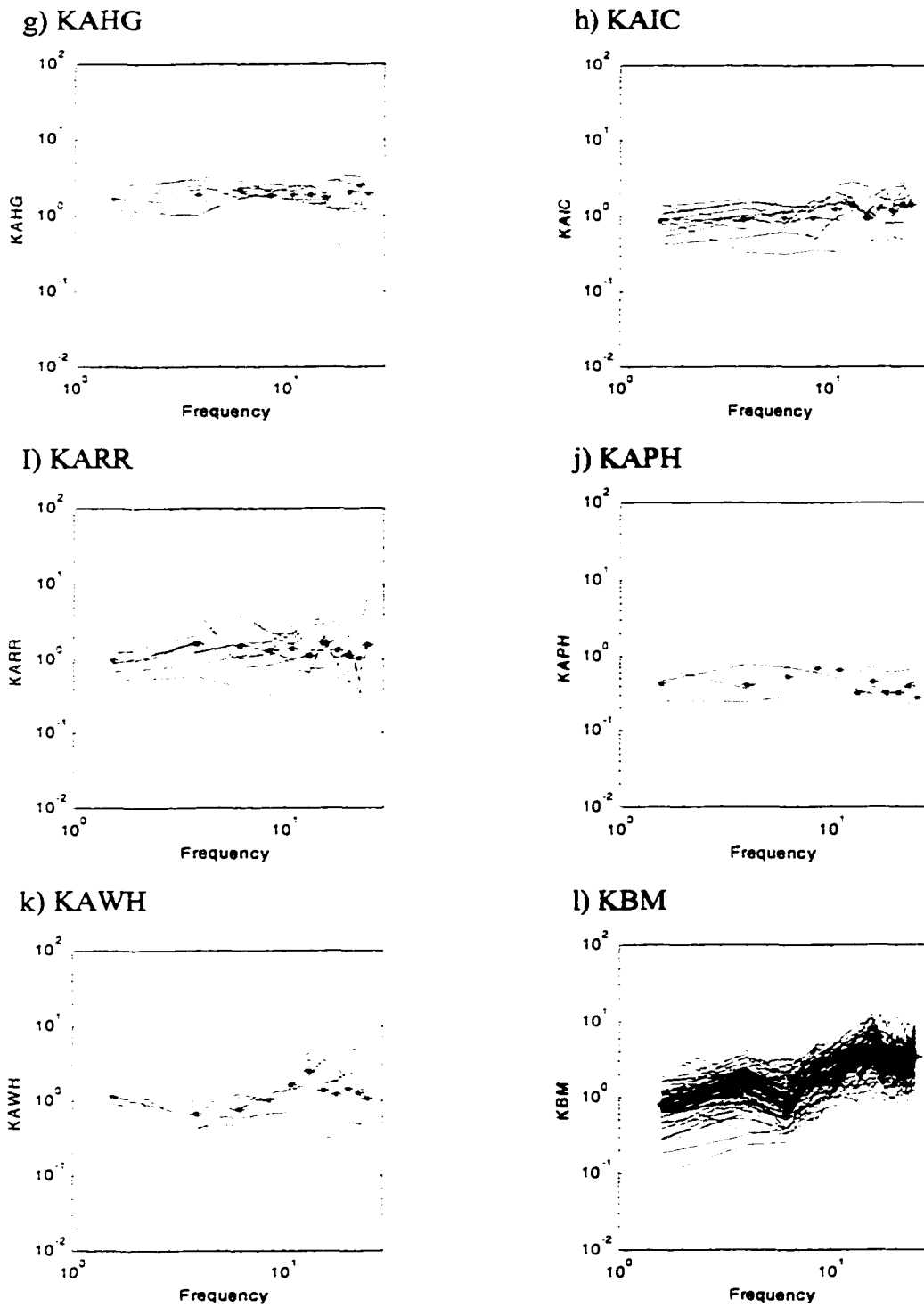


Figure 3.4: Continued

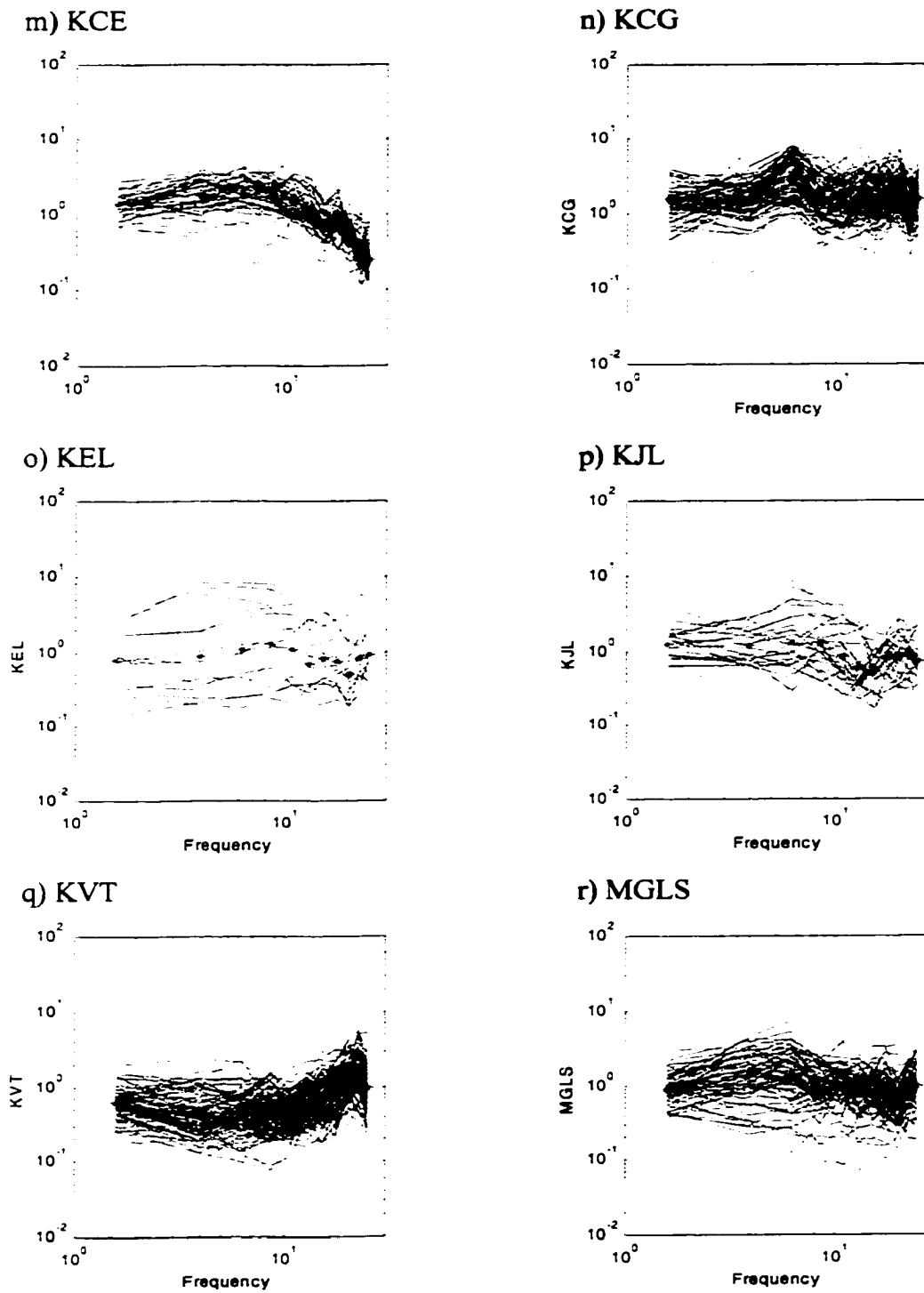


Figure 3.4: Continued

the thickness of the ignimbrite sheet (Kienle, 1991) as determined from gravity and seismic refraction data. It is also noted that the log-averaged spectrum shown in Figure 3.3 still contains this resonant feature. This suggests that the effect of the resonance has not been completely removed. Adding more stations to the log-averaged spectra might provide a more accurate correction for the site amplification factor. Unfortunately, the limited amount of high quality data (Table 3.1) prohibits such an analysis at this time. As the final step, the average site amplifications (Table 3.1) are applied as corrections to each spectrum, thus deconvolving the site amplification factor from the observed spectra $S_p(f)$ (Figure 3.5). Direct comparison of the spectra before (Figure 3.3) and after (Figure 3.5) the site amplification correction reveals the visual result of the applied correction: generally smoother spectra for which systematic effects of the site have been minimized. The corrected spectra (Figure 3.5) thus contain the attenuation $P_a(f)$, and the source $S_o(f)$, while the site $S_i(f)$ and instrument $I(f)$ effects are minimized.

3.3.2 The source

The source spectrum is thought to vary widely with magnitude, stress drop, rupture velocity and other features. Such variability impedes any effort to deconvolve the source effect. Regardless, it is useful to examine the spectra at the source in an effort to reduce the potential biases from the inversion process. In this study, the log averaged spectra

Table 3.1: Site amplification correction for each station. The amplification is determined for each station at a given frequency (f). The total number of readings per station (n) is reported in the final column. Data are determined from 128 sample FFT data.

$f(\text{Hz})$	1.56	3.91	6.25	8.59	10.94	13.28	15.63	17.97	20.31	22.66	25.00	n
ACH	0.94	0.89	0.86	1.11	1.31	1.89	2.06	1.52	1.85	1.61	1.44	43
ANCK	0.84	0.95	0.88	0.95	0.72	0.81	0.94	0.66	0.82	1.02	1.09	82
CAHL	1.90	0.84	0.55	0.82	0.81	0.45	0.43	0.48	0.41	0.45	0.47	72
CNTC	0.82	1.42	1.14	0.97	1.23	0.86	0.80	0.91	0.90	1.22	1.20	7
KABR	0.94	0.37	0.46	0.38	0.49	0.31	0.24	0.28	0.19	0.17	0.18	25
KAHC	1.02	1.37	0.87	1.26	0.95	0.70	0.46	0.34	0.42	0.48	0.51	3
KAHG	1.68	1.88	2.12	1.91	1.90	1.87	1.73	1.18	2.02	2.50	2.01	7
KAIC	0.87	0.92	0.94	0.92	1.24	1.40	0.92	1.31	1.16	1.43	1.44	12
KAPH	0.42	0.40	0.51	0.68	0.64	0.32	0.44	0.32	0.31	0.39	0.27	3
KARR	0.96	1.61	1.49	1.29	1.39	1.10	1.66	1.29	1.12	1.02	1.53	10
KAWH	1.15	0.66	0.77	1.02	1.57	2.39	1.38	1.21	1.40	1.23	1.05	6
KBM	0.78	1.44	1.01	1.76	2.33	3.18	4.11	3.05	2.75	2.70	3.32	97
KCE	1.35	1.76	1.88	1.74	1.43	1.16	0.72	0.82	0.52	0.33	0.25	55
KCG	1.51	1.52	2.93	1.48	1.38	1.59	1.49	1.71	1.90	1.13	1.52	88
KEL	0.80	0.89	1.08	1.28	1.10	0.70	0.81	0.75	0.49	0.84	0.93	15
KJL	1.25	1.20	1.28	1.30	0.85	0.60	0.54	0.78	0.87	0.82	0.74	31
KVT	0.61	0.44	0.44	0.44	0.45	0.60	0.66	0.90	1.27	1.50	0.97	112
MGLS	0.91	1.30	1.31	0.89	0.93	0.78	0.77	0.75	0.60	0.81	0.96	83

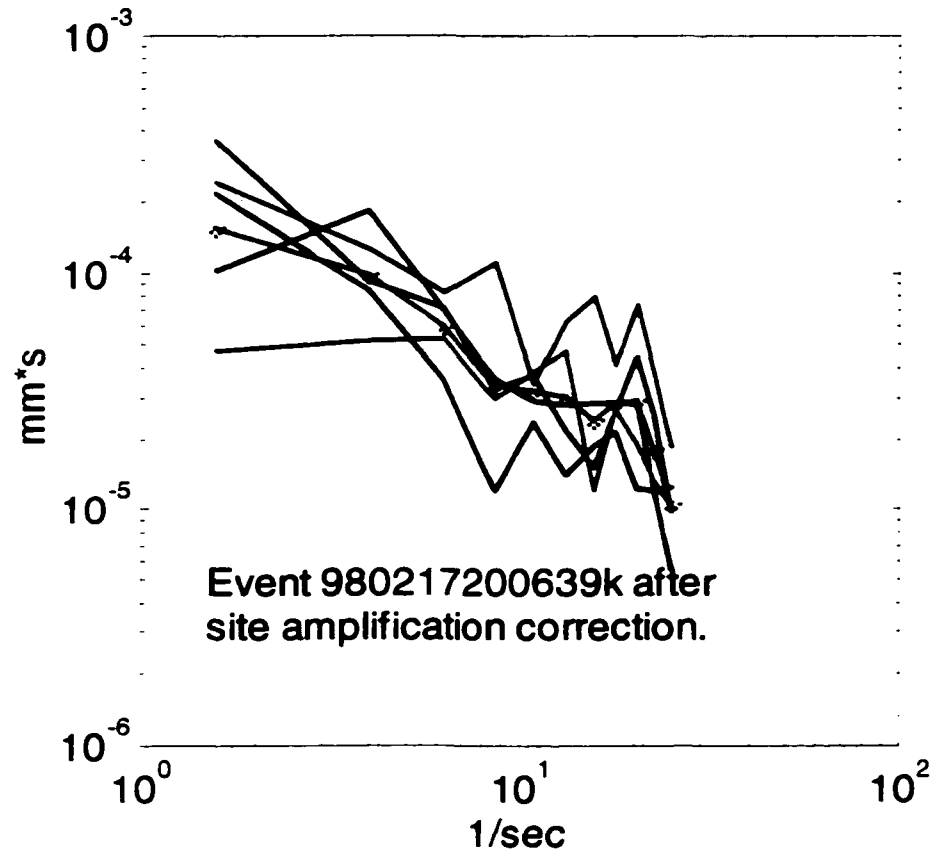


Figure 3.5: Spectra for event 980217200639.p with site amplification, instrument, and geometric spreading corrections applied. Stations used are KCE (green), KBM (cyan), KCG (blue), KJL (black), KVT (magenta). Connected red lines are the log average of the individual spectra. Note the improvement over spectra without site amplification correction (Figure 3.3).

used in the site amplification study were grouped based on their locations to observe any systematic aspect of the amplitude spectra. The data were grouped in a 2 km by 2 km lateral grid spacing and were further subdivided into shallow (< 4.0 km depth) and deep (> 4.0 km depth) locations. Gridded locations with three or more log averaged spectra are shown in Figure 3.6 and 3.7. Further, these log averaged spectra were also log averaged producing a 'typical' spectrum for that locale. The dominant feature is the observation of a peak in the 15-18 Hz range for many of the spectra. This observation suggests that the site amplification study of Section 3.3.1 has not completely removed the site resonance. Further, an inversion using data from this frequency range might be biased, producing a potentially unstable inversion. To avoid this potential bias, the feature is bypassed by inverting the data in the frequency range 3.91-13.28 Hz.

To further assess the spectra at the source, the slope of the frequency roll off between 3.91-13.28 Hz and its associated 95% confidence interval is calculated for each locale and plotted in map view for shallow (Figure 3.8) and deep earthquakes (Figure 3.9). The slopes of Martin, Mageik, and Trident clusters appear to have higher rolloffs than locations outboard of the volcanoes (Figure 3.8 and 3.9). Note that the 95% confidence intervals and hitcounts for each of the blocks are shown to offer an estimate of the confidence of the observations.

Results of the analysis suggest a strong systematic variation of the slope in space. The largest anomalies occur at shallow depth (less than 4 km) and centered near the low velocity zone of our P-wave inversion. Outboard of the volcanoes, and at greater depth, the slopes are flatter. Grid box 4, located near Angle Creek, is an exception. The spectra

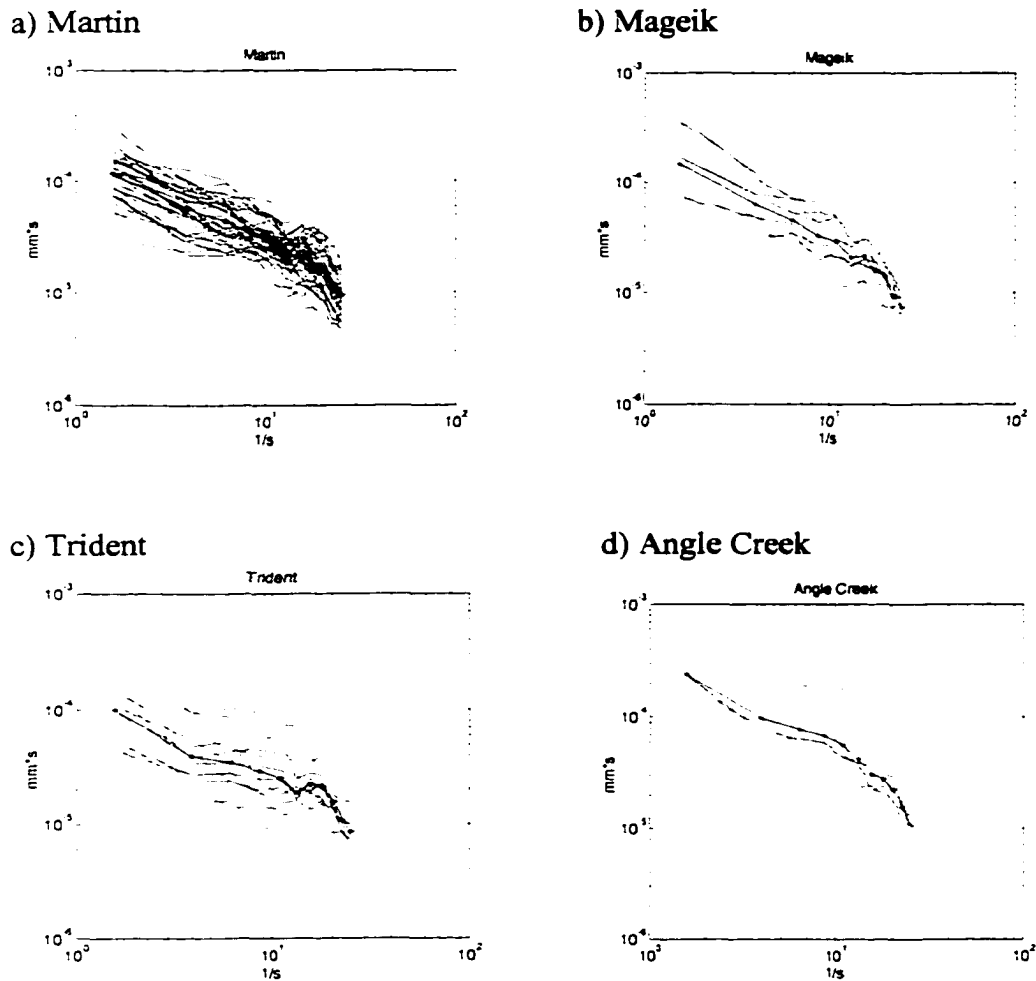


Figure 3.6: Log averaged spectra from earthquakes at given source regions. The regions are for shallow earthquakes (-3 to 4 km) shown in Figure 3.8 at, a) Martin, b) Mageik, c) Trident and d) Angle Creek. Red lines are the log averaged spectra for earthquakes with at least 5 high quality spectra. The blue star connected lines are the log average of all earthquakes within the grid block.

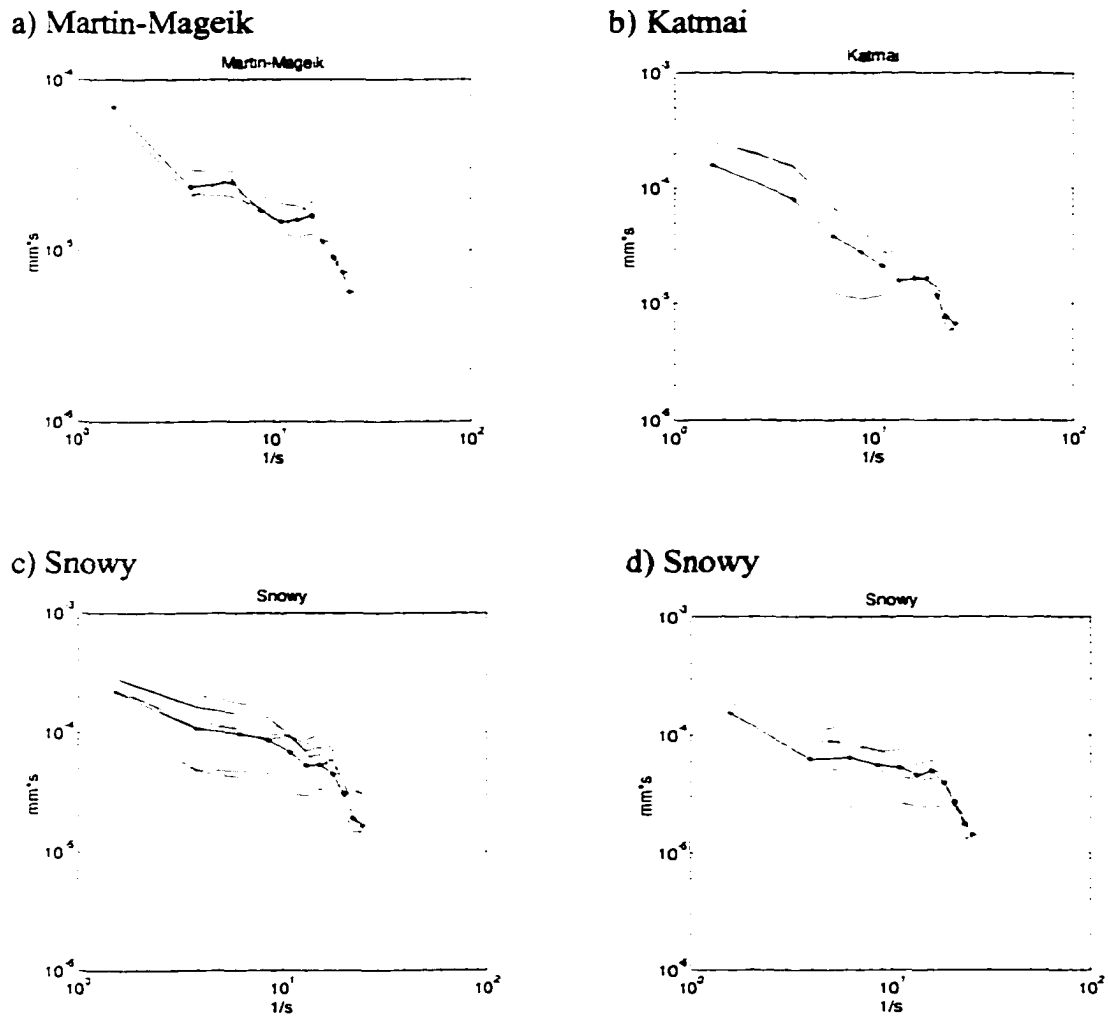


Figure 3.7: Log averaged spectra from earthquakes at given source regions. The explanation is the same as Figure 3.6 for deeper events (4 km-12 km) located at a) Martin-Mageik, b) Katmai, and c-d) Snowy in Figure 3.9.

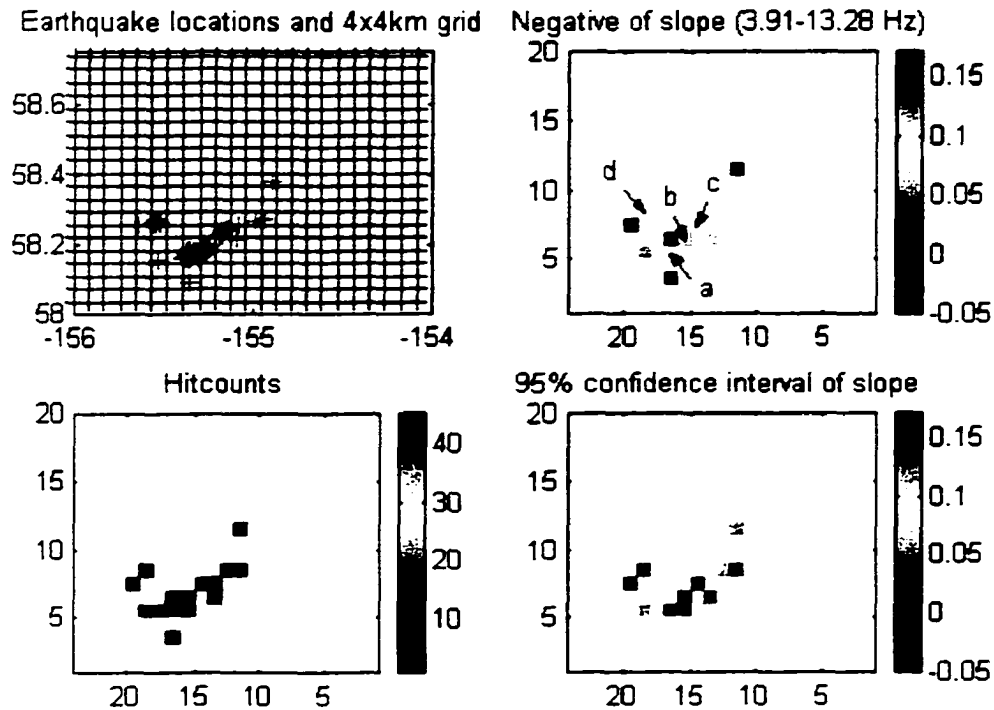


Figure 3.8: Grid map of earthquake spectra for depth range of 3 km above sea level to 4 km below sea level. The upper left panel shows the defined grid (blue line) and earthquakes in the study area (magenta +). The upper right panel shows the negative of the regressed slope for the frequency range 3.91-15.63 Hz. Two quality measures of the regression for each grid block are shown: Hitcounts in the lower left panel, and 95% confidence interval of the regressed slope in the lower right panel. Grid nodes are 4 km by 4 km. Letters a-d in the slope panel refer to Figure 3.6a-d.

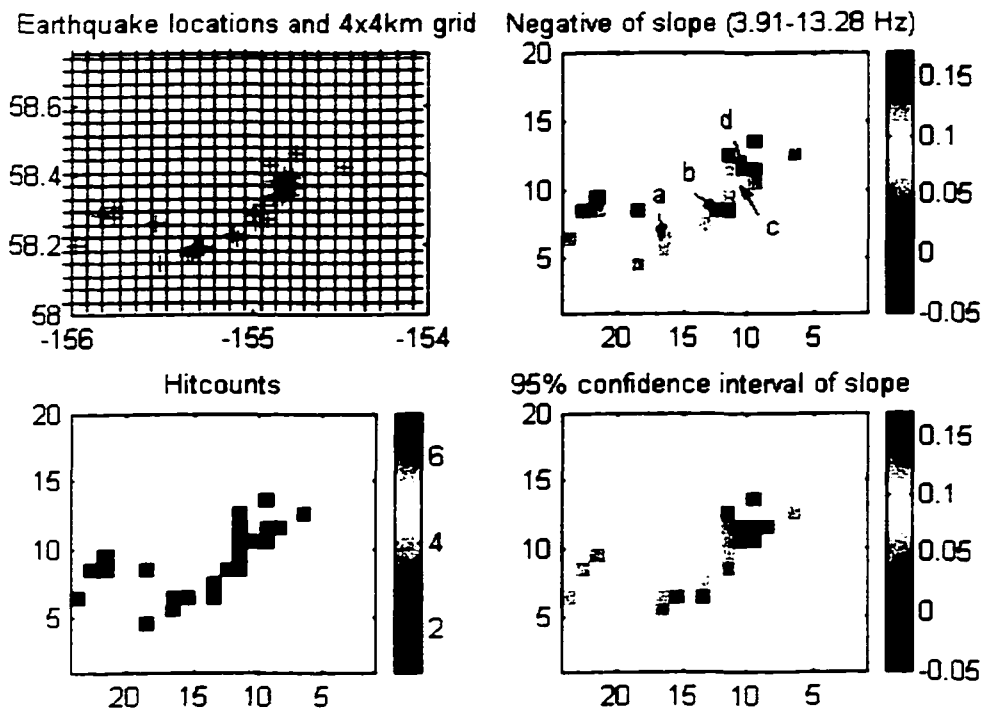


Figure 3.9: Grid map of earthquake spectra for depth range of 4 km below sea level to 12 km below sea level. Letters a-d in slope panel refer to Figure 3.7 a-d. See Figure 3.8 for explanation.

from this locale appear to have an anomalously steep slope. On closer examination of the spectra from this grid box (Figure 3.1.4), it is apparent that the frequency rolls off rapidly at less than 13 Hz. Such spectra might have low source corner frequencies that could contaminate the inversion results.

To assess the importance of source corner frequencies on the inversion, parameters such as the moment, stress drop, and rupture velocity are evaluated. For simplicity, the Haskell dislocation model is assumed. This model predicts that the $1/\omega$ corner frequency, F_c is inversely proportional to the rupture duration τ_d

$$F_c = 2/\tau_d. \quad 3.10$$

Because the rupture propagates, its duration must be dependent on the receiver location in relation to the rupture direction. If the rupture propagates towards the receiver, then

$$\tau_d (\text{towards}) = L(1/v_r - 1/\alpha), \quad 3.11$$

where L is the length of the fault, v_r is the rupture velocity and α is the P-wave velocity.

If the rupture propagates away from the receiver then

$$\tau_d (\text{away}) = L(1/v_r + 1/\alpha). \quad 3.12$$

It is assumed that the length of a fault is related to the size of the earthquake, and

$$\Delta\sigma = 7M_o / 16 r^3 \quad 3.13$$

is an appropriate measure for the relation of the moment M_o to rupture area (Brune, 1970)

where r is the radius of a circular rupture. Equations 3.10-3.13 offer direct estimates of the corner frequency and its relation to rupture characteristics such as the stress drop, rupture size and rupture velocity. For example, three earthquakes having magnitude 0.8, 1.2 and 1.8 M_L are converted to moment release (Kanamori, 1977) using the relation

$$M_w = (2/3)\text{Log}_{10}M_o - 10.7 \quad 3.14$$

and assuming $M_L = M_w$. Next, the rupture area is determined at several stress drop values (Equation 3.13), which in turn are converted to an average rupture duration (Equation 3.11 and 3.12) and the corner frequency (Equation 3.10). For this analysis (Figure 3.10), the stress drop varies from 5-150 bars ($0.5\text{-}15 \times 10^6$ dyne/cm²), the P-wave velocity is 5.0 km/s, and the rupture velocity is 0.8 times the S-wave velocity of 2.9 km/s. The average stress drop for intra-continental earthquakes is known to be about 100 bars while the stress drop for inter-continental earthquakes is about 30 bars (Harr et al., 1984). The analysis suggests that earthquakes in the study area should have corner frequencies above 40 Hz for the majority of the data. However, a small proportion of the data might be contaminated by lower corner frequencies associated with very low stress drops, very slow rupture velocities or strong directivity effects (Equation 3.5 and 3.6). It is surmised that high frequency rolloffs of Figure 3.8 and 3.9 result predominantly from the attenuation of earthquake rays propagating from the common source areas. If so, then the spectral rolloff maps in Figure 3.8 and 3.9 represent bulk attenuation measurements which are mapped at the source.

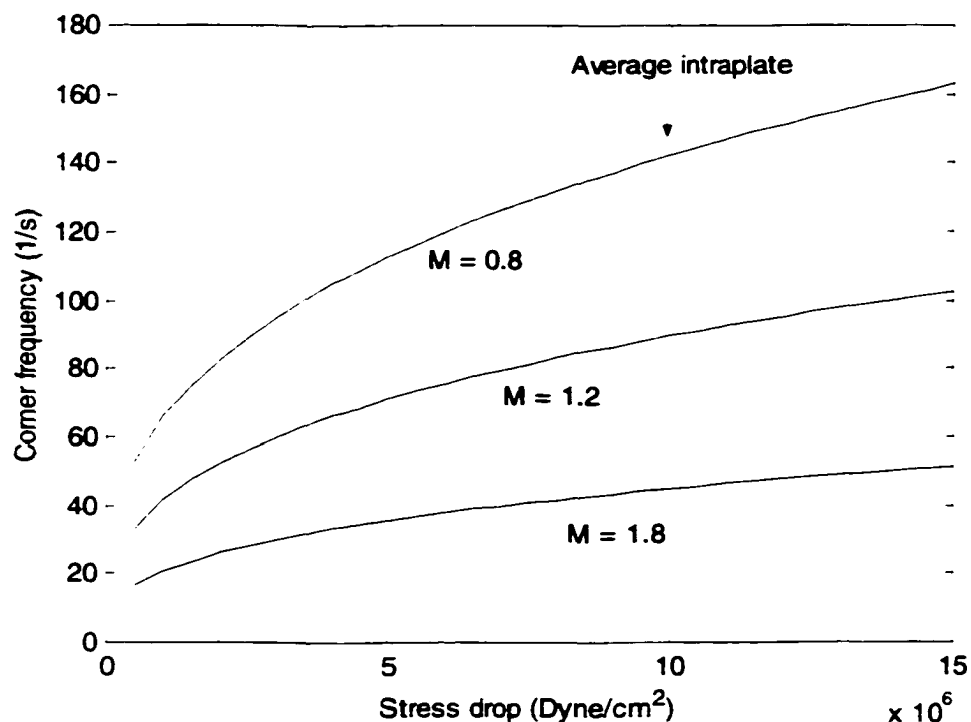


Figure 3.10: Stress drop (dyne/cm²) versus corner frequency (Hz) for three earthquakes having magnitude 0.8 M_L (top), 1.2 M_L (middle) and 1.8 M_L (bottom). The corners are based on a simple Haskell source model with P-velocity of 5.0 km/s, S velocity 2.8 km/s, and an earthquake rupture velocity of 2.25 km/s. The corner frequency is above the frequency of interest (3.91-13.28 Hz) for reasonable stress drops. The abscissa range is from 5 to 150 bars (0.5-50x10⁶ dyne/cm²). The average stress drop for an intraplate earthquake is about 100 bars.

3.4 Data for inversion

In this study, 327 earthquakes and 2977 spectra are available for inversion. These data were corrected for the site amplification factor and then the spectra for each earthquake were reexamined to determine the corner frequency. Application of the site amplification correction (Figure 3.4) allows examination of the corner frequency from earthquakes with fewer high quality spectra. Thus, earthquakes with three or more spectra with 2X signal to noise ratios are visually examined, and each earthquake whose log-averaged spectra rolled off at a rate greater than $1/\omega^2$ in the frequency range 3.91-13.28 were excluded from the inversion. Then, for the surviving spectra, the log amplitude of the available spectra were determined and all available spectra were regressed by least-squares for the slope (t^*). The quality of the regression is determined by calculating a 95% confidence interval (Kreyszig, 1993) for the slope. The visual analysis and corner frequency filtering left 230 earthquakes and 1301 rays for inversion.

The approximate inverse solver LSQR (Paige and Saunders, 1982a and 1982b) is applied to determine the inverse of the matrix system and a ray tracer (Um and Thurber, 1987) to determine the ray paths through the velocity model. For each ray, a t^* value and the standard error is available. The latter is applied as a weighting constraint for each t^* value (i.e. $W = 1/\sigma$). Thus, like the P-velocity inversion (Chapter 2), the matrix system is given by

$$\begin{bmatrix} WC \\ \lambda L \end{bmatrix} \delta B = \begin{bmatrix} W \delta t^* \\ 0 \end{bmatrix} \quad 3.9$$

where λ is the damping of the system, L is the two-dimensional Laplacian, and C is the matrix of travel-times. This weighted damped least-squares system is inverted for the unknown I/Q values (δB). The choice of a damping parameter, λ , for the attenuation inversion is somewhat arbitrary. In their inversion, Lees and Lindley (1994) tested several trial damping values and then chose the model providing a reasonable compromise between residual reduction and model smoothness. Their primary goal was to model structural features having the same wavelength as that of their velocity inversion. At Katmai, the same methodology is applied, producing a 66.9% model reduction from a damping of $\lambda = 60$.

3.5 Procedural outline

The following outline provides the method used in the attenuation inversion study.

The procedures include:

- 1) Select and process earthquake waveform.
 - 1a) Visually inspect event to ensure it is within instrumental dynamic range (exclude clipped events).
 - 1b) Calculate P and pre-event noise spectra for events surviving step 1a.
 - 1c) Deconvolve instrument response.
 - 1c) Save spectra and all other spectra for given earthquake in database.
- 2) Determine site amplification.

- 2a) For an earthquake, correct spectra for geometric spreading, plot spectra and associated log averaged spectrum.
- 2b) For earthquakes with 5 spectra above noise criterion, divide each spectrum by the log average spectrum. The result is amplification of station relative to earthquake.
- 2c) Save amplification data, and repeat step 2 for all earthquakes.
- 3) Calculate site amplification factor for totality of data in step 2.
- 4) Inspect spectra of step 2 within source regions.
- 5) Deconvolve site amplification factor determined in step 3 for all spectra.
- 6) Examine site and instrument corrected spectra.
 - 6a) Plot spectra for all earthquakes with 3 or more spectra above the noise criterion.
 - 6b) Inspect the log averaged spectra for corner frequency. Exclude all earthquakes with frequency rolloffs greater than $1/\omega^2$.
 - 6c) Calculate the slope (t^*) and standard error of the amplitude-frequency relation in frequency band of interest.
- 7) Invert the slope data.
 - 7a) Relocate attenuation study earthquakes using final velocity model from Chapter 2.
 - 7b) Trace rays using ray-bending techniques of Chapter 2.
 - 7c) Invert t^* data of step 6c for three-dimensional attenuation structure ($1/Q$).
- 8) Conduct error analysis using hitcount and jackknife procedures.

3.6 Errors

Errors associated with generalized attenuation inversions are complex and difficult to characterize. Such errors as outlined by Scherbaum (1990) and Lees and Lindley (1994) include: 1) assumptions about source models, 2) errors in the velocity model, 3) tradeoff between F_c and t^* , 4) ambiguity between intrinsic and scattering attenuation, 5) source directivity and radiation effects, 6) uncorrected site effects and 7) frequency dependence in Q . These issues are addressed in order below.

Source model assumptions (issue 1) do not enter into the inversion because this study makes no assumption about the roll off characteristics of the source. It is assumed that the source spectrum is flat below the corner frequency; a common feature of many source models. Velocity model errors (issue 2) are addressed by first inverting the data for the P-wave velocity (Chapter 2), and then inverting for the attenuation. Errors associated with the velocity model are generally small as shown in the jackknife analysis. The largest velocity model errors occur on the outer margins of the velocity model. The problem with tradeoff between F_c and t^* (issue 3) is not an issue in this inversion method because the corner frequency is not a parameter of the regression for t^* .

The question of intrinsic and scattering attenuation (issue 4) is not addressed in this study, or in prior attenuation inversion studies. Single station methods for separating intrinsic and scattering attenuation have been conducted for S-waves from the post-S coda (Frankel, 1991). The applicability of this method for a P-wave inversion study is

doubtful. Instead it is probable that the observed Q is a combination of both types of attenuation. Problems with source directivity and radiation patterns (issue 5) were not directly addressed. However, the source spectra were examined with respect to latitude, longitude and depth (Figure 3.6-3.7) towards a better understanding of these effects. One potential corner frequency anomaly was observed for a small earthquake cluster located at Angle Creek (Figure 3.6-4). Source corner frequencies in this cluster are anomalously low for a subset of the data. Such events are excluded from the inversion by visual inspection and should not bias the final inversion. Site effects (issue 6) are minimized by deconvolving the site amplification factor for all stations. We also limit the bandwidth of interest to avoid systematic and non-linear effects of the source, path and site. The frequency dependence of Q (issue 7) is difficult to assess. Aki (1980) found that Q increased with frequency by f^n ($0.5 < n < 0.8$) for S-waves in both Japan and central Asia. Patane et al. (1994) found that Q in the vicinity of Mt. Etna varied with frequency by ($0.5 < n < 1.6$). These studies used single station methods, which are not directly applicable to the multi-station inversion method used here. If higher frequencies are less attenuating as suggested by these studies, then the inversion method will incorrectly estimate the attenuation in the frequency range of interest. Assessing the frequency dependence of Q in the Katmai region might be a fruitful area of study in the future. In summary, the method applied in this study attempts to minimize the effect of source corner frequencies on the data.

3.7 Results

The primary results of the inversion include a broad region of high attenuation located at Katmai pass and extending from Martin volcano to Katmai caldera (Figures 3.11-20). The detailed interpretations of the results are saved for Chapter 6 where they are discussed in context with three dimensional b -value, velocity inversion and prior gravity, interferometry and seismology results. This section will concentrate on the observations, resolution and errors of the attenuation inversion. Attenuation results are shown for layer 1 (Figure 3.11), layer 2 (Figure 3.13), layer 3 (Figure 3.15), layer 4 (Figure 3.17), layer 5, (Figure 3.19) and presented in $1/Q$ so higher values on the color scale represent higher attenuation. In the discussion, attenuation will be given as $1/Q$ with the actual Q values offered in parentheses where appropriate. The resolution and errors of the inversion are estimated for layer 1 (Figure 3.12), layer 2 (Figure 3.14), layer 3 (Figure 3.16), layer 4 (Figure 3.18) and layer 5 (Figure 3.20). As with the prior velocity inversion (Chapter 2) the resolution of the attenuation inversion is controlled by raypath distribution, model parameterization and smoothing. Unlike the velocity inversion, a meaningful method of assessing the combined effects of model parameterization and smoothing (i.e. checkerboard) is not available. Instead, the resolution of the system is assessed using hitcount maps (Figure 3.12a, Figure 3.14a, Figure 3.16a, Figure 3.18a, Figure 3.20a) showing the number of rays traversing a given block. This resolution method is identical to that followed by Lees and Lindley (1994).

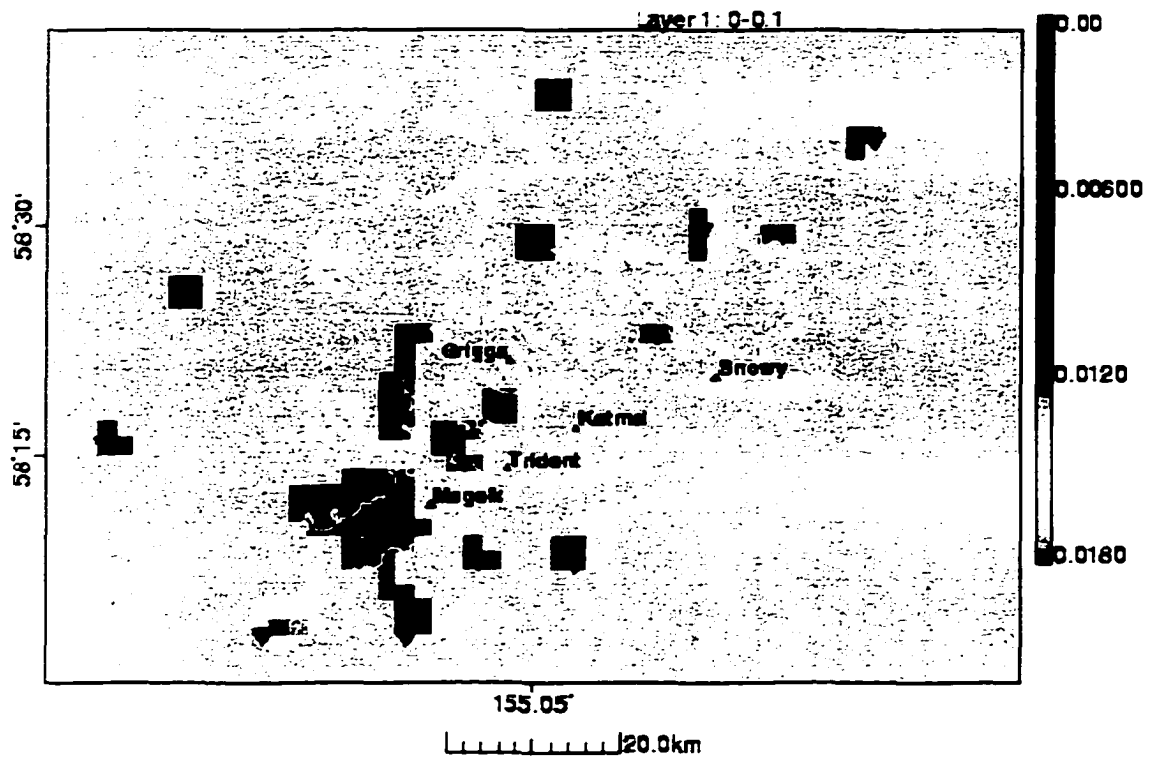
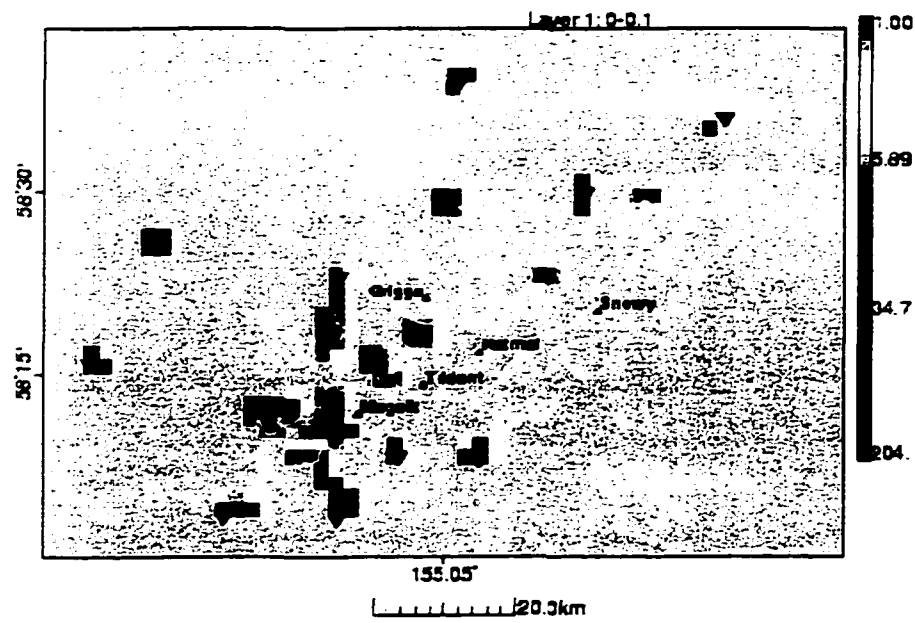


Figure 3.11: Attenuation model for layer 1 (-3.0-0.0 km depth). The color scale is expressed in unitless $1/Q$.

a)



b)

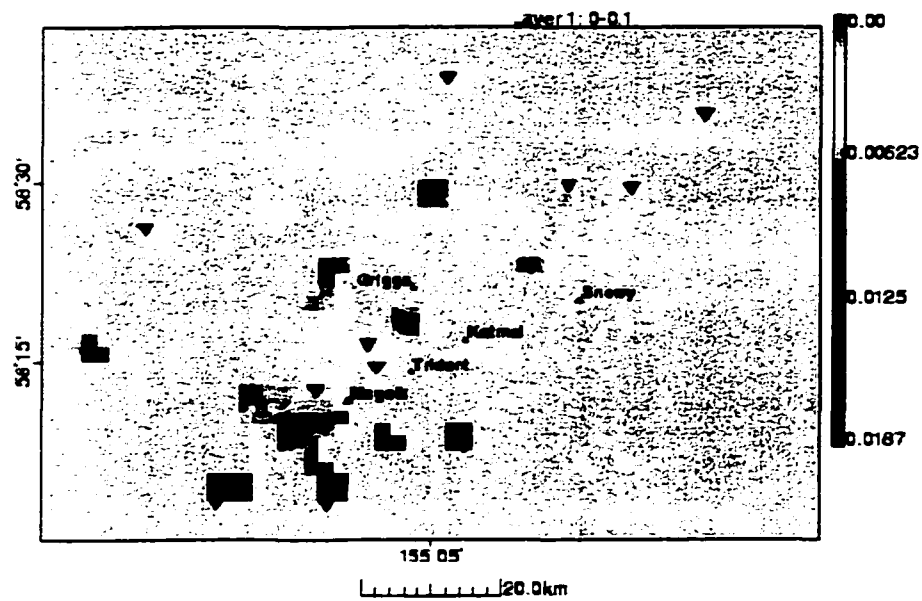


Figure 3.12: Hitcount map (a) and jackknife (b) errors for layer 1, (-3.0 to 0.0 km depth range). Color scale is number of events (a) and unitless $1/Q$ (b).

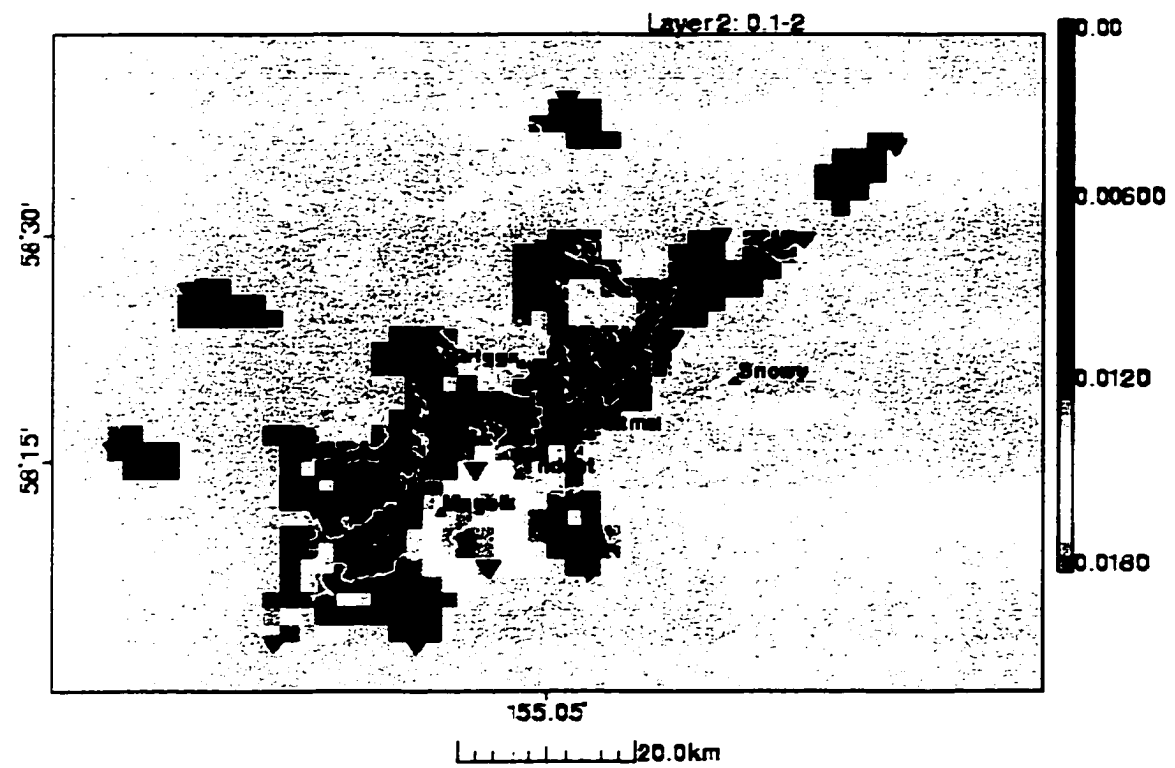
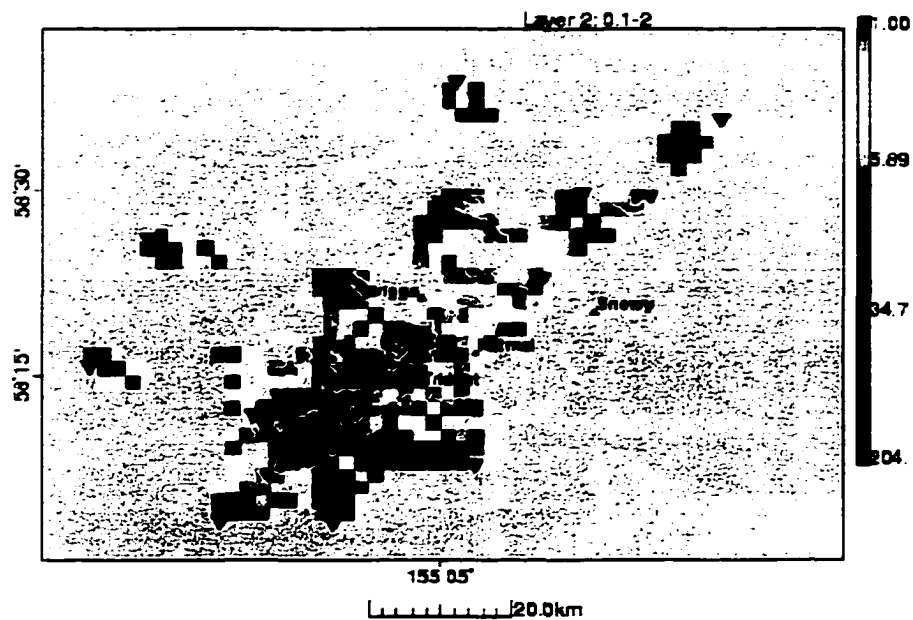


Figure 3.13: Attenuation model for layer 2 (0.0-2.0 km depth). The color scale is expressed in unitless $1/Q$.

a)



b)

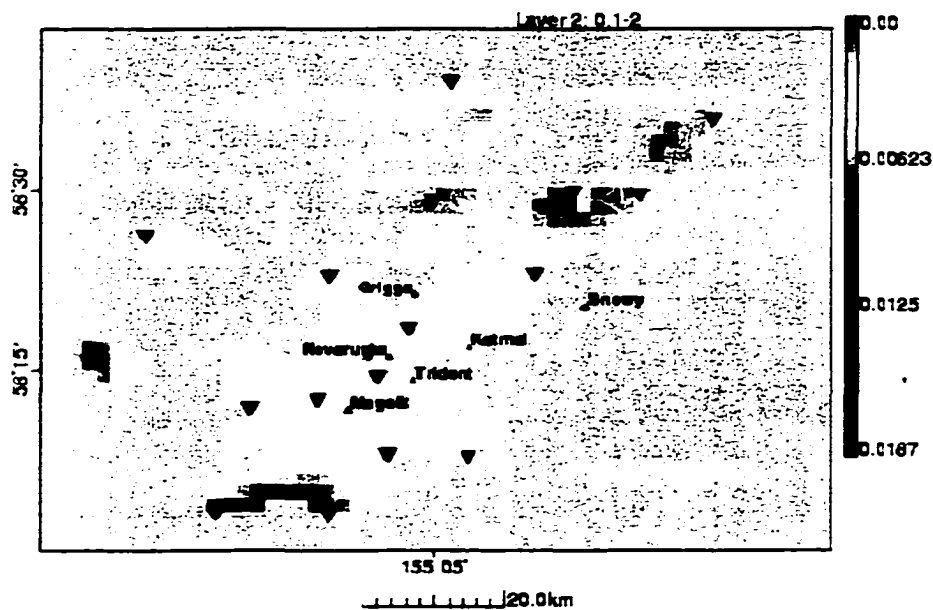


Figure 3.14: Hitcount map (a) and jackknife errors (b) for layer 2, (0.0 to 2.0 km depth range). Color scale is number of events (a) and unitless $1/Q$ (b).

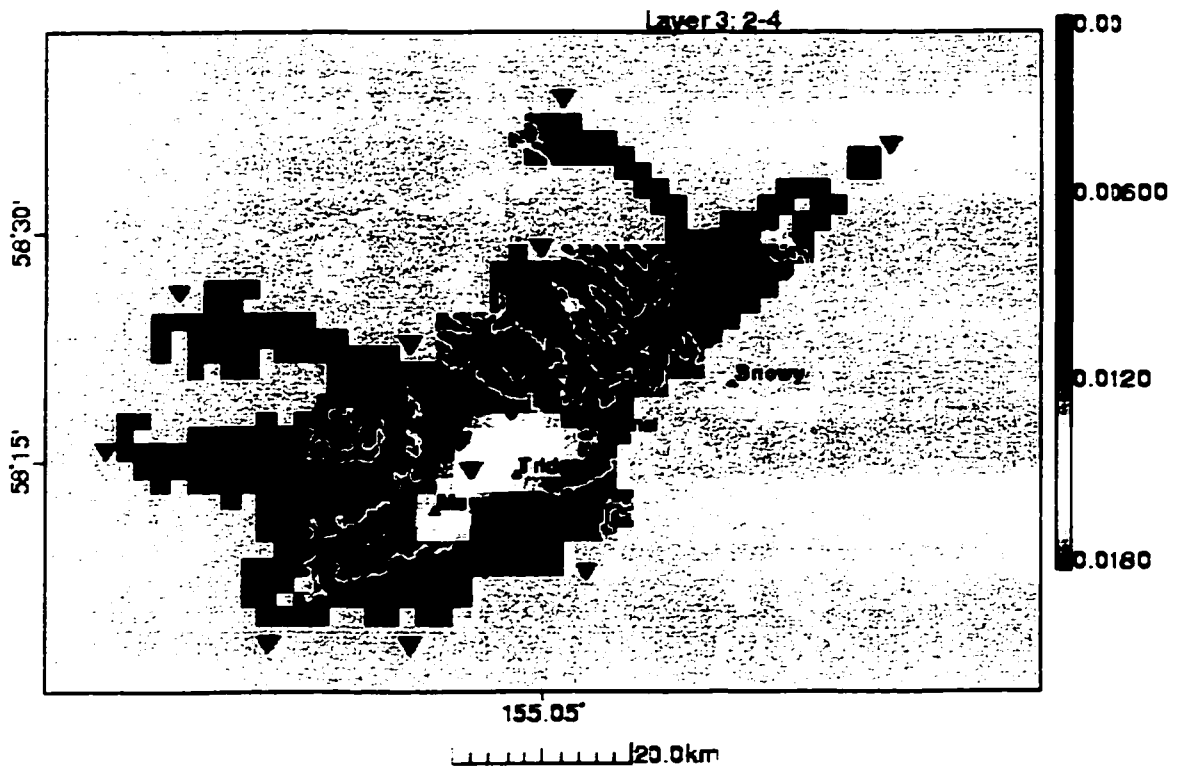
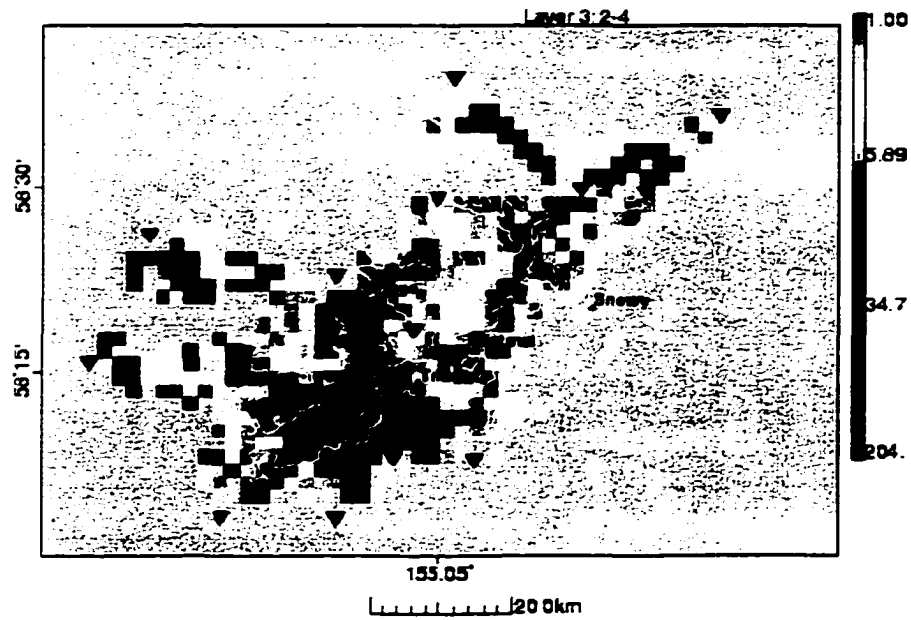


Figure 3.15: Attenuation model for layer 3 (2.0-4.0 km depth). The color scale is expressed in unitless $1/Q$.

a)



b)

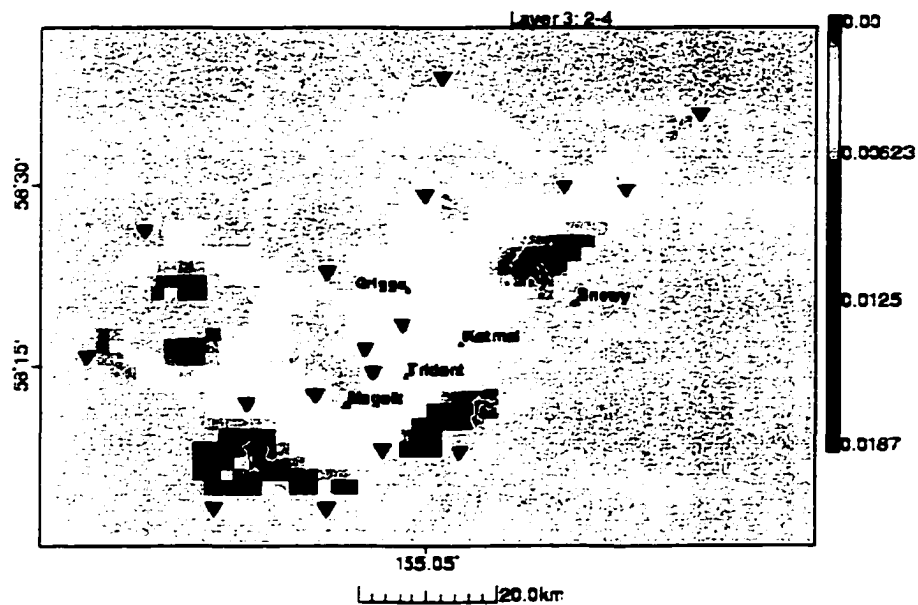


Figure 3.16: Hitcount map (a) and jackknife errors (b) for layer 3, (2.0-4.0 km depth range). Color scale is number of events (a) and unitless $1/Q$ (b).

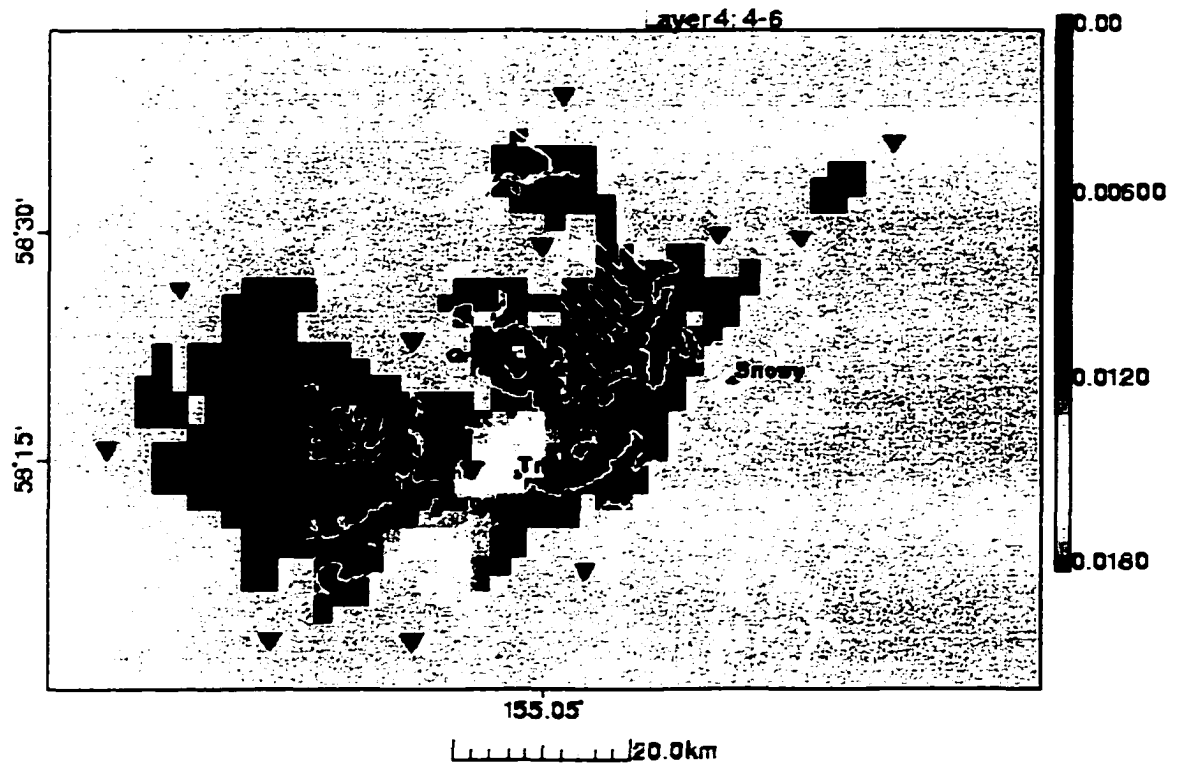
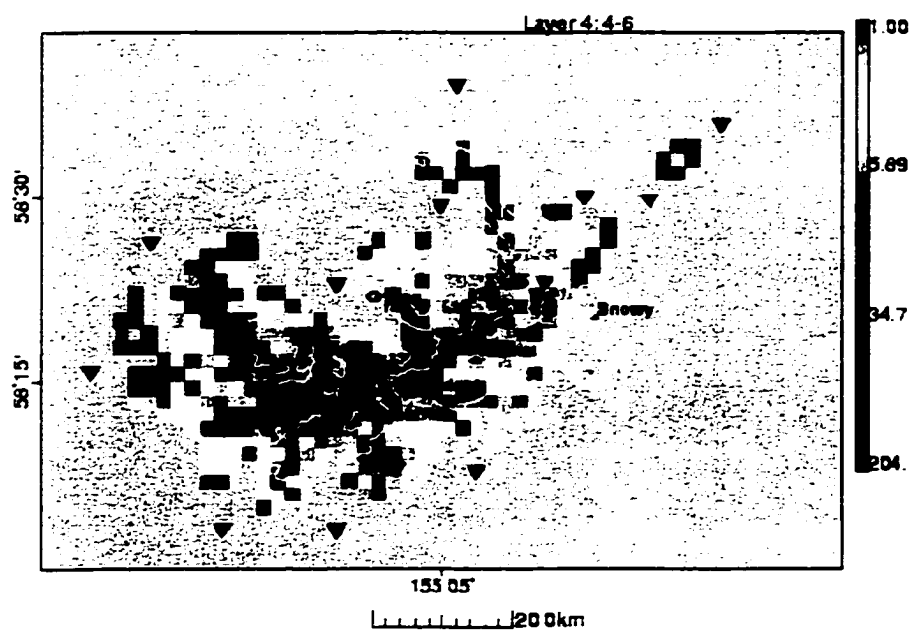


Figure 3.17: Attenuation model for layer 4 (4.0-6.0 km depth). The color scale is expressed in unitless $1/Q$.

a)



b)

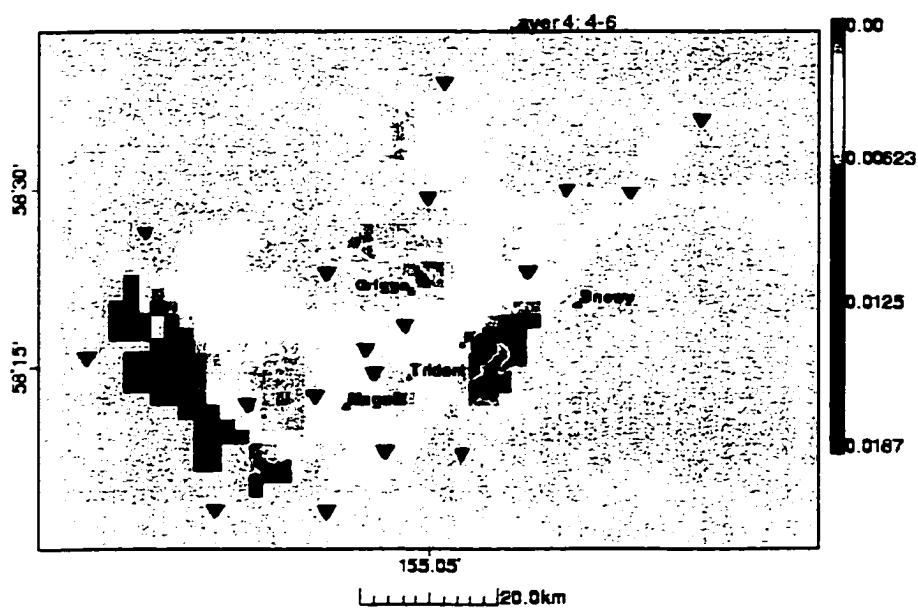


Figure 3.18: Hitcount map (a) and jackknife errors (b) for layer 4, (4.0-6.0 km depth range). Color scale is number of events (a) and unitless $1/Q$ (b).

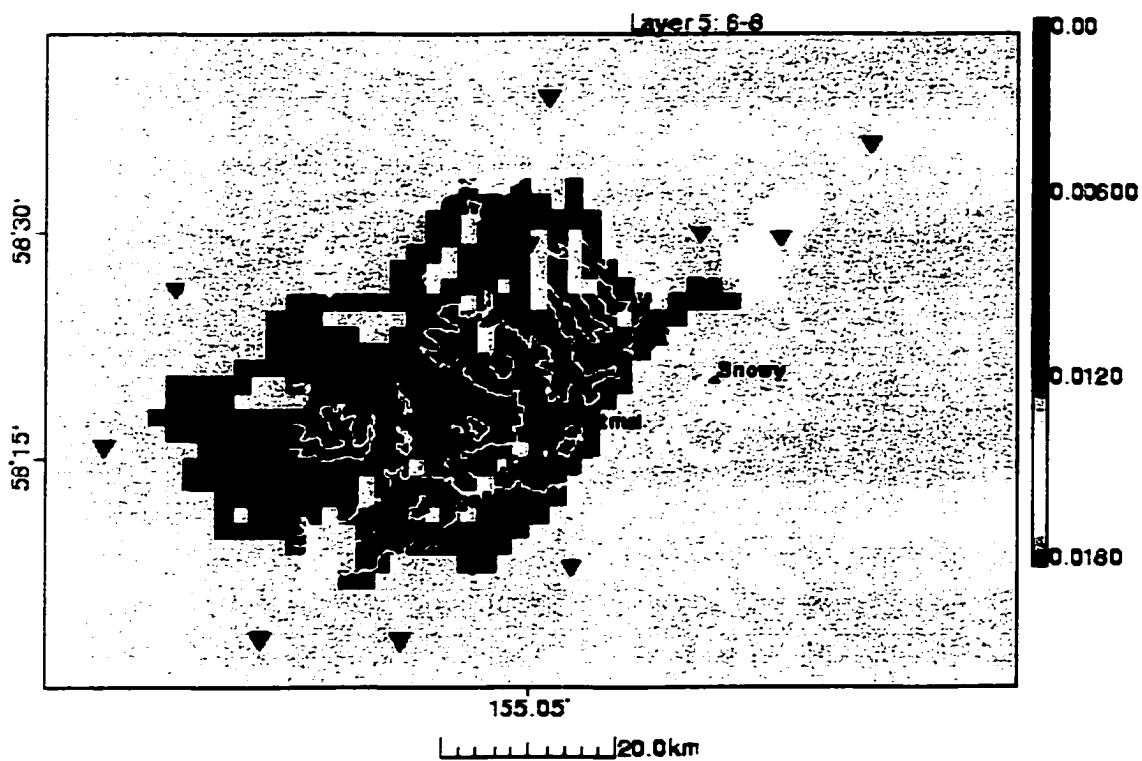
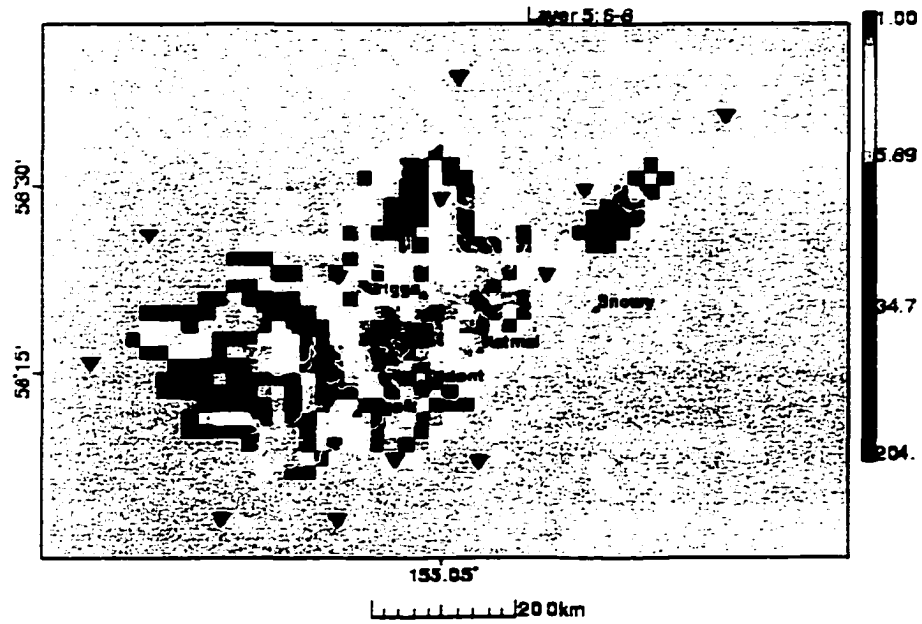


Figure 3.19: Attenuation model for layer 5 (6.0-8.0 km depth). The color scale is expressed in unitless $1/Q$.

a)



b)

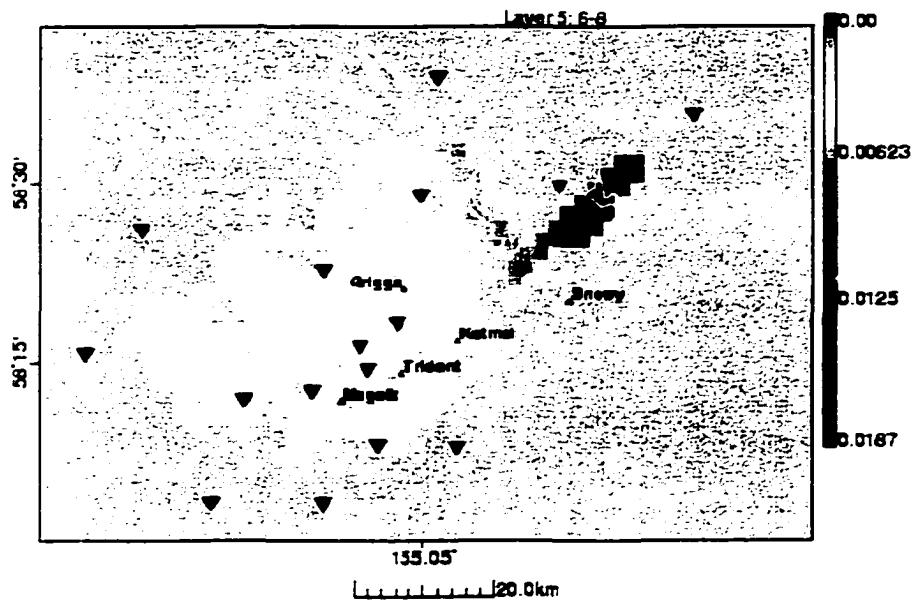


Figure 3.20: Hitcount map (a) and jackknife errors (b) for layer 5, (6.0-8.0 km depth range). Color scale is number of events (a) and unitless $1/Q$ (b).

The errors associated with the attenuation inversion are determined in a manner described in Chapter 2 using the method of Lees (1989) and Lees and Lindley (1994). For the jackknife method, the existing dataset was subdivided into 20 subsets each containing $(n - n/k)$ rays and each subset is inverted separately producing a $1/Q$ measurement for each block. The 20 inversions are averaged producing statistics for each hit block. Regions with large variability (yellows and greens) are not well constrained and should be viewed with caution (Figure 3.12b, Figure 3.14b, Figure 3.16b, Figure 3.18b and Figure 3.20b). A third consideration with the inversion is the variability of the azimuth and take-off angle of impinging rays, also called ray anisotropy. Regions of the model with uni-directional rays have poor model resolution even though they may have high hit counts. For layer 1 (Figure 3.12a) where rays traverse from depth to the stations in one direction, the model results may be poorly constrained.

Based on both hit count and jackknife errors, the best resolved regions appear to be in layers 1-4 associated with the 0-6 km depth range where large continuous blocks of blue, green and magenta are observed in the hitcount plots (Figure 3.12a, Figure 3.14a, Figure 3.16a and Figure 3.18a). Jackknife error analysis further suggests that the model is less well resolved in the northern and southern parts of layer 2 and 3 (Figure 3.12b and Figure 3.16b) south of Martin and Mageik clusters where the resolution appears to degrade. The attenuation model is interpreted in the 0-6 km depth region (Figure 3.11a and b) where hitcounts are greater than 5 and the jackknife errors are small ($1/Q < 0.005$). In this restricted volume, relatively high attenuation 0.008-0.018 ($Q \sim 55-125$) is observed in the 0-6 km range centered on Katmai pass and extending along the volcanic

axis from Martin volcano to Katmai caldera. The anomalous high attenuation extends northward to Griggs volcano which has $1/Q = 0.01$ ($Q = 100$). Higher attenuation ranging from 0.01-0.000 ($100 < Q < \infty$) is observed outboard of the volcanic axis and at depths greater than 6 km below sea level. The depth of the anomaly appears to be above 6 km depth (layer 5; Figure 3.19) where $1/Q$ is about $0.000 < 1/Q < 0.001$ ($1000 < Q < \infty$). This observation should be viewed with caution however because (Figures 3.20a and b) the volume below 6 km is not traversed by many rays.

3.8 References

Aki, K., Attenuation of shear-waves in the lithosphere for frequencies from 0.05 to 25 Hz., Phys. Earth Planetary Int., 21, 50-60, 1980.

Boatwright, J., A spectral theory for circular seismic sources; simple estimates of source dimension, dynamic stress drop, and radiated seismic energy, Bull. Seis. Soc. Amer., 70, 1-27., 1980.

Brune, J. N., Tectonic stress and the spectra of seismic shear waves from earthquakes, J. Geophys. Res., 75, 4997-5005, 1970.

Dahlen, F.A., On the ratio of P-wave to S-wave corner frequencies for shallow earthquake sources, Bull. Seis. Soc. Amer., 64, 1159-1180, 1974.

Evans, J.R. and Zucca, J.J., Active high-resolution tomography of compressional wave velocity and attenuation structure at Medicine Lake volcano, Northern California Cascade range, 93, 15016-15036, 1988.

Frankel, A., The effects of attenuation and site response on the spectra of microearthquakes in the Northeastern Caribbean, 72, 1379-1402, 1982.

Frankel, A., Mechanisms of seismic attenuation in the crust: Scattering and anelasticity in New York State, South Africa, and southern California, *J. Geophys. Res.*, 96, 6269-6289, 1991.

Gladwin, M.T. and Stacey, F.D., Anelastic degradation of acoustic pulses in rocks, *Phys. Earth Planet. Inter.*, 8, 332-336, 1974.

Harr, L.C., Fletcher, J.B., Mueller, C.S., The 1982 Enola, Arkansas, swarm and scaling of ground motion in the eastern United States, *Bull. Seis. Soc. Amer.*, 74, 2463-2482, 1984.

Kanamori, H., Energy release in great earthquakes, *J. Geophys. Res.*, 82, 2981-2987, 1977.

Kienle, J., Depth of the ash flow deposits in the Valley of Ten-Thousand Smokes, *Geophys. Res. Lett.*, 18, 1533-1536, 1991.

Kreyszig, E., *Advanced engineering mathematics*, 7th ed., John Wiley and Sons, 1270 p., 1993.

Lees, J.M., *Seismic tomography in Western Washington*, Ph.D. Thesis, 173 p., Univ. of Wash., Seattle, 1989.

Lees, J.M. and Lindley, G.T., **Three-dimensional attenuation tomography at Loma Prieta: Inversion of t^* for Q** , *J. Geophys. Res.*, **99**, 6843-6863, 1994.

Paige, C.C. and Saunders, M.A., **LSQR: An algorithm for sparse linear equations and sparse least squares**, *ACM Trans. Mathematical Software*, **8**, 43-71, 1982a.

Paige, C.C. and Saunders, M.A., **LSQR: Sparse linear equations and least squares problems**, *ACM Trans. Mathematical Software*, **8**, 195-209, 1982b.

Patane, D., Ferrucci, F., Gresta, S., **Spectral features of microearthquakes in volcanic areas: Attenuation in the crust and amplitude response of the site at Mt. Etna, Italy**, *Bull. Seis. Soc. Amer.*, **84**, 1842-1860, 1994.

Scherbaum, F., **Combined inversion for the three-dimensional Q structure and source parameters using microearthquake spectra**, *J. Geophys. Res.*, **95**, 12423-12438, 1990.

Solomon, S.C. and Toksoz, M.N., **Lateral variation of attenuation of P and S waves beneath the United States**, *Bull. Seis. Soc. Amer.*, **60**, 819-838, 1970.

Tonn, R., **Comparison of seven methods for the computation of Q** , *Phys. Earth and Planet. Int.*, **55**, 259-268, 1989.

Um, J. and Thurber, C., A fast algorithm for two-point seismic ray tracing, *Bull. Seis. Soc. Amer.*, 77, 972-986, 1987.

Wittlinger, H., Haessler, H., Granet, M., Three-dimensional inversion of Q_p from low magnitude earthquake analysis, *Annales Geophysicae*, 1, 427-438, 1983.

Wu, H. and Lees, J.M., Attenuation structure of Coso geothermal area, California, from wave pulse widths, 86, 1574-1590, 1996.

Zucca, J.J. and Evans, J.R., Active high-resolution compressional wave attenuation tomography at Newberry volcano, central Cascade range, *J. Geophys. Res.*, 97, 11047-11055, 1992.

Chapter 4: Seismicity and *b*-values at the volcanoes of Katmai National Park, Alaska; July 1995-December 1997

4.0 Abstract

Upper-crustal seismicity located within Katmai National Park occurs mainly within four distinct clusters originating near Martin-Mageik volcanoes, Trident volcano, Katmai caldera and Snowy volcano. Analyses of earthquake frequency-magnitude distributions reveal high *b*-values beneath Martin-Mageik (~1.5), normal *b*-values at Trident volcano (~1.0), and intermediate *b*-values at Katmai caldera (~1.3) for all seismicity occurring between July 1995 and December 1997. Detailed analyses of subsets of *b*-values and hypocenter locations at Martin-Mageik reveal a temporal increase in *b*-value associated with an increase in the maximum depth of seismicity. The changes occurred during a shallow earthquake swarm beneath Mageik volcano between October 16 and 25, 1996 and again in November-December 1997. Before the swarm, the weighted least squares *b*-value was 1.01 at Martin-Mageik, increased to 1.59 during the swarm and remained anomalously high until April 1997. The corresponding maximum depth of seismicity is generally less than 5 km for well located earthquakes occurring after September 18, 1996, but shifted to ~10-km during both the October 1996 swarm and the November-December 1997 period. The November-December 1997 event is not associated with an increase in the rate of seismicity or the *b*-value. The October 1996 swarm had, a cumulative moment release of 5.0×10^{20} dyne-cm, and decayed from a peak

rate of 110 events per day with a modified Omori law p -value of 1.06 ± 0.11 . Modeling by the flow law with a 10 km depth limit for seismicity suggests that temperature gradients are on the order of $20\text{--}40^\circ\text{C km}^{-1}$, in agreement with the p -value estimate. We infer that a simple pressurizing intrusion was not associated with the October swarm because higher stresses should increase seismicity and lower the b -value, the opposite of what we observed. Alternatively, an actively degassing intrusion would reduce the effective stress and increase the b -value at shallow depths while the increased stress would induce seismicity at depth. Surface temperature measurements taken at the Mageik crater lake in July 1995, and again in July 1997, revealed an increase of about 10°C in the lake water temperature, consistent with a degassing intrusive event.

This chapter is excerpted from Jolly A. D. and McNutt, S. R., 1999, Seismicity at the volcanoes of Katmai National Park; July 1995-December, J. Volc. and Geotherm. Res., 93, 173-190, 1999.

4.1 Introduction

A recently installed, permanent, telemetered seismic network in the vicinity of the Katmai group of volcanoes, Alaska peninsula (Figure 4.1), permits us to characterize selected features of the seismicity for the first time. Spatial and temporal analyses of earthquakes recorded between July 1995 and December 1997 in the Katmai region was conducted. Rates of seismicity, spatial clustering, and frequency-magnitude distributions were completed with emphasis on the activity before, during, and after a swarm in October 1996 beneath Mageik volcano.

At Katmai, earthquakes are observed in four clusters: Martin-Mageik, Trident, Katmai caldera, and Snowy (Figure 4.2). At Martin-Mageik volcanoes we observed both an increase in the b -value (the slope of the frequency-magnitude relation) and a decrease in the maximum depth of seismicity following the 1996 earthquake swarm. No anomalous b -values were observed near the adjacent volcanoes Novarupta, Trident, or Katmai caldera.

Although seismicity is examined, deformation in the volcanic environment may occur as a response to either regional or local stress changes, or both. The predominant mode of deformation, either plastic flow or brittle failure, is controlled by the material properties of the rock and the applied stress. In the crust, the transition between brittle failure and plastic flow is expressed by the occurrence of earthquakes which are constrained above a seismogenic depth of typically 10 to 20 km. Below this brittle-ductile transition, ever-increasing burial temperatures and rock confining pressures reduce rock strength and induce plastic flow (Sibson, 1982; Scholz, 1988). Rock strength may be reduced in volcanic environments where thermal gradients are steeper, resulting in shallower maximum earthquake depths during times of volcanic quiescence (Stephens

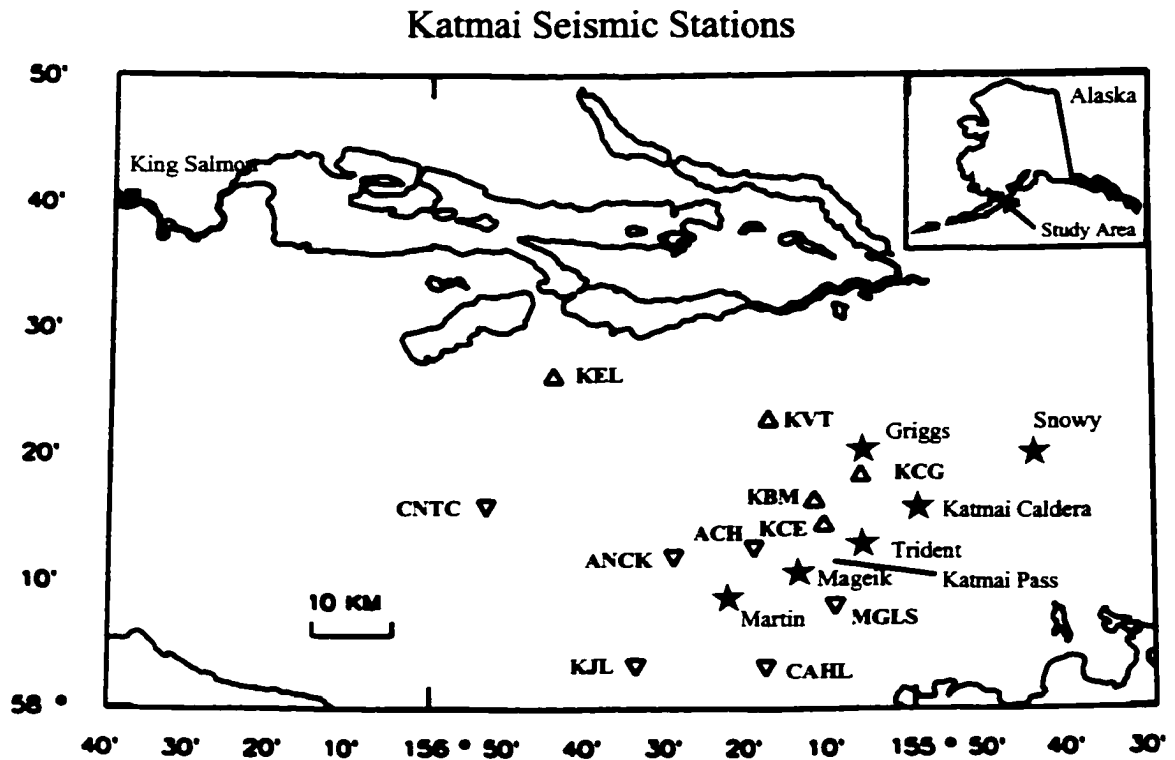


Figure 4.1: Index map of the study area in the Alaska Peninsula, south central Alaska, and station map showing the locations of seismic stations used in this study. Open triangles are stations which began operation July 27, 1995; solid inverted triangles are stations which began operation after September, 1996. Stars show the locations of major volcanoes in the region.

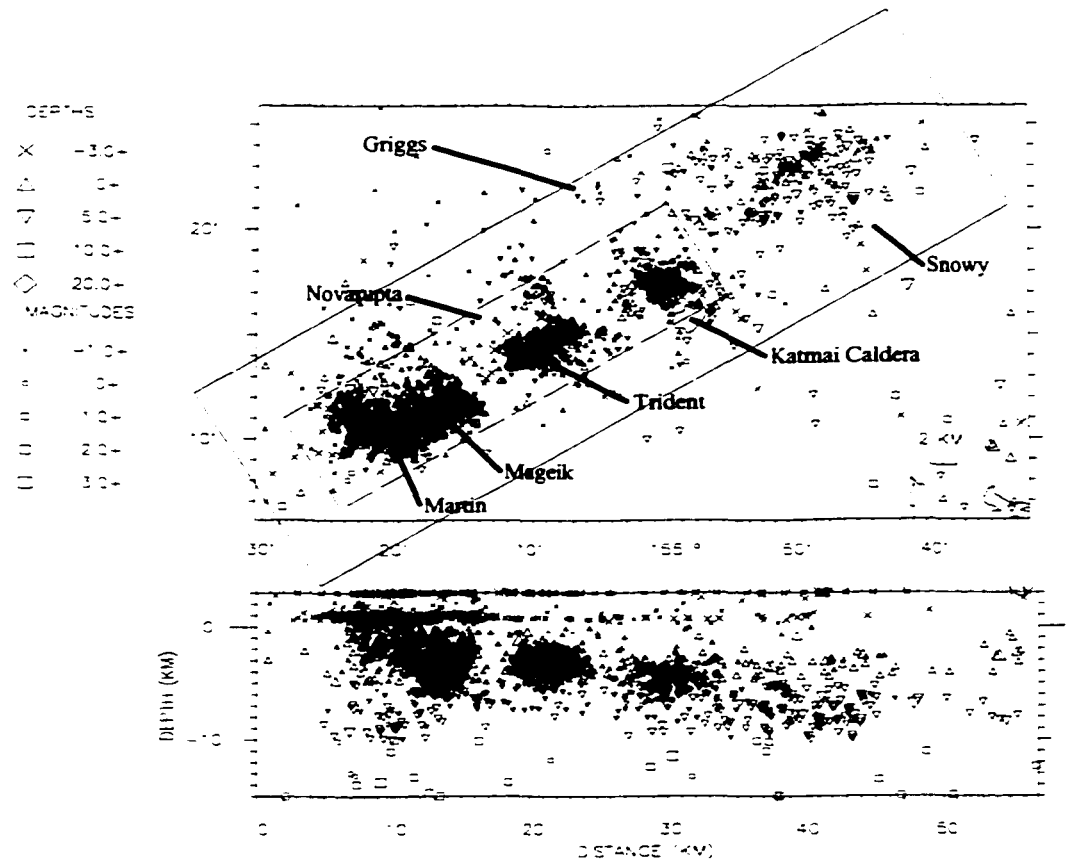


Figure 4.2: Seismicity map and WSW-ENE cross-section of earthquakes located in the region between July 27, 1995 and December 31, 1997. Crosses represent earthquakes from -3.0 to 0.0 km, triangles 0.0 km to 5.0 km, inverted triangles 5.0 to 10.0 km, squares 10.0 km to 20.0 km, and diamonds deeper than 20.0 km. Larger magnitudes are given by larger symbols. Solid box represents area of space-time plot of Figure 4.3. Dashed box represents area used in b -value cross-section of Figure 4.6.

et al., 1984; Hill, 1992; Jolly et al., 1994). Such quiescent zones may become illuminated by seismicity when magma is injected and stresses are concentrated along volcanic conduits (e.g., Power et al., 1995; Hill, 1996). Water content may also play an important role in the depth of the brittle-ductile transition (Kirby and Kronenberg, 1987; Hill, 1992) because rock strength is reduced both in the brittle and ductile layers when the water content is increased, thereby increasing the potential for rock to flow plastically. Such a mechanism might apply to volcanic environments where high stress concentrations and high deformation rates may increase rock fracture resulting in increased permeability and fluid mobility. These would then appear as systematic differences in seismicity.

Seismicity is expressed by the occurrence of many more small earthquakes than large ones, following a power law given as $\text{Log } N = a - bM$ (Gutenberg and Richter, 1954) where N is the cumulative number of earthquakes having magnitude greater than M , and a and b are constants. The slope b is found to vary in predictable ways in both regional tectonic (Anderson et al., 1980; Wiemer and Benoit, 1996) and volcanic environments (Wiemer and McNutt, 1997; Wyss et al., 1997; Power et al., 1998; Wiemer et al., 1998). Higher relative b -values are shown to result from: 1) high thermal gradients (Warren and Latham, 1970), 2) lowering of the magnitude of applied shear stress (Scholz, 1968), 3) decreased effective stress (or high pore pressure; Wyss, 1973), or 4) high material heterogeneity (Mogi, 1962). In addition, non-fractal scaling or scale saturation (Scholz, 1982; Pacheco et al., 1992) or systematic biases associated with magnitudes (Zuniga and Wyss, 1995) may modify the frequency-magnitude distribution.

The b -value and depth data is used to place constraints on the likely processes and sequence of events before, during, and after the October 1996 swarm near Mageik volcano.

4.2 Previous Studies

The subsurface structure in the vicinity of Novarupta dome and Katmai caldera, Alaska (Figure 4.1) has been a topic of great scientific interest in the past several decades (e.g., Matumoto and Ward, 1967; Kienle, 1970; Matumoto, 1971; Hildreth, 1987; Fierstien and Hildreth, 1982; Ward et al., 1991; Abe, 1992). This interest is spurred in large part by the June 6th-9th, 1912 eruption which produced $\sim 30 \text{ km}^3$ of eruptive materials (Hildreth, 1987) and induced the collapse of Mount Katmai (located $\sim 10 \text{ km}$ to the east of Novarupta). The spatial offset between the eruptive vent (Novarupta) and the caldera collapse site (Katmai) requires a magma system of large lateral extent. Matumoto and Ward (1967), Kubota and Berg (1967) and Matumoto (1971) mapped the location of the magma system in the area. They observed an attenuation of S-waves in the region. Kienle (1970), observed a -35 Mgal gravity low in the vicinity of Katmai pass (Figure 4.1). Later, Ward et al. (1991) observed travel-time delays as large as 0.9 seconds for a seismic station south of Katmai pass. These travel-time delays depended on azimuth and were greatest to the north of the station. Recently, Lu et al. (1997) observed anomalies from SAR interferometric images acquired between 1993 and 1995. They interpreted the anomalies as representing significant inflation (8 cm) in the vicinity of Trident volcano. From the uplift gradient, Lu et al. (1997) determined a pressure source located 0.8 to 2.0 km below the surface. The observed anomaly lies outside an established EDM/GPS net (Kleinman et al., 1997) which yielded no significant deformation for the 1991-1993 period.

4.3 Seismic data 1995-1997

Beginning late July 1995, the Alaska Volcano Observatory (AVO) reestablished 5 stations, with 7 components (Figure 4.1), of a 16 station, 20 component array originally operated by the United States Geological Survey between September 1987 and February 1993 (Ward et al., 1991). The refurbished net, located in the Valley of Ten Thousand Smokes (here referred to as the VTTS subnet), operated until April 1996 and recorded nearly 500 locatable volcano-tectonic earthquakes (Figures 4.2 and 4.3) before a telemetry failure stopped data transmission. The VTTS subnet was re-established in July 1996 and 6 new seismic stations were added in the vicinity of Martin and Mageik volcanoes (here referred to as the MM subnet; Figures 4.1 and 4.3). This augmented local net, which consisted of 11 stations and spanned an area of about 1000 km², recorded almost 1500 locatable earthquakes before another telemetry failure occurred the net in April 1997. The second telemetry failure prompted AVO to replace the old VTTS subnet with 5 new short-period instruments in July 1997. The network includes 9 short-period vertical seismometers with a natural frequency of 1 Hz, and 2 three-component instruments with a natural frequency of 2 Hz. Magnifications range between 1.0×10^6 to 5.0×10^6 at a frequency of 10 Hz. All data are telemetered via FM radio to King Salmon, Alaska, where they are transmitted continuously, frequency-multiplexed via phone lines, to the AVO seismology lab in Fairbanks, Alaska. In Fairbanks, the signals are digitized using a 12 bit analog-to-digital converter at a rate of 100 samples s⁻¹ and recorded in both continuous and event detection modes.

In all, the period July 27, 1995 to December 31, 1997, over 2500 earthquakes were located in the area (Figure 4.2). Earthquakes were located using the program HYPOELLIPSE (Lahr, 1989) and the southern Alaska regional velocity model (Table 1)

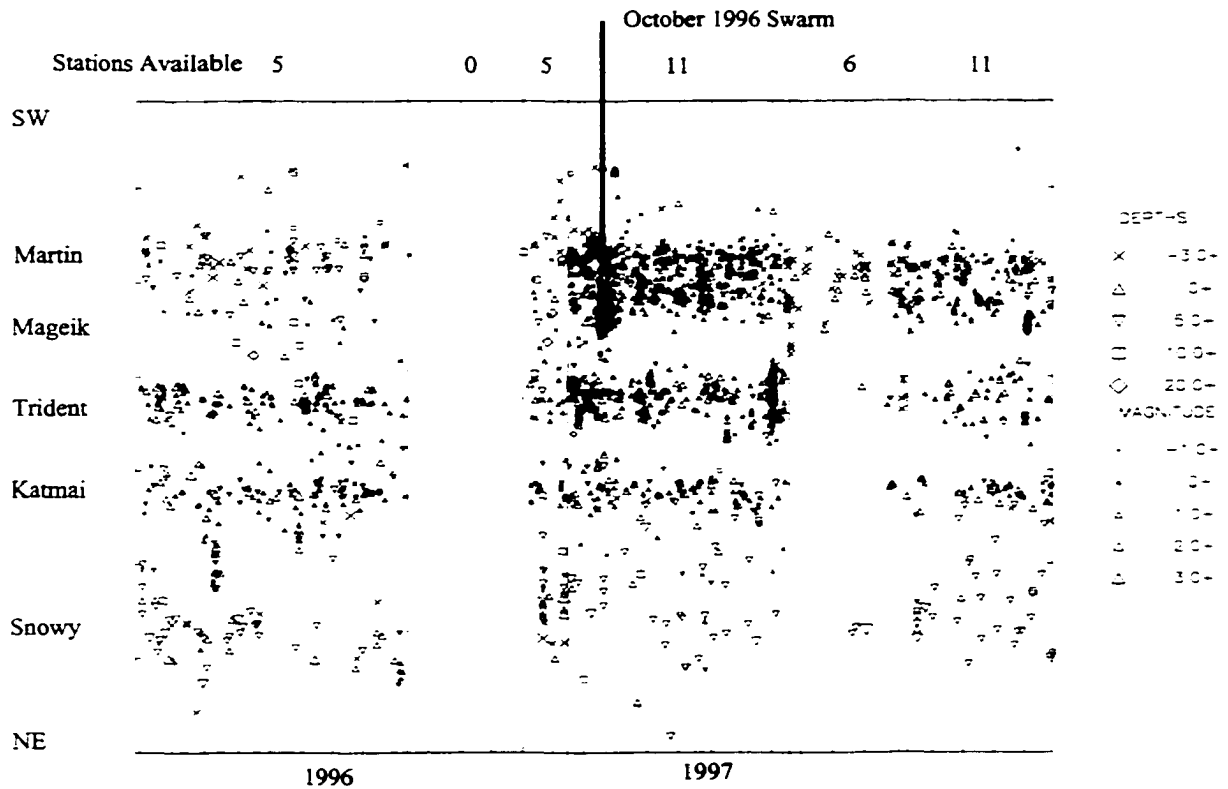


Figure 4.3: Space-time plot along the volcanic axis showing seismicity and station use through time. Numbers of stations available through time are indicated along the top of the diagram. Symbols are as indicated in Figure 4.2.

(Fogleman et al., 1988). Magnitudes (M_L) for these earthquakes were determined using the maximum trace amplitude of several stations. The velocity model was originally used by Ward et al. (1991) to locate seismicity originating between the period September, 1987-December, 1990. The model (Table 4.1) provides locations with formal errors of about 1.5 km in depth at the Trident cluster and about 3.0 km in depth for less well constrained locations near Snowy volcano. These errors are roughly equivalent to errors found for earthquakes originating at other Alaskan volcanoes (Lahr et al., 1994; Jolly et al., 1994). Thus, the model provides adequate locations for kilometer-scale spatial analyses of the seismicity in the Katmai region.

Table 4.1: Velocity model used for locations in the Katmai region (Fogleman et al., 1988). The top of the model begins at 3 km above sea level and depths are referenced to sea level with values below sea level having positive values. A half-space (HS) having velocity of 8.3 km s^{-1} is located at 65 km below sea level.

Layer	Velocity(km/s)	Depth(km)
1	5.3	-3.0
2	5.6	4.0
3	6.2	10.0
4	6.9	15.0
5	7.4	20.0
6	7.7	25.0
7	7.9	33.0
8	8.1	47.0
HS	8.3	65.0

4.4 Seismicity

Upper-crustal seismicity in the Katmai region formed four distinct clusters which were centered beneath Martin-Mageik volcanoes, Trident volcano, 2 km west of Katmai caldera, and about 5 km due west of Snowy volcano. Additional diffuse seismicity occurred along the volcanic axis in an ENE-WSW belt about 20 km in width (Figure 4.2). The earthquakes are volcano tectonic in character and only isolated B-type earthquakes were observed. Earthquake depths were generally shallowest at Trident volcano where seismicity was concentrated above 5 km, and reached greater depths at Martin-Mageik and Snowy volcanoes where earthquakes depths reached to about 10 km. Isolated earthquakes having depths greater than 10 km were occasionally observed. Griggs volcano and Novarupta, site of the paroxysmal 1912 eruption, had little seismic activity beneath them. Magnitudes for earthquakes originating in the region ranged between -0.5 and 4.5 for the period of interest. Anomalous seismicity at 1.0 km above sea level (Figure 4.2, cross-section) results from a location artifact associated with the program HYPOELLIPSE (Lahr, 1989). The artifact is caused by earthquakes that have an insufficient number of arrival times to iterate away from the -1.0 km initial trial depth.

A uniform magnitude detection threshold was determined from the power law of the frequency-magnitude relationship. This detection threshold changed depending on both station availability and distance from the center of the array (Figure 4.3). For the time period July 1995-April 1996 when only 5 seismic stations operated locally, the uniform detection threshold was 1.0 M_L at Martin-Mageik, 0.7 at Trident and 0.7 at Katmai caldera (Table 4.2). After installation of the Martin-Mageik subnet the uniform magnitude detection threshold decreased to about 0.5 M_L at Martin-Mageik and 0.5 at

Table 4.2: Summary of seismicity rates, *b*-values and magnitudes of completeness.

	July 95-April 96	October swarm	Sept. 96-April 97 (excluding swarm)	May 97-Dec 97
	Rate [^] M _{comp} # b*	Rate [^] M _{comp} # b*	Rate [^] M _{comp} # b*	Rate [^] M _{comp} # b*
Martin-Mageik	3 1.0 0.92	500 0.5 1.54	9 0.7 1.56	6 0.7 0.98
Trident	4 0.7 1.03		7 0.5 1.08	2
Katmai Caldera	3 0.7 1.17		3	1
Snowy	1		1	1

[^]-Earthquake rate in events per week.

#-Magnitudes are given in M_L.

*-*b*-value calculated by weighted least squares with average errors ± 0.07 .

Trident (Table 4.2). The addition of the Martin-Mageik subnet generally decreased the uniform detection threshold at Martin-Mageik and Trident volcanoes but not elsewhere.

Rates of seismicity were determined at each of the four clusters to offer baselines for comparison to future activity. Such measurements were complicated, however, by network and station outages and by the addition of new local subnets. At Martin-Mageik, approximately 3 events per week were recorded during the period July 1995-April 1996 when the VTTS subnet operated. The Trident cluster produced 4 events per week during the same period and Katmai caldera cluster had 3 events per week. With the addition of the MM subnet in August-September 1996 the sensitivity and hence the number of locatable earthquakes increased. At Martin-Mageik 9 earthquakes per week were located for the time interval September 1996-April 1997 (excluding events of the October 1996 Mageik swarm), the Trident cluster generated 7 locatable earthquakes per week, and

Katmai caldera recorded 3 earthquakes per week (unchanged from the previous period). Magnitude dependent rates of locatable seismicity appear to follow the Gutenberg-Richter relation for the Trident cluster, which was the only cluster with sufficient seismicity to calculate the rate for increased detection sensitivity. At Martin-Mageik the rate of seismicity appears to follow that expected by the Gutenberg-Richter relation, however the number of small magnitude events is increased significantly relative to the number of large magnitude events. In other words the b -value was much higher for the Martin-Mageik cluster after the end of the October 1996 swarm.

4.5 The October 16-25, 1996 swarm

An intense swarm occurred near Mageik volcano beginning October 16, 1996 with a 1.3 M_L shock (Figure 4.4). This was the most significant swarm recorded since the network was installed, so it is described in detail. The swarm reached its peak rate about 17 hours after the onset (Figure 4.4), and then decayed until background rates were reached 8 days later. The general character of the October 1996 swarm is similar to other swarms originating in volcanic environments. For example, the duration is slightly longer than the average of 3.5 days established by Benoit and McNutt (1996) for 136 non-eruptive earthquake swarms. Further, the swarm's weighted least-squares b -value is 1.54 ± 0.05 (Table 4.2), within the range of published b -values of 0.6 (Endo et al., 1981) to 3.5 (Minakami, 1974), but is anomalous compared to the 1.01 ± 0.06 b -value observed in the same area prior to the swarm (Table 2). The swarm is characterized by a cumulative moment release of about 5.0×10^{20} dyne-cm (Figure 4.4c), roughly equivalent to a single magnitude 3 earthquake.

October 16-25, 1996 Mageik Swarm

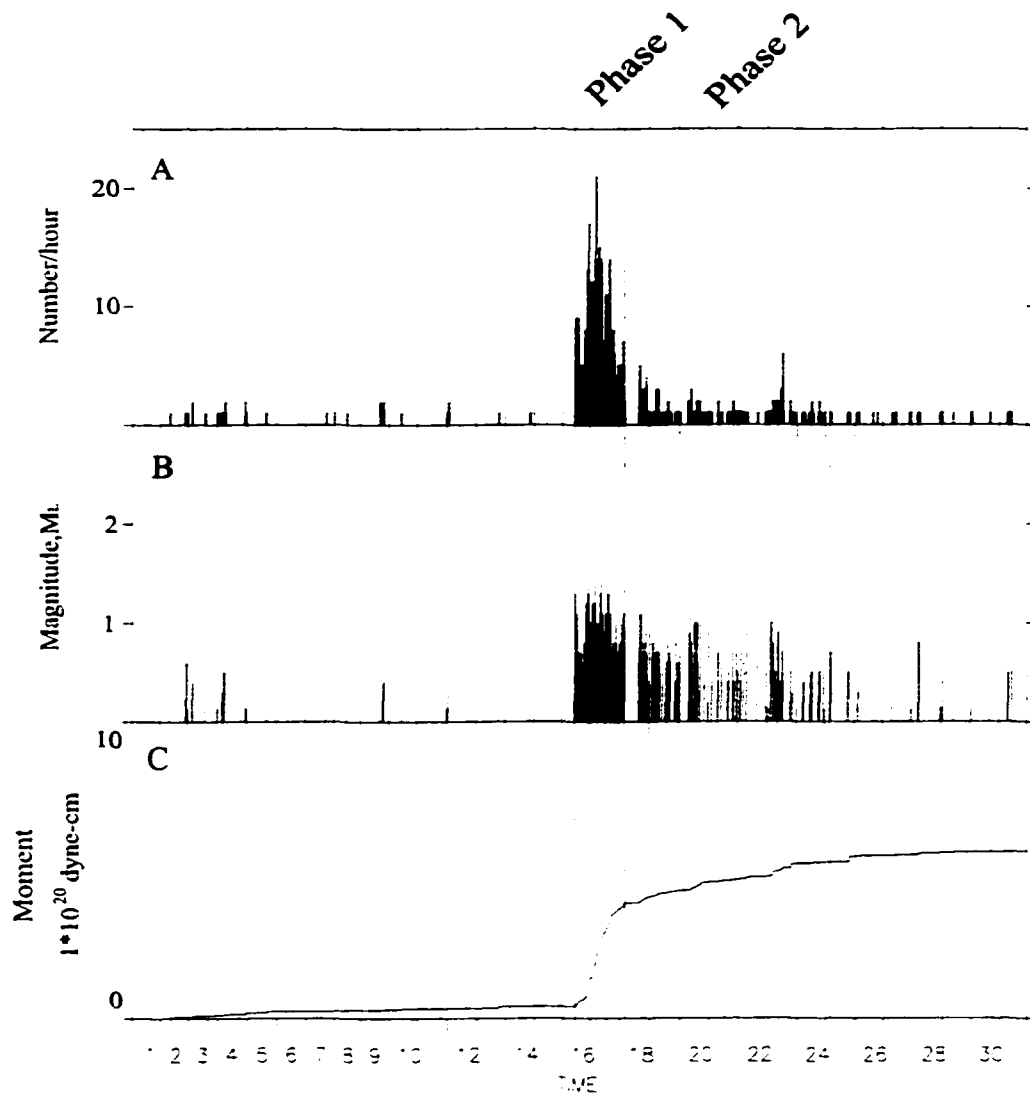


Figure 4.4: Number of events per hour (A), magnitudes (B), and cumulative seismic moment release (C), for the October 16-25, 1996 Mageik swarm. The data span a one month period and moment calculations are determined using parameters derived by Bakun (1984). Vertical lines mark two prominent phases of the swarm. See text for further discussion.

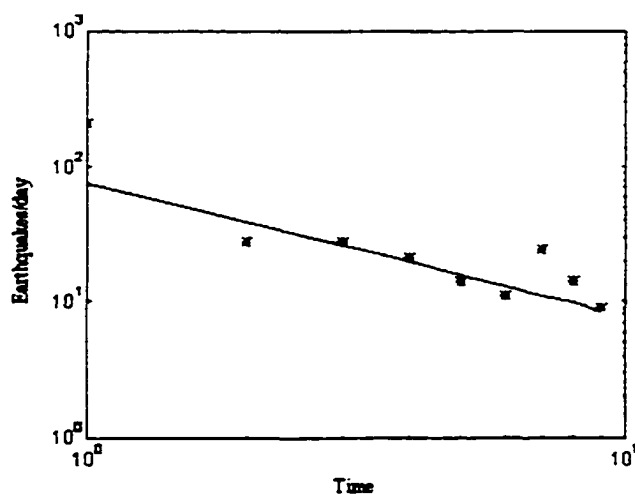


Figure 4.5: Earthquake decay vs. time for October 16-25 Martin-Mageik swarm.

Number of events per day after the peak of seismicity associated with the October 1996 earthquake swarm (stars) and maximum likelihood determination of parameters associated with the decay of the swarm (line). The swarm decays with a p -value of 1.06 ± 0.11 using the modified Omori law. Other parameters of the regression include $c = 0.17 \pm 0.08$ and $k = 88.72 \pm 13.60$. Parameters were derived using the program ASPAR (Reasenber, 1994).

The swarm's p -value or decay rate (Figure 4.5) was estimated using the modified Omori law, expressed by $n(t) = K(t + c)^{-p}$ where $n(t)$ is the number of events per unit time at time t , and K , c and p are parameters which describe the total number of events in the sequence, the rate of activity at the beginning of the sequence, and the decay rate, respectively (Kisslinger and Jones, 1991). The p -value of 1.06 ± 0.11 , which is determined beginning from the peak seismic rate, is similar to p -values determined in southern California (1.11 ± 0.25) for 39 aftershock sequences (Kisslinger and Jones, 1991). This decay rate is used to corroborate an estimate of temperature gradient determined from flow law modeling later in the paper. A 12-hour quiescence was observed beginning about 36 hours after the swarm's onset. The data acquisition systems operated properly throughout the swarm, thus the quiescence is real and separates two phases in the evolution of the swarm (Figure 4.4).

4.6 Spatial variations in the frequency-magnitude distribution

Detailed analysis of variations in the frequency-magnitude distribution in space was conducted using the methods of Wiemer and McNutt (1997) (Figure 4.6). The data selected for this analysis include seismicity from Martin-Mageik, Trident and Katmai caldera (Figure 4.2, dashed box) which were filtered by removing earthquakes smaller than $0.7 M_L$ to reduce the effects of magnitude incompleteness in the data set. The $0.7 M_L$ filter was determined visually from the bulk b -value analyses shown in Table 4.2. About 1100 events remaining in the data set were projected into a cross-sectional plane over which a 0.5 km grid was placed. For each node, a cylindrical volume containing 100 nearest neighbor earthquakes, was selected. The b -value was calculated for this cylindrical volume and subsequent cylindrical volumes in the projected plane. The b -

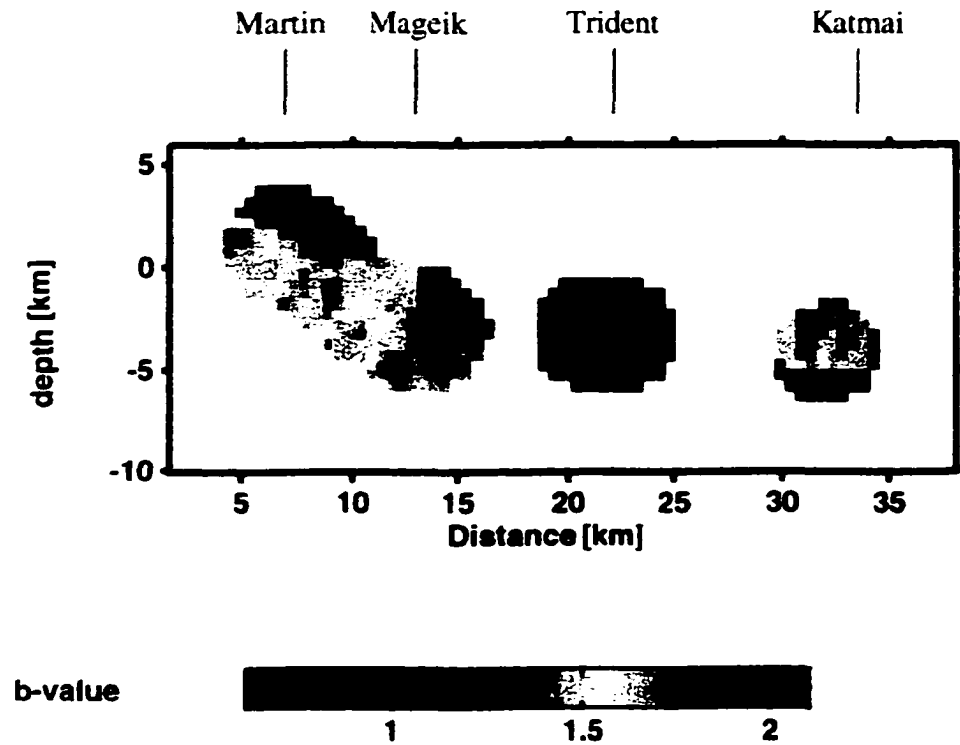


Figure 4.6: Spatial b -values determined within a cross-section shown by dashed line in Figure 4.2. b -values are calculated using a weighted least-squares method described by Wiemer and McNutt (1997).

value was calculated in a weighted least squares sense such that the regression line relies on the number of events in a magnitude class, so that a few larger earthquake do not bias the calculation. Nodes for cylinders smaller than 2.5 km are plotted with the color scale given in Figure 4.6. The processed data (Figure 4.6 and Table 4.2) reveal two high b regions in the vicinity of Martin and Mageik volcanoes ($b > 1.5$), lower relative b -values at Trident ($b = 1.0$) and intermediate b -values at Katmai caldera ($b = 1.2$ to $b > 1.5$). Table 4.2 shows overall or bulk values for each region whereas Figure 4.6 shows higher spatial resolution. High b -values at Martin and Mageik volcanoes occur at about the same depth (3-4 km beneath ground surface) as high b observations at both Spurr and Mt. St. Helens volcanoes (Wiemer and McNutt, 1997) and Mammoth Mountain (Wiemer et al., 1998). No b -value anomaly is associated with the velocity and gravity anomaly observed by Ward et al. (1991) between Trident and Katmai. The high b anomaly beneath Katmai caldera is somewhat deeper (7-8 km beneath ground surface). The anomalous b -values at Martin and Mageik volcanoes probably are associated with the October 1996 swarm and post-swarm seismicity, based on temporal analyses (Table 4.2). Temporal analyses of b -value changes are limited to Martin-Mageik volcanoes, however, because of insufficient data elsewhere for these periods.

4.7 Temporal analyses of pre- and post-swarm seismicity

The character of seismicity at Martin-Mageik changed fundamentally following the October 1996 swarm, with twin observations of increased b -values and shoaling of the maximum depths (Figure 4.7). The b -value was 1.01 at Martin-Mageik between July 27, 1995 and October 16, 1996, and 1.55 for the post-swarm period November 1, 1996 to April 31, 1997 (Table 4.2; Figure 4.8). One possible explanation is that the post-swarm

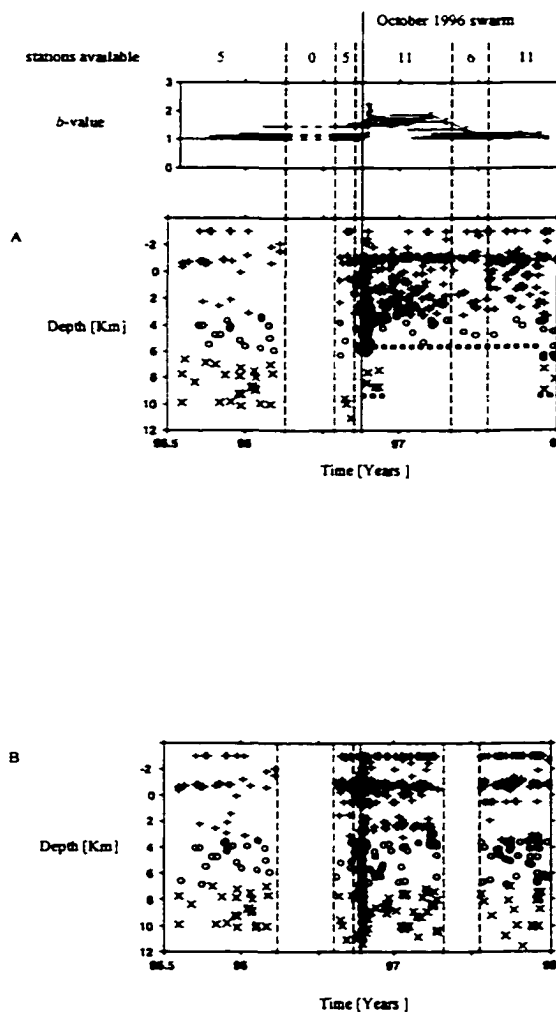


Figure 4.7: The b -value versus time and depth versus time and for pre- and post-swarm seismicity located in the vicinity of Martin and Mageik volcanoes. The moving window b -value calculation contains 100 events per window. Number of stations available for depth calculation are shown above the b -value vs. time plot and period boundaries are marked as vertical dashed lines. Dotted line in plot A refers to the inferred maximum depth of seismicity. B) Relocation of all events using only the VTTS subnet.

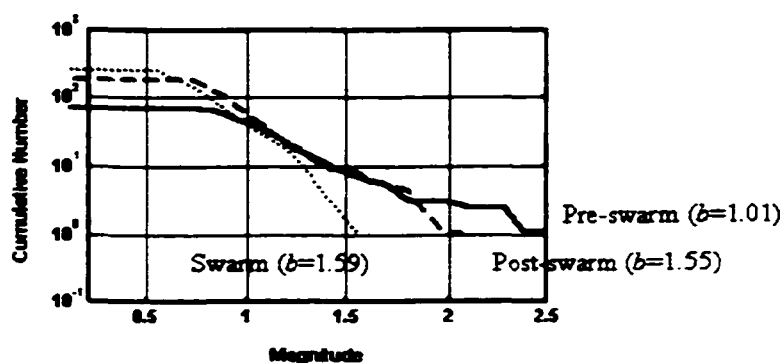


Figure 4.8: Frequency-magnitude distributions for Martin-Mageik area. The distributions are pre-swarm (solid line; July 27, 1997-October 15, 1996), swarm (dotted line; October 16-25, 1996) and post-swarm (dashed line; November 1, 1996-April 30, 1997) periods. Data are selected from the Martin-Mageik cluster with events shallower than 6 km. An Utsu (1992) test for pre-swarm and post-swarm periods show that the b -values are significantly different at a probability greater than 99%.

b-value resulted from excitation of a previously quiescent portion of the crust and thus represented a spatial change in the *b*-value rather than a temporal one. Unfortunately, higher detection levels prior to the October 1996 swarm preclude detailed spatio-temporal analysis of *b*-values such as that shown in Figure 6. It is noted, however, that the seismic cluster above 5 km depth does not change significantly in shape or average location for the two periods. Thus, the *b*-value change probably does not reflect a spatial change within the cluster. For the two periods, using events from identical volumes and with depths less than 5 km, the probability that the *b*-values are different is > 99% as determined by the Utsu (1992) test. The effect of station geometry changes associated with the installation of the new Martin-Mageik seismograph net beginning August 1996 was examined to determine its effect on seismic patterns. At the adjacent Trident cluster, the *b*-value is 1.03 prior to installation of the Martin-Mageik subnet and 1.08 after installation. Errors associated with the weighted least-squares calculations are about ± 0.07 (Table 4.2). Therefore, the two *b*-values are not significantly different. Trident seismicity is only about 8 km away from the Martin-Mageik cluster. If the *b*-value changed at Martin-Mageik as a result of some station change with time, then nearby Trident seismicity should also change. We infer from the lack of *b*-value change at Trident that the scaling of the frequency-magnitude distribution did not change as a result of the addition of the Martin Mageik subnet.

Prior to the October 1996 swarm, seismicity at the Martin-Mageik cluster was generally constrained between the surface and 10 km below sea level (Figure 4.7). Shortly after the October 1996 swarm, the maximum depth of seismicity was observed to decrease to about 5 km below sea level. Again, the change in maximum seismic depths might result from the addition of the Martin-Mageik subnet in September 1996. This hypothesis was tested by relocating the post-swarm seismicity with (Figure 4.7a) and

without the Martin-Mageik subnet (Figure 4.7b), thus locating both data sets with the same subset of seismic stations. After the relocation, post-swarm earthquakes became systematically deeper and occupied the volume which was previously devoid of seismicity. The results suggest that depth change results for the period July, 1995 to September 1996 should be viewed with caution. However, we observe from seismicity located between September 18 and October 16, 1996, when all stations were operational, that seismicity immediately before the swarm was constrained above 5 km (Figure 4.7a). A detailed interpretation of temporal b -value and depth changes is given in the following section.

4.8 Discussion

4.8.1 Interpreting intrusive events

The combined observations of b -values and maximum earthquake depths at Martin-Mageik volcanoes offer an opportunity to evaluate critically the various mechanisms that can affect seismicity in volcanic environments. Both the temporal and spatial scales of the observations are considered and plausible assumptions are subsequently applied to infer their sources. Finally, the physical conditions at depth including the stress, water content, and heat are examined to obtain quantitative estimates of these parameters.

First consider the spatial extent of the b -value anomaly associated with the October 1996 swarm. The seismicity apparently occupies a volume of 15 km³ (Figures 4.2 and 4.3). Lahr et al. (1994) have shown, however, that a point source with typical measurement errors will generate a diffuse cluster of hypocenters. Given the formal

errors (1.5 km in depth) for the locations, and the additional errors inherent with non-uniform phase sets and unknown velocity structure, the swarm's actual source volume may be less than 1 km^3 . Within such a small volume it is possible that a local stress change, a water injection, or a thermal event triggered the seismicity over the 1 week period of the swarm. Alternatively, the b -value change might reflect excitation of a heterogeneous region which was previously quiescent. Any of the above physical processes can easily occur over small ($< 1 \text{ km}^3$) volumes, resulting in the anomalous b -values. These arguments suggest that the physical mechanisms which drive earthquakes for short-lived and small-volume seismic swarms cannot be determined uniquely unless information other than b -value data is available.

The volume within which the swarm-related depth change occurred underlies Martin-Mageik volcanoes and spans a region 6 km along the volcanic axis and 2 km wide. These dimensions are established by the geometry of the seismicity (Figure 4.2), the earthquake location errors, and the separation of the Martin-Mageik volcanic vents. The earthquake depths range from the surface to 10 km below sea level. Thus, the observations span a volume of 150 km^3 , at least one order of magnitude larger than the volume occupied by the October 1996 swarm, and are not dependent on measurement or location errors.

Consider the time scale associated with the change in b -value and in the maximum depth of earthquakes at Martin-Mageik. Because rates of seismicity are low, several months of data are required to calculate a robust b -value. A moving-window b -value calculation (Figure 4.7) suggests that the change occurred within two months of the onset of the October 1996 swarm, reached a peak b -value of >1.5 beginning January 1997, and remained anomalous through April 1997. As stated earlier, depths of seismicity before September 18, 1996 are poorly constrained. During the October 1996

swarm, well constrained depths are above 6 km, with sparse seismicity occurring as deep as 9-10 km. The seismicity between 6 and 10 km persists for about 1-2 months before seismicity returns to the 5 km depth limit. Seismicity remains shallower than 5 km depth during the January-April peak b -value period and increases to ~10 km in November 1997.

Earlier it was established that spatio-temporal b -value changes cannot be attributed to single physical processes without corroborating evidence. If so, then what spatial and temporal scales of observation can be attributed to each candidate physical process? It can be argued that certain physical processes associated with the observed changes may be excluded if the changes occur over too large a volume or too short a period to be plausible. As an example, material heterogeneity can be excluded because it would require unrealistically extensive brittle deformation to occur over the short period observed. Likewise, thermal conduction is difficult to invoke because estimates of cooling of intrusions (e.g., Hill, 1992) show that thermal gradient changes in the upper crust occur over thousands of years, not the observed several months.

Increased water content is known to reduce the strength of all rock types, causing increased b -values (Wyss, 1973) or plastic creep in rock (Sibson, 1982; Hill, 1992). However, water diffusion cannot account for the increase in the maximum depth of seismicity at Martin-Mageik volcanoes, because the diffusion rates are slow (Kronenberg et al., 1986) and in the wrong polarity to account for the depth change observations.

A stress increase is a potential mechanism. Pressurization of the system will tend to push seismicity from plastic to brittle deformation at depth. However, Scholz (1968) determined that b -values are lowered with the application of higher shear stress, opposite of the observation at Martin-Mageik. A simple stress increase is excluded as a mechanism responsible for the observations.

These analyses suggest that a single candidate process is not responsible for the twin observations at Martin-Mageik. It may be that a more complicated model is needed to explain the observations. Of several combinations of processes, an actively degassing intrusive model is considered most likely. If the intrusion contains sufficient volatiles, their propagation into surrounding country rock will act to reduce the effective stress and increase the b -value. At the same time, the intrusion increases the applied stress, moving rocks from plastic to brittle behavior. The intrusive degassing mechanism also agrees with the timescale of observations. Stresses propagate through the crust rapidly and can dissipate rapidly, accounting for the 1-2 month time scale for reducing the depth of seismicity from 10 to 5 km. Degassing of magmatic fluids is a much slower process, as reflected by the seven month period required to reduce the b -value to pre-swarm levels.

Some additional evidence of an intrusive degassing event is available at Martin-Mageik volcanoes. Surface measurements were taken at Mageik's crater lake in July 1995, and again in July 1997. The measurements showed an increase in the lake water temperature of about 10°C (R. Symonds, personal communication, 1997). These observations, made 15 months before and 10 months after the b -value change in October 1996 (Figure 4.7), give circumstantial support to the hypothesis of an intrusion which temporarily increased the stress causing increased seismicity at depth while at the same time increased fluids caused the b -value to increase beneath Martin-Mageik volcanoes.

The 1989 Mammoth Mountain swarm exhibited similar behavior to the observations we describe at Martin-Mageik. The Mammoth Mountain post swarm seismicity was associated with an increase in the maximum depth of volcano-tectonic seismicity from 8 to 11 km (Hill, 1996) and an increase in the b -value from 0.8 to 1.5 (Wiemer et al., 1998), in agreement with our observations. If the Mammoth Mountain swarm resulted from a simple dike intrusion, as suggested by Langbein et al. (1993), one

would expect increased pressurization, which in turn induces deeper seismicity and lower b -values (Scholz, 1968). If, however, the Mammoth Mountain swarm resulted from intrusion and exsolution of a fluid phase as suggested by Hill (1996) and Wiemer et al. (1998), then both the b -value and the maximum earthquake depth would increase only if water-related b -value changes dominate stress-related b -value changes. Evidence for fluid exsolution at Mammoth Mountain includes CO₂ emissions (Farrar et al., 1995) and long-period earthquakes (Hill, 1996).

Magma degassing may be critical in the interpretation of b -values associated with intrusive events. For example, the intrusion at Mammoth Mountain is associated with a high b -value and extensive CO₂ gas emission, while the intrusion prior to the May 18, 1980 Mount St. Helens eruption had a low b -value of 0.6 (Endo et al., 1981) and low SO₂ levels (Casadevall et al., 1981). Initial eruptive products at Mt. St. Helens were not degassed (Eichelberger et al., 1986) possibly because ascent rates were very rapid, and diffusion through the magma and into the surrounding country rock was inefficient (Eichelberger, 1995). If so, then little fluid was available from the magma to reduce the effective stress and increase the b -value in the surrounding rocks.

In both Mount St. Helens and Mammoth Mountain, surface deformation was observed and seismicity propagated to depths where little prior seismicity had been observed (Endo, 1981; Hill, 1996). Elsewhere, Fedotov et al. (1992) observed changes in the mean depth of seismicity which correlated with surface deformation near Klyuchevskoy volcano in Kamchatka. However, no b -value changes were reported. The available evidence suggests that pressurizing intrusive events may be accompanied by increased maximum seismic depths and high b -values in the presence of magma degassing, and low b -values otherwise. At Martin-Mageik, the November-December

1997 increase in the maximum depth of seismicity is not accompanied by an increase in the b -value. This observation is interpreted as a pressurizing event without degassing.

4.8.2 Flow law models

If the October 1996 swarm is associated with a stress increase, then the process can be modeled by the flow law to determine the magnitude of the strain rate change. This is done with shear strength models previously discussed by Sibson (1982), Scholz (1988), and Hill (1992). In their formulations the static frictional strength of the brittle layer is given by

$$\tau = \mu S_n \quad 4.1$$

where τ has units MPa, μ is the coefficient of friction (dimensionless), and S_n is the brittle effective compressional stress (MPa) normal to the local fracture surface. Under conditions of classical Andersonian faulting with $\mu = 0.75$, hydrostatic pore pressure, and pressures less than 500 MPa (Byrlee, 1978; Sibson, 1982), the strength of rock should be proportional to τ (MPa)=10 z for strike-slip faulting, where z =depth in km. The strength for normal, strike-slip and thrust faulting follows from the ratio 1:1.6:4 (Sibson, 1982).

The flow law is given by

$$\dot{\epsilon} = A\sigma^n \exp(-H^*/RT) \quad 4.2$$

where σ is the differential stress $\sigma = \tau = (\sigma_1 - \sigma_3)/2$ or the shear strength. Solving for the shear strength gives

$$\tau = (\dot{\epsilon}/A)^{1/n} \exp(H^*/nRT) \quad 4.3$$

(Kirby and Kronenberg, 1987) where $\dot{\epsilon}$ is the strain rate, H^* is the activation energy, R is the universal gas constant, T is absolute temperature and A and n are constants.

Table 3: Steady-state parameters (A , n and H^*) used in flow-law models. Parameters evaluated include the strain-rate increase ($\Delta\dot{\epsilon}$), temperature gradient (dT/dz), and temperature increase (dT), required to induce plastic flow using flow law of the form $\tau = (\dot{\epsilon}/A)^{1/n} \exp(H^*/nRT)$ (Kirby and Kronenberg, 1987).

Rock type	$A(\text{MPa}^{-n} \text{s}^{-1})$	n	$H^*(\text{kJ mol}^{-1})$	$\Delta\dot{\epsilon}(\text{s}^{-1})\dagger$	dT/dz ($^{\circ}\text{C km}^{-1}$)
<u>felsic</u>					
granite 'wet' #	1.9×10^{-3}	1.5	137	10^5	20
granite 'dry' #	2.6×10^{-9}	3.4	139	10^5	30
<u>intermediate</u>					
Diorite 'wet' #	3.8×10^{-2}	2.4	216	10^8	35
<u>mafic</u>					
Diabase*	2.2×10^{-4}	3.4	260	10^8	50

Hanson and Carter, 1982.

* Shelton and Tullis, 1981.

† Assume upper strain rate of 10^{-16} s^{-1} .

The flow law characteristics of 'wet' and 'dry' Westerly granite, 'wet' diorite (Hanson and Carter, 1982) and diabase (Shelton and Tullis, 1981) (Table 4.3) were applied to determine the effects of strain rate and temperature (equations 4.2 and 4.3) on the depth of the brittle-ductile transition. First the upper limit of the thermal gradient (dT/dz ; Table 3) at Martin-Mageik volcanoes is obtained by determining the strength of the rock at given thermal gradients with the flow law parameters for both felsic and mafic rocks, and assuming that strain rates do not exceed the highest values historically observed in geologic and volcanic environments worldwide (10^{-11} s^{-1} ; Hill, 1992). Then, the 10 km seismicity depth yields a thermal gradient less than $30^{\circ}\text{C km}^{-1}$ if rocks are felsic and $70^{\circ}\text{C km}^{-1}$ if rocks are mafic. Alternatively, if strain rates are near the geologically observable limit of detection (10^{-16} s^{-1}), then the thermal gradient is between $15\text{-}25^{\circ}\text{C km}^{-1}$ if the rocks are felsic and $35\text{-}50^{\circ}\text{C km}^{-1}$ if rocks are intermediate to mafic.

Martin-Mageik deposits are andesitic to dacitic while nearby Novarupta volcano deposits are rhyolitic to andesitic. Thus, thermal gradients probably have lower to intermediate values of 20–40 °C km⁻¹ even if strain rates are relatively high.

The strain rate increase ($\Delta\dot{\epsilon}$) required to increase the depth is strongly dependent on rock type, but not on thermal gradient (dT/dz) or initial strain rate ($\dot{\epsilon}$) (Table 4.3). If the rocks near Martin-Mageik are felsic, then a 5 order-of-magnitude increase in the strain rate is required to change the maximum depth of seismicity from 5 to 10 km (Figure 4.9). If rocks are intermediate to mafic, then an 8 order-of-magnitude increase is required (Table 4.3). No surface deformation data is available to determine if these values are reasonable.

The flow law provides useful constraints; however, there are many uncertainties associated with such analyses. These include experimental uncertainties of A , n and H^* (Chen and Molnar, 1983) and uncertainties associated with extrapolation of laboratory strain rate measurements of 10^{-4} to 10^{-8} s⁻¹ (Hanson and Carter, 1982) to the geologically observed strain rates of 10^{-11} and 10^{-16} s⁻¹ (Hill, 1992). In addition, temperature gradients at Martin-Mageik are not known, and variations in temperature can cause large changes in the exponential term of the flow law equation. This latter concern may be addressed by evaluating the 1.06 ± 0.11 p -value observed for the October 1996 swarm (Figure 4.5). Mogi (1967) and Kisslinger and Jones (1991) demonstrated general relationships between heat flow and p -values in studies in Japan and southern California, respectively. In California the average p -value is 1.11 ± 0.25 (Kisslinger and Jones, 1991, their Figure 6), a value which is in agreement with our computation and which suggests heat flow of about 120 mWm⁻² for Martin-Mageik volcanoes. Such heat flows also correspond to our modeled temperature gradients of 20–40 °C km⁻¹. Higher temperature gradients, such as are observed at the Phlegrean fields (120 °C km⁻¹; De Vivo et al. 1988), are unreasonable

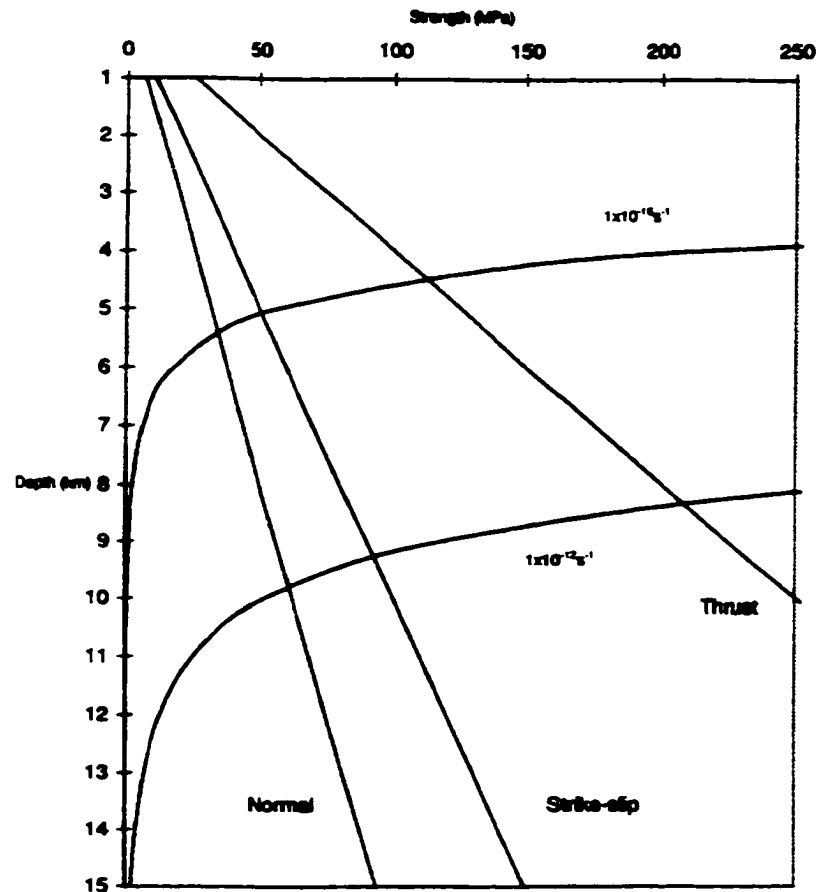


Figure 4.9: Rock shear strength (MPa) vs depth (km) for brittle and plastic flow. Brittle rock strength profiles (straight lines) are for normal, strike-slip, and thrust faulting as determined by (Byrlee, 1978) and (Sibson, 1983). Flow law shear strength profiles (curved lines) as developed by Kirby and Kronenberg (1987) show shear strength for low strain rate and high strain rate cases. Intersection of curved and straight lines show the depth below which plastic flow dominated for the given brittle strength profile. Temperature-depth gradient is $20^{\circ}\text{Ckm}^{-1}$.

for Martin-Mageik volcanoes because they would result in much shallower maximum earthquake depths and higher p -values.

4.9 Conclusions

Results at Martin-Mageik, Mammoth Mountain, and Mt. St. Helens show that the maximum depths of seismicity in conjunction with b -values can be used to interpret the physical processes which operate in volcanic environments. It is proposed that swarms which have low b -values and increased depths of seismicity are associated with degassed intrusions while swarms with high b -values and increased depths of seismicity represent actively degassing intrusions. Simultaneous changes in these parameters provide a method of isolating physical processes which occur at active volcanoes. These new results at Martin-Mageik suggest that an intrusive event occurred, with magmatic degassing. This in turn triggered the anomalous seismicity and surface temperatures. Further case studies are needed to elucidate these patterns. The outcome of these studies will determine if volcanic hazard assessment can be improved based on a coupled analyses of maximum depths of seismicity and b -values.

4.10 References

Abe, K., Seismicity of the caldera-making eruption of Mount Katmai, Alaska, in 1912, Bull. Seismol. Soc. Amer., 82, 175-191, 1992.

Anderson, R.N., Hasegawa, A., Umino, N., and Takagi, A., Phase changes and the frequency-magnitude distribution in the upper plane of the deep seismic zone beneath Tohoku, Japan, J. Geophys. Res., 85, 1389-1398, 1980.

Bakun, W.H., Seismic moments, local magnitudes, and coda duration magnitudes for earthquakes in central California, *Bull. Seis. Soc. Amer.*, 74, 439-458, 1984.

Benoit, J.P. and McNutt, S.R., Global volcanic earthquake swarm database 1979-1989, *U.S. Geol. Surv. Open File Report.*, 96-69, 333 p., 1996.

Byrlee, J. D., Friction of rocks, *Pure Appl. Geophys.*, 116, 615-626, 1978.

Casadevall, T.J., Johnson, D.A., Harris, D.M., Rose, W.I., Malinconico, L.L., Stoiber, R.E., BornHorst, T.J., Williams, S.N., Woodruff, L. and Thompson, J.M., SO₂ emission rates at Mt. St. Helens from March 29 through December, 1980, in P.W. Lipman and D.R. Mullineaux eds. *The 1980 eruptions off Mount St. Helens, Washington*, U.S. Geol. Surv, Professional Paper 1250, 193-200, 1981.

Chen, W.P, and Molnar P., Focal depths of intracontinental and intraplate earthquakes and their implications for the thermal and mechanical properties of the lithosphere, *J. Geophys. Res.*, 88, 4183-44124, 1983.

De Vivo, B., Belkin, H.E., Barbieri, M., Chelini, W., Lattanzi, P., Lima, A., and Tolomeo, L., The Campi Phlegrei (Italy) geothermal system: a fluid inclusion study of the Mofete and San Vito fields, *J. Volcanol. and Geotherm. Res.*, 36, 303-326, 1988.

Eichelberger, J.C., Carrigan, C.R., Westrich, H.R. and Price, R.H., Non-explosive silicic volcanism, *Nature*, 323, 589-602, 1986.

Eichelberger, J.C., *Silicic Volcanism: Ascent of viscous magmas from crustal reservoirs*, *Annu. Rev. Earth Planet. Sci.*, 23, 41-63, 1995.

Endo, E.T., Malone, S.D., Noson, L.L., and Weaver, C.S., Locations, magnitudes, and statistics of the March 20-May 18 earthquake sequence, in P.W. Lipman and D.R. Mullineaux, eds. The 1980 eruptions off Mount St. Helens, Washington, U.S. Geol. Surv., Professional Paper 1250, 93-107, 1981.

Farrar, C.D., Sorey, M.L., Evans, W.C., Howle, J.F., Kerr, B.D., Kennedy, B.M., King, C.Y., and Southon, J.R., Forest-killing diffuse CO₂ emissions at Mammoth mountain as a sign of magmatic unrest, *Nature*, 376, 675-687, 1995.

Fedotov, S.A., Gorelchik, V.I., and Zharinov, N.A., Deformation, earthquakes and mechanism of activity of Klyuchevskoy volcano, *Volcanic Seismology, IAVCEI Proceedings in Volcanology 3*, P. Gasparini, R. Scarpa, K. Aki, eds., Springer-Verlag, 20-44, 1992.

Fierstein, J. and Hildreth, W., The plinian eruptions of 1912 at Novarupta, Katmai National Park, Alaska, *Bull. Volcanology*, 54, 646-684, 1982.

Fogleman, K.A., Stephens, C.D., and Lahr J.C., Catalog of earthquakes for southern Alaska for 1985, U.S. Geol. Surv. Open File Report., 88-312, 112 p., 1988.

Gutenberg, B. and Richter C.F., Frequency of earthquakes in California, *Bull. Seis. Soc. Amer.*, 34, 185-188, 1954.

Hanson, F.D. and Carter, N.L., Creep of selected crustal rocks at 1000 MPa, *EOS Trans. American Geophysical Union*, 63, 437, 1982.

Hildreth, W., New perspectives on the eruption of 1912 in the Valley of Ten Thousand Smokes, Katmai National Park, Alaska, *Bull. Volcanology*, 49, 680-693, 1987.

Hill, D.P., Temperatures at the base of the seismogenic crust beneath Long Valley caldera, California, and the Phlegrean fields, Italy, *Volcanic Seismology, IAVCEI Proceedings in Volcanology 3*, P. Gasparini, R. Scarpa, K. Aki, eds., Springer-Verlag, 432-461, 1992.

Hill, D.P., Earthquakes and carbon dioxide beneath Mammoth mountain, California, *Seis. Res. Lett.*, 67, 8-15, 1996.

Jolly, A.D., Page, R.A. and Power, J.A., Seismicity and stress in the vicinity of Mount Spurr volcano; South central Alaska, *J. Geophys. Res.*, 99, 15305-15318, 1994.

Kienle, J., Gravity traverses in the Valley of Ten Thousand Smokes, Katmai National Monument, Alaska, *J. Geophys. Res.*, 75, 6641-6649, 1970.

Kirby, S.H. and Kronenberg, A.K., Rheology of the lithosphere: selected topics, *Rev. Geophys.*, 25, 1219-1244, 1987.

Kisslinger, C. and Jones, L.M., Properties of aftershock sequences in southern California, *J. Geophys. Res.*, 96, 11947-11958, 1991.

Kleinman, J.W., Iwatsubo, E.Y., Power, J.A. and Endo, E.T., Geodetic studies in the Novarupta area, Katmai National Park, Alaska, 1990 to 1995, in J.A. Dumoulin and J.E. Gray eds., *Geologic Studies in Alaska by the U.S. Geological Survey, 1995*, U.S. Geol. Surv. Professional Paper 1574, p. 83-92, 1997.

Kronenberg, A.K., Kirby, S.H., Aines, R.D. and Rossman, G.R., Solubility and diffusional uptake of hydrogen in quartz at high water pressure: Implications for hydrolytic weakening, *J. Geophys. Res.*, 91, 12723-12744, 1986.

Kubota, S. and Berg, E., Evidence for magma in the Katmai volcanic range, *Bull. Volcanologique*, 31, 175-214, 1967.

Langbein, J., Hill, D.P., Parker, T.N. and Wilkinson, S.K., An episode of reinflation of the Long Valley caldera, eastern California: 1989-1991, *J. Geophys. Res.*, 98, 15851-15870, 1993.

Lahr, J.C., HYPOELLIPSE/Version 2.0: A computer program for determining local earthquake hypocentral parameters, magnitude, and first motion pattern: U.S Geol. Surv., Open-File Report 89-116, 89p., 1989.

Lahr, J.C., Chouet, B.A., Stephens, C.D., Power, J.A. and Page, R.A., Earthquake location and error analysis procedures for a volcanic sequence: Application to the 1989-1990 eruptions at Redoubt volcano, Alaska, *J. Volcanol. Geotherm. Res.*, 62, 137-153, 1994.

Lu, Z., Fatland, R., Wyss, M., Li, S., Eichelberger, J., Dean, K., Freymueller, J., Deformation of New Trident volcano measured by ERS-1 SAR interferometry, Katmai National Park, Alaska, *Geophys. Res. Lett.*, 24, 695-698, 1997.

Matumoto, T. and Ward, P.L., Microearthquake study of Mount Katmai and vicinity, Alaska, *J. Geophys. Res.*, 72, 2557-2568, 1967.

Matumoto, T., Seismic body waves observed in the vicinity of Mount Katmai, Alaska, and evidence for the existence of molten chambers, *Geol. Soc. Amer. Bull.*, 82, 2905-2920, 1971.

Minakami, T., **Seismology of volcanoes in Japan**, in Civetta et al eds., **Physical volcanology. Developments in solid earth geophysics**, Elsevier, Amsterdam, Holland, 6, 313-333, 1974.

Mogi, K., **Magnitude-frequency relation for elastic shocks accompanying fractures of various materials and some related problems in earthquakes (2nd Paper)**, **Bull. Earthquake Res. Inst.**, 40, 831-853, 1962.

Mogi, K., **Earthquakes and fractures**, **Tectonophysics**, 5, 35-55, 1967.

Pacheco, J.F., Scholz, C.H. and Sykes, L.R., **Changes in the frequency-size relationship from small to large earthquakes**, **Nature**, 355, 71-73, 1992.

Power, J.A., Jolly, A.D., Page, R.A. and McNutt, S.R., **Seismicity and forecasting of the 1992 eruptions of Crater Peak vent, Mount Spurr volcano Alaska: An overview**, in T.E.C. Keith ed., **The 1992 eruptions of Crater peak vent, Mount Spurr volcano, Alaska**, U.S. Geol. Surv. Bull. 2139, 149-159, 1995.

Power, J.A., Wyss, M., Latchman, J.L., **Spatial variations in the frequency-magnitude distribution of earthquakes at Soufriere Hills volcano, Montserrat, West Indies**, **Geophys. Res. Lett.**, 25, 3653-3656, 1998.

Reasenber, P.A., **Computer programs ASPAR, GSAS, ENAS and APROB for the statistical modeling of aftershock sequences and estimation of aftershock hazard**, U.S Geol. Surv., Open-File Report, 94-221, 1994.

Scholz, C.H., **The frequency-magnitude relation of microfracturing in rock and its relation to earthquakes**, **Bull. Seis. Soc. Amer.**, 58, 399-415, 1968.

Scholz, C.H., **Scaling laws for large earthquakes: Consequences for physical models**, Bull. Seis. Soc. Amer., 72, 1-14, 1982.

Scholz, C.H., **The brittle-plastic transition and the depth of seismic faulting**, Geol. Rundsch, 77, 319-328, 1988.

Sibson, R.H., **Fault zone models, heat flow, and the depth distribution of earthquakes in the continental crust of the United States**, Bull. Seis. Soc. Amer., 72, 151-163, 1982.

Shelton, G and Tullis, J.A., **Experimental flow laws for crustal rocks**, EOS Trans. Amer. Geophys. U., 62, 496, 1981.

Stephens, C.D., Lahr, J.C. and Page, R.A., **Seismicity along southern coastal Alaska, October 1981 - September 1982**, The United States Geological Survey in Alaska, K.M Reed and S. Bartsch-Winkler eds., U.S. Geol. Surv. Circ. 939, 78-82, 1984.

Utsu, T., **On seismicity**, in : Report of Cooperative Research Institute of the Statistical Mathematics 34, Mathematical Seismology VII, Annals of the Institute of Statistical Mathematics, Tokyo, 139-157, 1992.

Ward, P.A., Pitt, A.M. and Endo, E., **Seismic evidence for magma in the vicinity of Mt. Katmai, Alaska**, Geophys. Res. Lett., 18, 1537-1540, 1991.

Warren, N.W., and Latham, G.V., **An experimental study of thermally induced microfracturing and its relation to volcanic seismicity**, J. Geophys. Res., 75, 4455-4464, 1970.

Wiemer, S. and Benoit, J., 1996, **Mapping the *b*-value anomaly at 100 km depth in the Alaskan and New Zealand subduction zones**, Geophys Res. Lett., 23, 1557-1560, 1996.

Wiemer, S. and McNutt, S.R., Variations in the frequency magnitude distribution with depth in two volcanic areas: Mount St. Helens, Washington, and Mt. Spurr, Alaska, *Geophys. Res. Lett.*, 24, 189-192, 1997.

Wiemer, S., McNutt, S.R. and Wyss, M., Temporal and three-dimensional spatial analyses of the frequency-magnitude distribution near Long Valley caldera, *Geophys. J. Intl.*, 134, 409-421, 1998.

Wyss, M., Towards a physical understanding of the earthquake frequency distribution, *Geophys. Roy. Astr. Soc.*, 31, 341-359, 1973.

Wyss, M., Shimazaki, K. and Wiemer, S., Mapping active magma chambers by b values beneath the off-Ito volcano, Japan, *J. Geophys. Res.*, 102, 20413-20422, 1997.

Zuniga, F.R. and, Wyss, M., Inadvertent changes in magnitude reported in earthquake catalogs: Their evaluation through b -value estimates, *Bull. Seis. Soc. Amer.*, 85, 1858-1866, 1995.

Chapter 5: Spatial variations in b -values and earthquake relocations

5.0 Abstract

This chapter presents a new and improved version of the spatial b -value analysis. Earthquakes recorded for the period July 26, 1995 to November 30, 1999 were re-located using a new three-dimensional velocity model to determine the effect of improved earthquake locations on b -value spatial maps. The three-dimensional velocity model was derived by non-linear inversion of over 8000 first P-arrival times. These new locations and b -value spatial maps are compared to baseline locations and b -value spatial maps derived from the standard Alaska Volcano Observatory (AVO) one-dimensional velocity model. For both standard and revised velocity models, the seismicity forms distinct seismic clusters beneath Martin, Mageik, Trident and Katmai caldera. Earthquake locations are similar for both models at Mageik, Trident and Katmai caldera, but are noted to shift for seismicity beneath Martin volcano. For this cluster, earthquakes ranged between -3 to 4 km depth for the standard model locations and between -1 to 6 km depth for the relocation. The standard model locations yield high b -values at Martin (0.8 - 1.8) and Mageik (1.2 - 2.2) volcanoes, lower b -values at Trident volcano (0.6 - 1.2) and moderate b -values at Katmai caldera (0.7 - 1.2). After the relocation, the b -value distribution at Mageik (1.2 - 2.2), Trident (0.6 - 1.2) and Katmai caldera (1.2 - 1.4) are similar to their standard model b -value ranges. The b -value distribution at Martin volcano, however is significantly changed. The standard model yielded low b -values (0.8 - 1.2) near the surface -3 to 0 km depth and higher b -values (1.2 - 1.8) at greater depths

with the standard model. After relocation, the high and low b -value zones are eliminated and the b -value ranges between (1.0-1.6).

5.1 Introduction

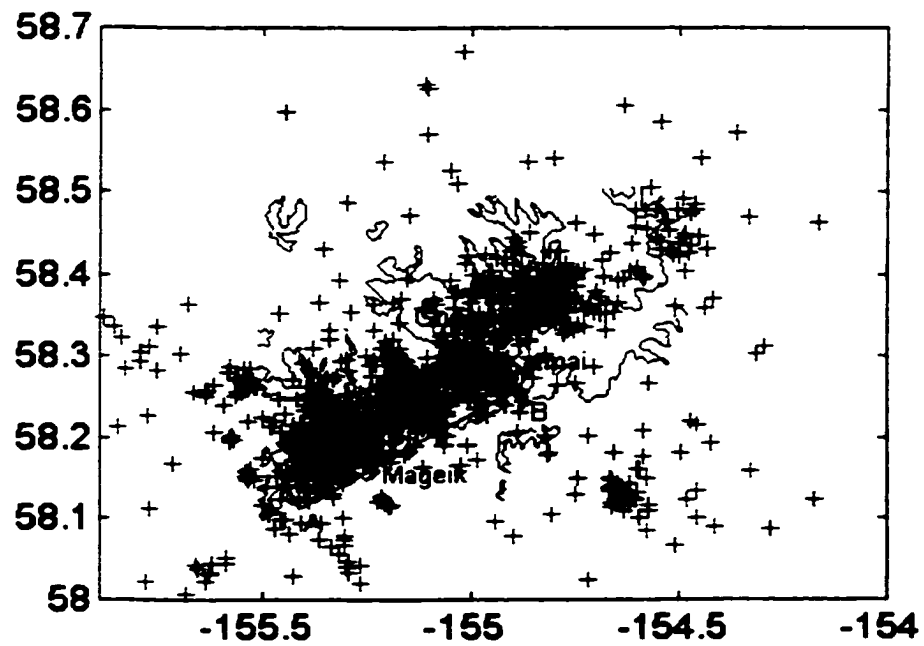
The b -value analysis in Chapter 4 was completed using data collected July 26, 1995-December, 31 1997. After this period, the Alaska Volcano Observatory added 7 seismic stations to the Katmai network (Chapter 1). The new network configuration yielded 1800 additional earthquakes for the period January 1, 1998-November 30, 1999. Earthquakes from the two periods provided the basis for a new P-wave velocity model and revised earthquake locations (Chapter 2). The revised earthquake locations, in turn, offer an opportunity to examine the effect of improved velocity models on the b -value spatial mapping techniques conducted in Chapter 4.

Three aspects of the b -value study of Chapter 4 merit review: 1) an examination of the spatial b -value for earthquake data collected for the period July 26, 1995-November 30, 1999, using the standard AVO velocity model, 2) a comparison of spatial b -value variations with both the standard AVO velocity model and the b -values derived from the new three-dimensional model (Chapters 2 and 3) and 3) an examination of the effect of earthquake relocations on temporal changes observed beneath Martin and Mageik volcanoes. These aspects of the seismicity are examined in order in Sections 5.2-5.5.

5.2 Frequency-magnitude distribution using 1-D velocity model

Earthquake locations depend on the velocity model used. Thus, as a first step, the spatial frequency-magnitude results of Chapter 4 are re-examined by combining data from July 26, 1995-December 31, 1997 with new data from January 1, 1998-November 30, 1999. The earthquakes are located using the standard AVO velocity model (Table 4.1) and the combined data are presented in Figure 5.1. Comparison of the combined datasets with results from the earlier data locations (Figure 4.2) show that persistent features of the seismicity remain: namely 4 clusters of seismicity centered at Martin-Mageik, Trident, Katmai caldera and Snowy volcano generally located above 10 km depth. Details of the seismicity also persist. For example, the very shallow seismicity (–3 km to 5 km depth) beneath Martin Volcano for the earlier dataset (Figure 4.2) is also present in the combined dataset (Figure 5.1b). As a second step, a new b -value map and cross-section were produced using the methods outlined in Section 4.6. First, the dataset was filtered by removing earthquakes smaller than $0.7 M_L$. This reduced the effects of magnitude incompleteness in the data set and left about 2600 events for analysis. Remaining events were projected into both a map and cross-section and a 0.5 km by 0.5 km grid was overlain on both projections. For each grid-node, a variable cylindrical volume containing 100 nearest neighbor earthquakes was selected. The b -value was calculated for each cylindrical volume in the projected plane. The b -value was calculated in a weighted least squares sense such that the regression line relies on the number of events in a magnitude class. This weighting scheme ensured that a few larger

a)



b)

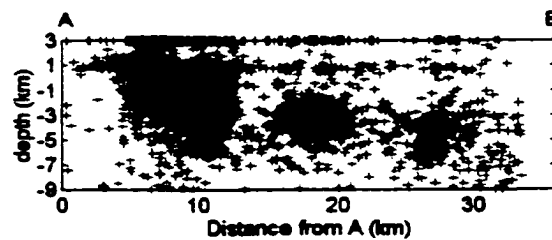


Figure 5.1: Map (a) and cross-section (b) of seismicity in the Katmai region. Seismicity is from the period July 20, 1995 to November 31, 1999.

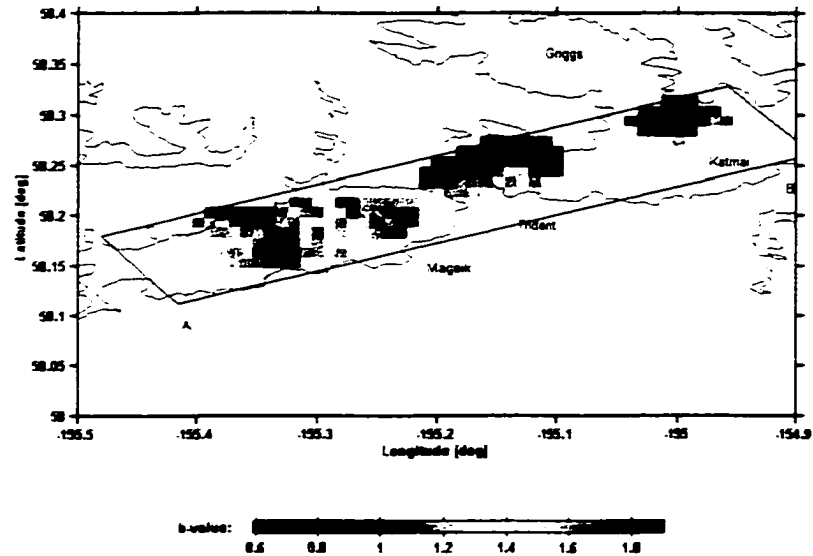
earthquakes do not bias the b -value calculation. Nodes for cylinders smaller than 2.5 km are plotted with the color scale given in Figure 5.2.

The cross-section of Figure 5.2 is substantially the same as the cross-section of Figure 4.6 shown in Chapter 4 despite the addition of about 30% more data. The addition of these new data show that the prior b -value results are robust, and do not represent under sampled spatial distributions which change markedly with new data. Instead, the anomalies are judged to be temporally persistent and provide a baseline for comparison to b -value spatial maps using an improved velocity model.

5.3 Frequency magnitude distribution with a new three-dimensional velocity model

The new b -value map with all data (Figure 5.2) is next compared to the same dataset located with the new three-dimensional velocity model (Chapter 2). All earthquakes are relocated using the final three-dimensional model of the P-wave velocity inversion (Figure 2.4) and are re-plotted here for convenience (Figure 5.3). The relocation utilized only P-wave arrival times because an S-velocity model was not developed in Chapter 2 and the computer code for S-wave derived locations is not available. For the relocation of each earthquake, 5 P-wave arrival times, and a gap less than 300 degrees was required, a criterion established as a compromise between data sufficiency and earthquake location quality, which reduced the number of events from 4320 to 2103. This is a significant reduction, but far more than the 815 earthquakes surviving the requirement for inversion of the final model (see Chapter 2).

a)



b)

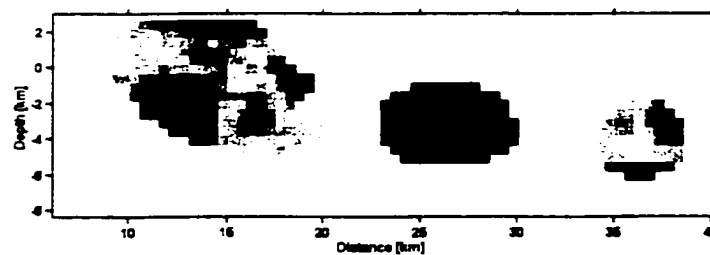


Figure 5.2: Map (a) and cross-section (b) of b -value variation in space for earthquakes located between July 1995 to November 1999. The b -value is determined using the standard AVO velocity model.

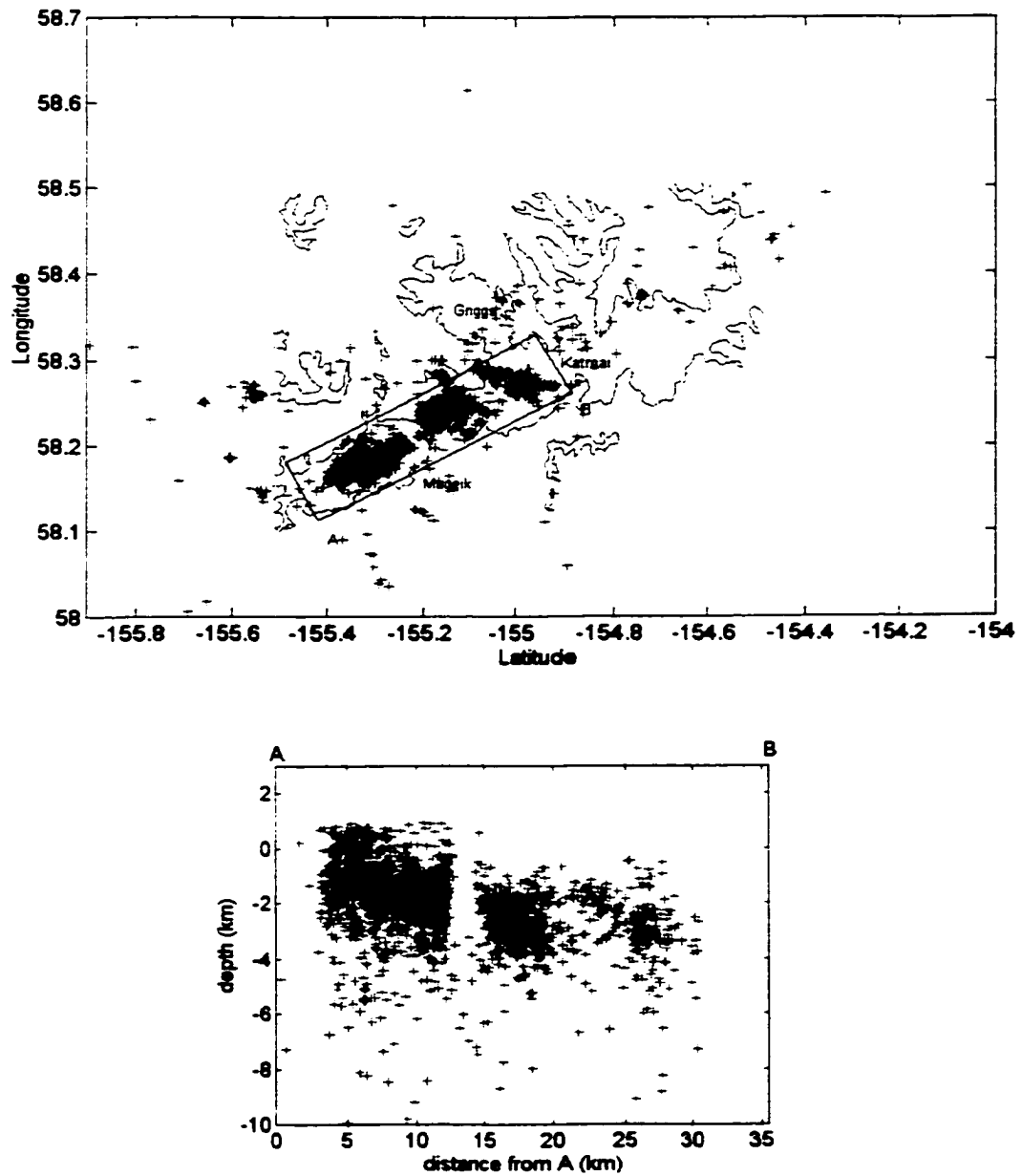
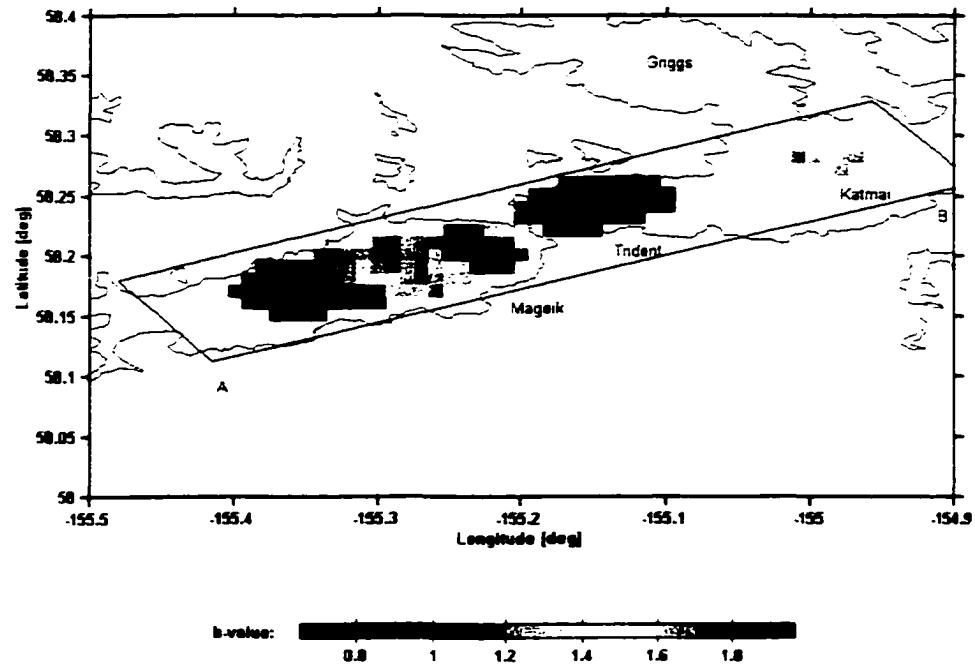


Figure 5.3: Map and cross-section for relocation of earthquakes using the final three-dimensional velocity model. Earthquakes required 5 P phases and an azimuthal gap of less than 300 degrees for inclusion.

Results of the earthquake relocation include a strong shift in the depths of earthquakes located beneath Martin volcano (Figure 5.1 compared to Figure 5.3). The earthquakes initially locate at depths of -3 km to 2 km below sea level. The relocated hypocenters plot between sea level and 5 km below sea level, similar to the depth range for seismicity located beneath Mageik, Trident and Katmai caldera. For 815 high quality earthquakes (see Chapter 2), the relocation reduced the average RMS from 0.18 (Section 2.2.1) to 0.13 seconds, an improvement of 27% over the standard model (Section 2.4). In addition, the relocation eliminated an artifact caused by earthquakes located 1 km above sea level (Chapter 4.2). The source of this artifact is unclear, but the location algorithm HYPOELLIPSE (Lahr, 1989) tries a location with depths of -1.0 km as an initial starting point for earthquake locations. If this starting point has a very low initial RMS travel-time for its solution, then it is accepted as the best solution. The elimination of this artifact, reduced RMS, and improved earthquake clustering suggests that the relocation is more robust and improved over the standard model locations.

Comparison of the *b*-value maps calculated with the standard model (Figure 5.2) and the new model (Figure 5.4) show that the *b*-values have not changed significantly for the Mageik, Trident and Katmai clusters. The *b*-value calculated at Martin volcano, however, is significantly different after relocation. At Martin volcano, the relocation causes a strong change in the *b*-value. Low *b*-values (<1) observed at shallow depth for the standard model locations are eliminated with new model locations (Figure 4.6) and

a)



b)

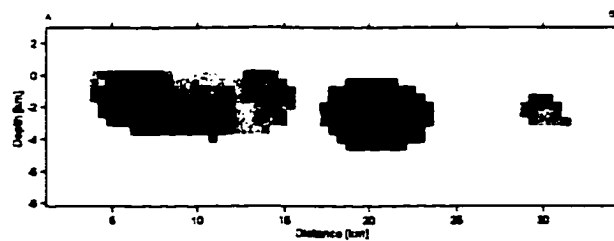


Figure 5.4: Map (a) and cross-section (b) of b -value variation in space for earthquakes located between July 1995 to November 1999. The b -value is determined using the final three-dimensional velocity model.

high b -values resolved at 0-3 km depth are reduced from 1.5-2.0 to about 1.0-1.5 after relocation. Results show that earthquake relocations can change the character of b -value spatial map and stress the importance of high quality earthquake locations for b -value spatial mapping studies.

5.4 Temporal analysis of b -values and maximum depths of seismicity

At Martin and Mageik volcanoes, a temporal variation of the b -value was observed in conjunction with a variation in the maximum depth of seismicity (Figure 4.7). These variations were reexamined using additional earthquakes, higher quality locations and an analysis of the differential b -value to determine if the observation might result from a spatial variation. At Martin and Mageik, almost 700 earthquakes were available for analysis after relocating hypocenters and eliminating earthquakes smaller than the magnitude of completeness ($0.7 M_L$). With relocation, the earthquakes ranged in depth from about 1 km above sea level to about 4 km below sea level (Figure 5.3) with isolated events at greater depths.

With the new velocity model and relocated hypocenters, the fundamental observations persist: increased depths of seismicity associated with the October 1996 swarm coincide with increasing b -values (Figure 5.5). It is noted however that the number of deep events in the relocation is very small: Only three events remain below 7 km depth during the October 1996 swarm. Based on the small number of events, the depth change results should be viewed with caution. The temporal change in b -values is

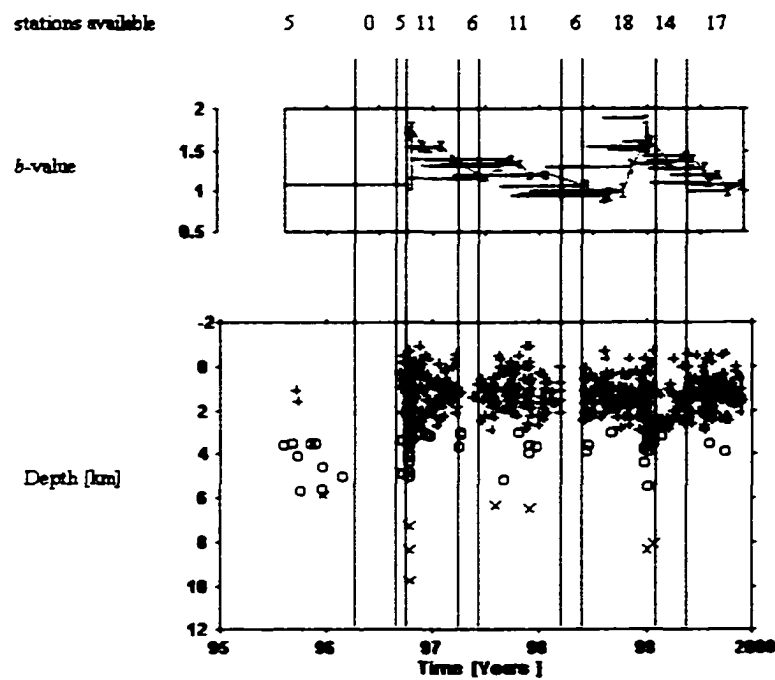


Figure 5.5: Depth versus time and b -value versus time for the period July 26, 1995 to November 30, 1999. Martin-Mageik cluster seismicity is located with three-dimensional velocity model (Chapter 2). Earthquakes required 5 P-phases for inclusion in the relocation.

noted to occur on the scale of the Martin-Mageik cluster. The majority of events during the October 1996 swarm occurred beneath Mageik volcano. Analysis of the differential b -value revealed that most of the earthquakes associated with the October 1996 swarm seismicity occur about 1-2 km from the pre and post swarm seismicity. The difference in locations suggests that the observed temporal b -value anomaly instead may result from a spatial change.

In late December 1998, a second smaller swarm occurred beneath Martin-Mageik volcanoes (Figure 5.5). The December swarm contained about 76 earthquakes and the largest event had a magnitude of 2.6. The b -value and maximum depths of seismicity for the December, 1998 swarm show the same character and polarity as the swarm on October 1996. Again the number of events at depths greater than 7 km is small: only two earthquakes are located at greater depth. The data suggest that the swarms might represent an influx of pressurizing fluid, which lowered the effective stress on fractures, induced seismicity in a high b -value region, and extended seismicity to greater depths.

5.5 Discussion

Spatial b -value mapping has become a standard tool for the examination of subsurface structures in volcanic (Wiemer and McNutt, 1997; Wyss et al., 1997; Power et al., 1998; Wiemer et al., 1998) and tectonic regions (Wiemer and Benoit, 1996; Weimer and Wyss, 1997). Most often, the method has relied on careful selection of earthquakes

located with one-dimensional velocity models. New results suggest that the b -value mapping technique can resolve b -value anomalies with greater accuracy if a higher resolution velocity model, such as the three-dimensional velocity model from Chapter 2, is incorporated into the location process.

The strong shift in hypocenters (Figure 5.3 compared to Figure 4.2) and associated b -value anomalies (Figure 5.4 compared to Figure 5.2) probably occur as a result of previously unmodeled velocity perturbations. The unmodeled perturbation might systematically shift earthquake locations based on magnitude because smaller earthquakes contain a different subset of raypaths than larger earthquakes from the same source area.

As a general example, consider a small (M_L 0.8) and larger (M_L 3.0) earthquake located at Martin volcano using the standard one-dimensional velocity model and an unmodeled velocity perturbation located at Katmai Pass (~10 km distant). The small magnitude earthquake might have sufficient energy to be recorded 30 km from the source and the phase arrival will be recorded at about 10 near stations. For this earthquake, three of the ten stations might be influenced by the unmodeled anomaly (say KCE, KCG, and KABR) causing a bias in the location. Next, consider the large (M_L 3.0) magnitude earthquake. Its location will be determined using more stations because it has more energy traveling to more distant stations. If the event is located on all available stations, then the velocity perturbation will have a much smaller influence (say 3 of 18 arrival times) on the location. Then for many earthquakes in a source region, the larger earthquakes of the distribution might be systematically shifted with respect to the location of smaller earthquakes and this systematic shift might produce an anomalous b -value

distribution. Such anomalies have been generated from synthetic frequency-magnitude distributions originating at a point source and modified by a local velocity perturbation (Jolly et al., 1996).

At Martin volcano, b -values calculated with the standard model are lower at shallow depth and higher at greater depths (Figure 5.2b). The low b -values at shallow depth imply a depletion of small magnitude earthquakes relative to large magnitude events and an enrichment of small magnitude earthquakes at greater depth. Based on these observations, it is surmised that the unmodeled low velocity anomaly at Katmai Pass forced the small earthquakes systematically deeper and further away from the anomaly relative to larger magnitude earthquakes.

Alternatively, a subset of the earthquakes might have insufficient arrival time information to iterate off the location trial depth of 1.0 km above sea level. Such a pathological effect might produce the b -value shift observed. However, a significant number of Martin earthquakes are not located at 1 km above sea level and are not unusual compared to other upper-crustal seismicity in the area. The anomalous earthquakes also occur above Mageik and Trident volcano in significant numbers (Figure 5.1). Martin volcano has 5 seismograph stations within 10-15 km, a station distribution as good or better than other Katmai volcanoes in the study area. Based on the distribution of stations, it is expected that earthquake locations at Martin volcano should be of the same quality as its neighbors. Regardless, this analysis demonstrates the need for better earthquake locations in seismological studies. This relocation study is shown to highlight regions where b -value anomalies are stable (Trident, Mageik, Katmai) under different

velocity models, and regions (Martin) where the *b*-value anomalies are shown to change. Based on lower RMS travel-time residuals and removal of the location artifact, the associated *b*-value images are judged to be improved over the version offered in Chapter 4.

5.6 References

Jolly, A.D., McNutt, S.R., Wiemer, S. and Lahr, J.C., An evaluation of spatial *b*-value mapping techniques based on an analysis of seismicity at Mt. Spurr, Alaska, and synthetic data, EOS Trans. Amer. Geophys. U., 77, 514, 1996.

Lahr, J.C., HYPOELLIPSE/Version 2.0: A computer program for determining local earthquake hypocentral parameters, magnitude, and first motion pattern: U.S Geol. Surv., Open-File Report, 89-116, 89p., 1989.

Power, J.A., Wyss, M., Latchman, J.L., Spatial variations in the frequency-magnitude distribution of earthquakes at Soufriere Hills volcano, Montserrat, West Indies, Geophys. Res. Lett., 25, 3653-3656, 1998.

Wiemer, S. and Benoit, J., Mapping the *b*-value anomaly at 100 km depth in the Alaskan and New Zealand subduction zones, Geophys. Res. Lett., 23, 1557-1560, 1996.

Wiemer, S. and McNutt, S.R., Variations in the frequency magnitude distribution with depth in two volcanic areas: Mount St. Helens, Washington, and Mt. Spurr, Alaska, *Geophys. Res. Lett.*, 24, 189-192, 1997.

Wiemer, S. and Wyss, M., Mapping the frequency-magnitude distribution in asperities; An improved technique to calculate recurrence times, *J. Geophys. Res.*, 102, 15115-15128, 1997.

Wiemer, S., McNutt, S.R., and Wyss, M., Temporal and three-dimensional spatial analysis of the frequency-magnitude distribution near Long Valley caldera, California, *Geophys. J. Int.*, 134, 409-421, 1998.

Wyss, M., Shimazaki, K. and Wiemer, S., Mapping active magma chambers by *b*-values beneath the Off-Ito volcano, Japan, *J. Geophys. Res.*, 102, 20413-20422, 1997.

Chapter 6: Integrated analysis of the *b*-value, P-wave velocity and P-wave attenuation

6.0 Introduction

In prior chapters, separate methods for examining the subsurface structure (*b*-values, P-wave velocity and P-wave attenuation) were applied to the Katmai volcanoes. Interpreted individually, the methods are useful, but provide an incomplete and unconstrained picture of the subsurface structure. Together, the methods are highly complementary, and provide strong evidence in support of magma resident at shallow depth beneath Mageik and Trident volcanoes. The methods use double couple (elastic failure) earthquakes to measure properties of the earth. However, the *b*-value spatial mapping technique measures those properties at the source, and P-wave velocity and attenuation methods measure those properties along the path. A consequence of this difference is illustrated in Figure 2.2 and 2.3 compared to Figure 5.4. The tomographic method provides interpretable images from a much larger portion of the earth, even though the methods were drawn from the same datasets. This advantage is offset by the computational expense associated with tomographic methods. The CPU cycles required for this tomographic analysis were at least an order of magnitude greater than for the *b*-value study. In addition, spatial mapping via the *b*-value has an advantage in error estimation because the earthquake frequency-magnitude distribution obeys a power law, allowing standard regression statistics (Wiemer and McNutt, 1997) and testing (Utsu,

1992). Errors associated with tomographic techniques are not as straightforward, a consequence of the non-linearity and approximate nature of the inversion technique.

6.1.0 Variations in the frequency-magnitude distribution

Double-couple earthquakes common to both tectonic and volcanic environments obey the frequency-magnitude relation given by

$$\text{Log } N = a - Mb \quad 6.1$$

where a is the total number of earthquakes in the distribution, N is the total number of earthquakes at and above the magnitude M , and the b describes the slope. The b -value is known to vary systematically with applied shear stress (Scholz, 1968), material heterogeneity (Mogi, 1962), temperature gradient (Warren and Latham, 1970) and effective stress (Wyss, 1973). Recent computational advances have made analyses of b -values in space (Wiemer and Benoit, 1996; Wiemer and McNutt, 1997), and time (Wiemer et al., 1998) routine. These analyses showed that large variations in the frequency-magnitude distribution occur over small spatial scales and that the variations can be ascribed to one or more mechanisms.

6.1.1 Velocity in the volcanic environment

Like frequency-magnitude distributions, the P-wave velocity is highly variable in the earth's crust. Despite a large number of papers showing observations in volcanic environments (e.g. Lorenzen, 1994; Benz, et al., 1996; Okubo et al., 1997; Power et al., 1998, Moran, 1997), little is known about the physics under which the velocity varies. As stated in Chapter 2, the P-wave velocity is given by

$$\alpha = [(\kappa + (4\mu/3))/\rho]^{1/2} \quad 6.2$$

where κ is the bulk modulus, μ is the rigidity, and ρ is the density. Examination of Equation 6.2 shows that liquids, which do not support shear, will cause a reduction in rigidity and consequent reduction in elastic wave velocity. This simplistic approach is confirmed by theoretical analysis by Mavco, (1980) who showed for olivine and pyroxene that a 10% partial melt of magma could produce 10-40% reduction on the P-wave velocity. Ito et al. (1979) showed that the velocity of rock decreased under conditions of low pore pressures where steam exists. Under conditions of higher pore pressures, where liquid and steam coexist, the velocity decreased, but not strongly. Further saturation of the fractured system caused the velocity to increase as pore fractures are completely filled. The later observation can be understood because under conditions of increased pore fluid pressure, voids in the rock are filled with fluid and become less compressible, hence increasing the bulk modulus (Equation 6.1 above) (Lorenzen, 1994).

6.1.2 Attenuation and volcanoes

Many studies of the frictional attenuation of the earth's crust have been undertaken over the past 30 years. Ito et al. (1979) showed experimentally that strong attenuation is associated with low pore pressure conditions where steam exists. Such conditions probably apply to the upper kilometer or two of the crust (Evans and Zucca, 1988; Zucca and Evans, 1992). At greater depths and higher confining pressures, fluid saturated rocks might dominate producing higher attenuation than their unsaturated counterparts (Toksoz et al., 1979). Studies by Volarovitch and Gurevich (1957) and Gordon and Davis (1968) showed that attenuation is independent of temperature, at temperatures low relative to the melting point. At higher temperatures, Mavco (1980) showed that the P-wave attenuation should increase with increased partial melting. This is confirmed in low temperature laboratory experiments (Gao et al., 1993), where strong attenuation resulted in simulations of partial melting using aluminum-gallium mixtures.

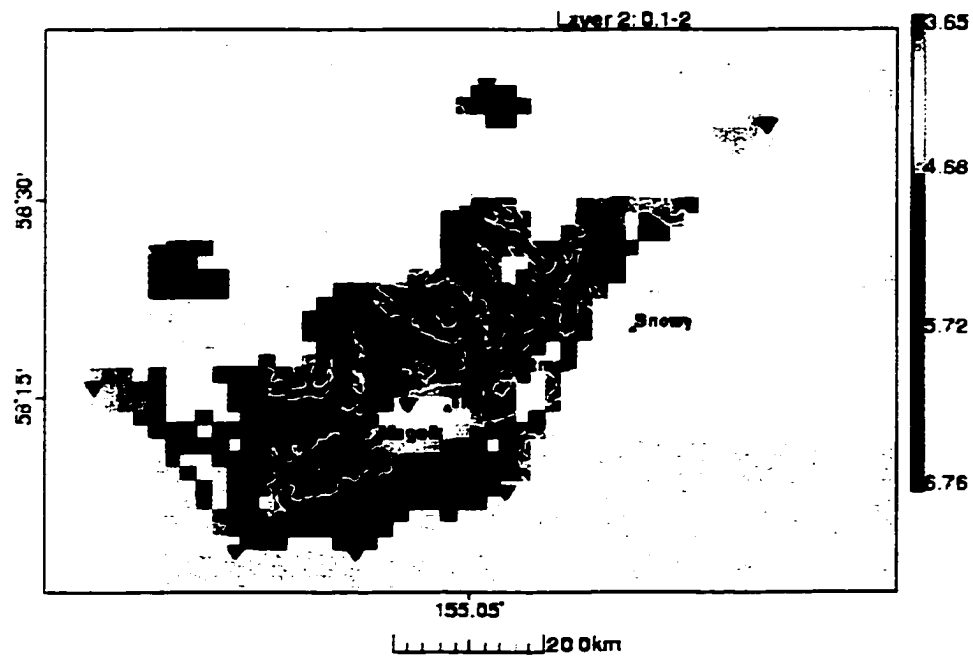
6.2 Integrated analysis

The three parameters of this study are integrated to determine the subsurface structure beneath the Katmai volcanoes. The integration is completed by first re-plotting velocity, attenuation and *b*-value results from Chapters 2, 3 and 5 (Figures 6.1-6.4). Associated cross-sections for the velocity (Figures 6.5a), attenuation (Figures 6.5b) and

the b -value (Figure 6.5c) are projected from a section along the volcanic axis (box in Figure 4.2). Finally, the dominant features of each cross-section in Figure 6.5 are integrated into a generalized cross-section (Figure 6.6). These integrated features are tested against competing theoretical, laboratory, and field observations resulting in a consistent and realistic interpretation of the subsurface structure. Results of the integration include; 1) normal velocity and attenuation observed outboard of the volcanoes (Figure 6.1-6.4), 2) a zone of moderately low velocities and moderately high attenuation between Martin volcanoes and Katmai caldera at depths less than 6 km (dotted rectangle, Figure 6.6), 3) lowest velocities and highest attenuation observed between Mageik, Novarupta and Trident volcanoes at depths of 0-4 km (Figures 6.5-6.6) and 4) high b -values at Mageik volcano and low b -values at Trident volcano.

The velocity and attenuation anomalies probably cannot be ascribed to simple lithologic variations. In the study area, surface rocks are dominantly Jurassic Naknek Formation (sand and siltstones), except along the volcanic axis, where andesite, dacite and rhyolite predominate. The thickness of the Naknek Formation rocks is poorly constrained, but is probably on the order of 1.5 km thick (Hildreth, 1987). The Naknek Formation is underlain by Mesozoic sedimentary and volcanic rock having an approximate thickness of 3.5 km (Hildreth, 1987). The underlying basement rock is probably composed of meta-sedimentary and plutonic rocks (Beikman, 1980). If the rocks outboard of the volcano are predominantly sedimentary and the rocks along the volcanic axis are predominantly volcanic, then the question is, what is the expected

a)



b)

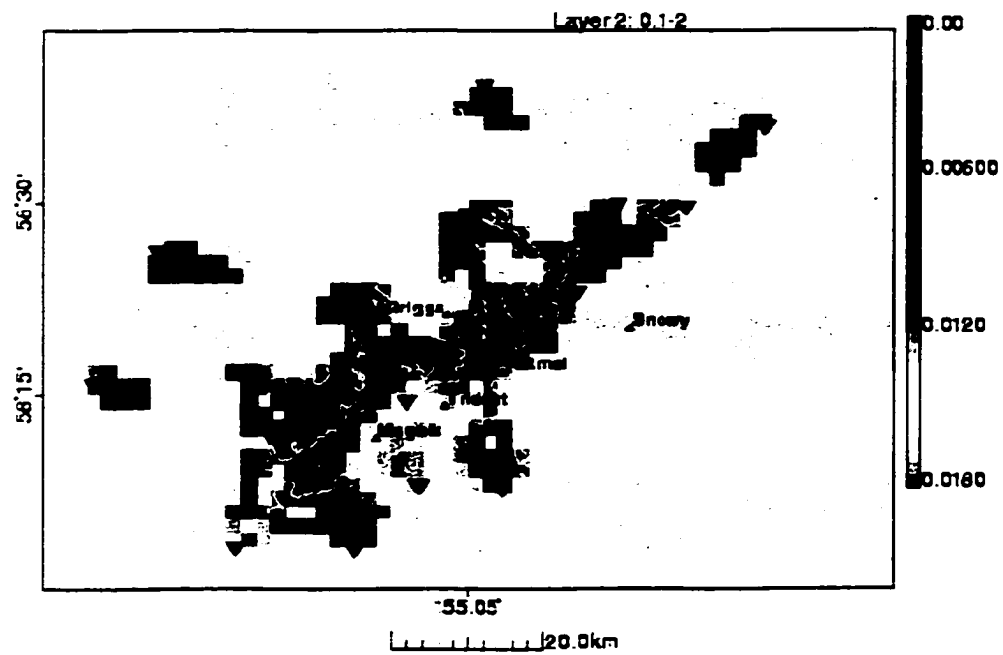
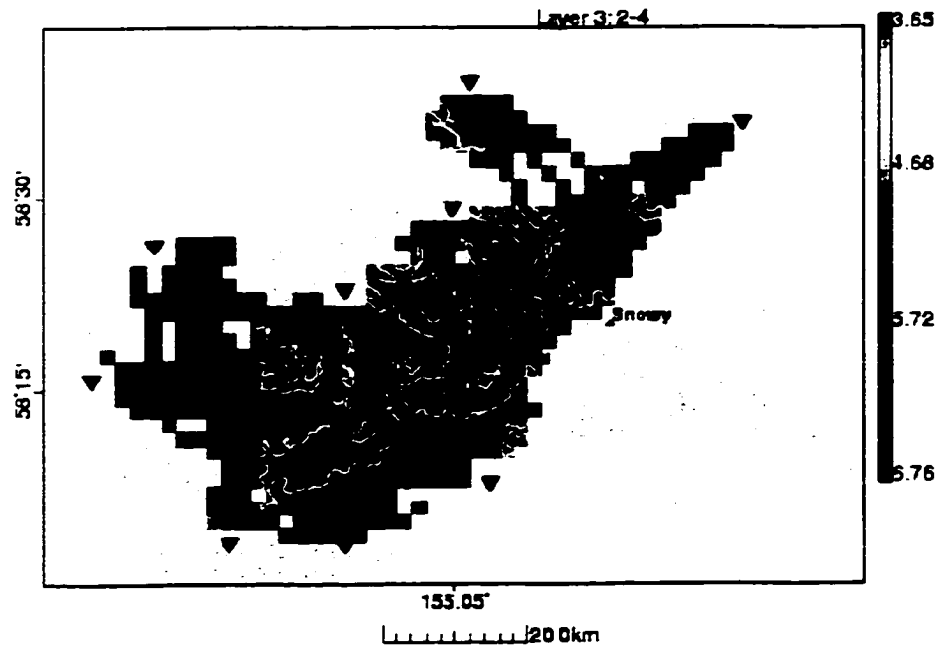


Figure 6.1: Velocity (a) and attenuation (b) for layer 2 (0.0-2.0 km). Color scale is km/s (a) and $1/Q$ (b).

a)



b)

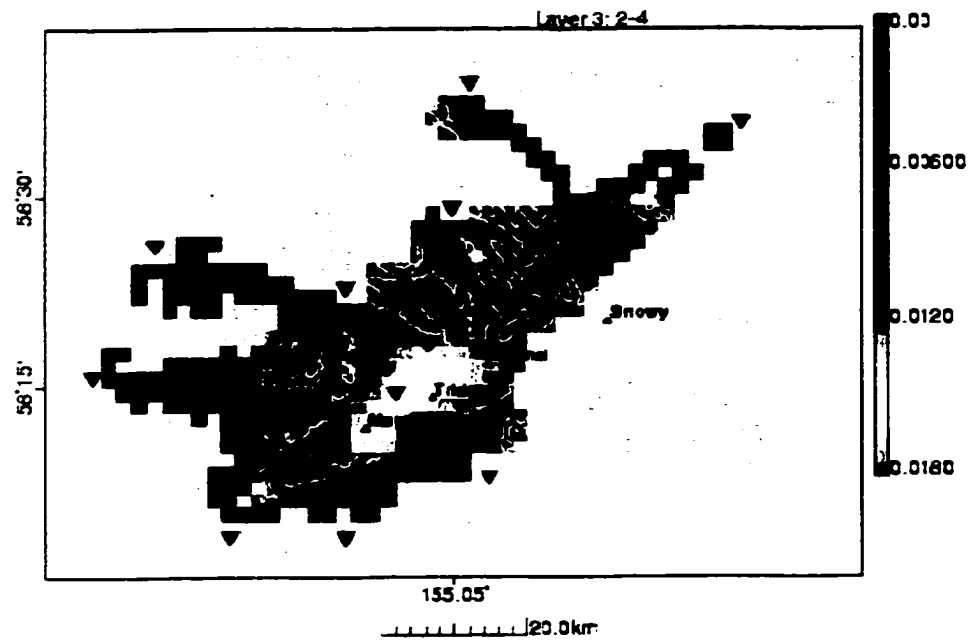
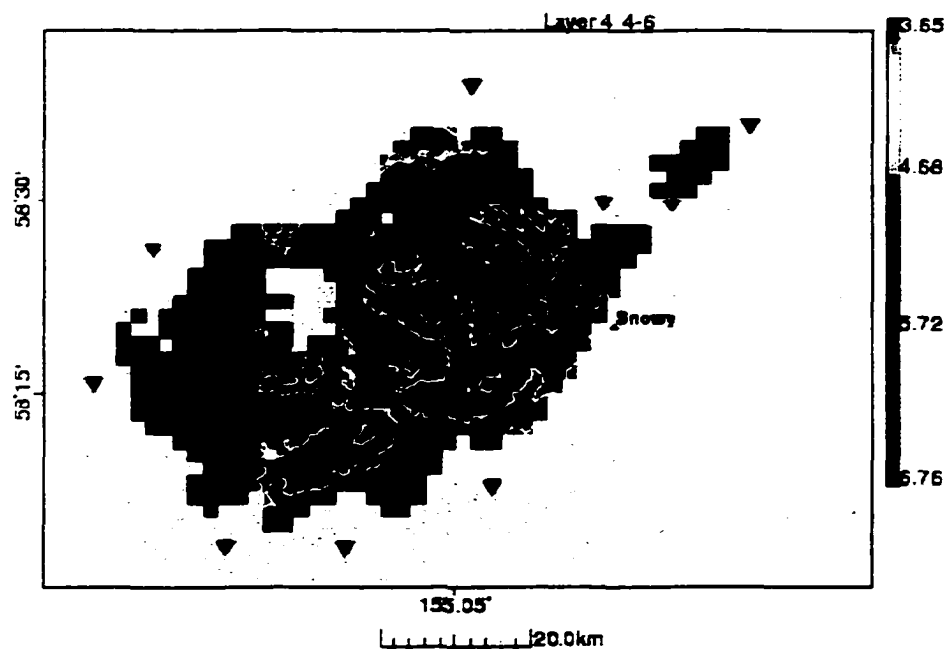


Figure 6.2: Velocity (a) and attenuation (b) for layer 3 (2.0-4.0 km). Color scale is km/s (a) and $1/Q$ (b).

a)



b)

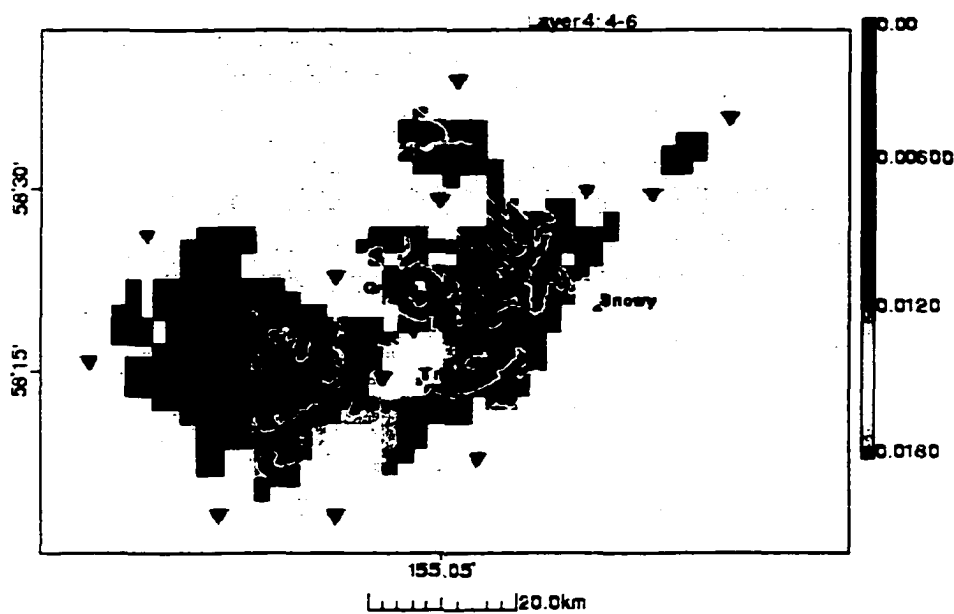


Figure 6.3: Velocity (a) and attenuation (b) for layer 4 (4.0-6.0 km). Color scale is km/s (a) and $1/Q$ (b).

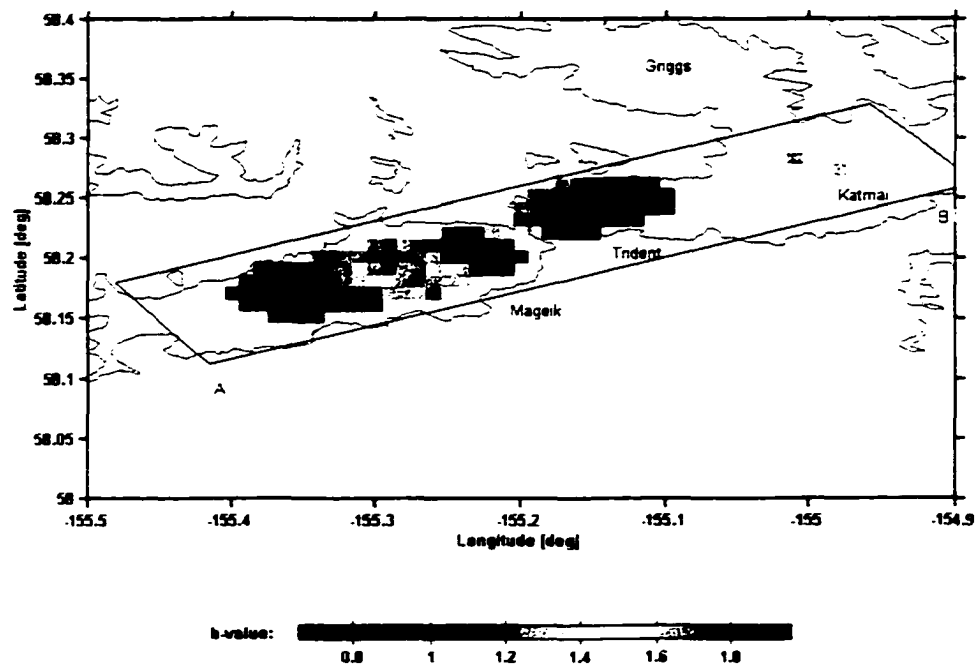


Figure 6.4: Map of b -value variation in space for earthquakes located between July 26, 1995 and November 30, 1999. Grid spacing is approximately 0.5 km by 0.5 km. Locations are determined using the final three-dimensional velocity model. The b -value is determined in variable volume cylinders having 100 earthquakes $> 0.7 M_L$.

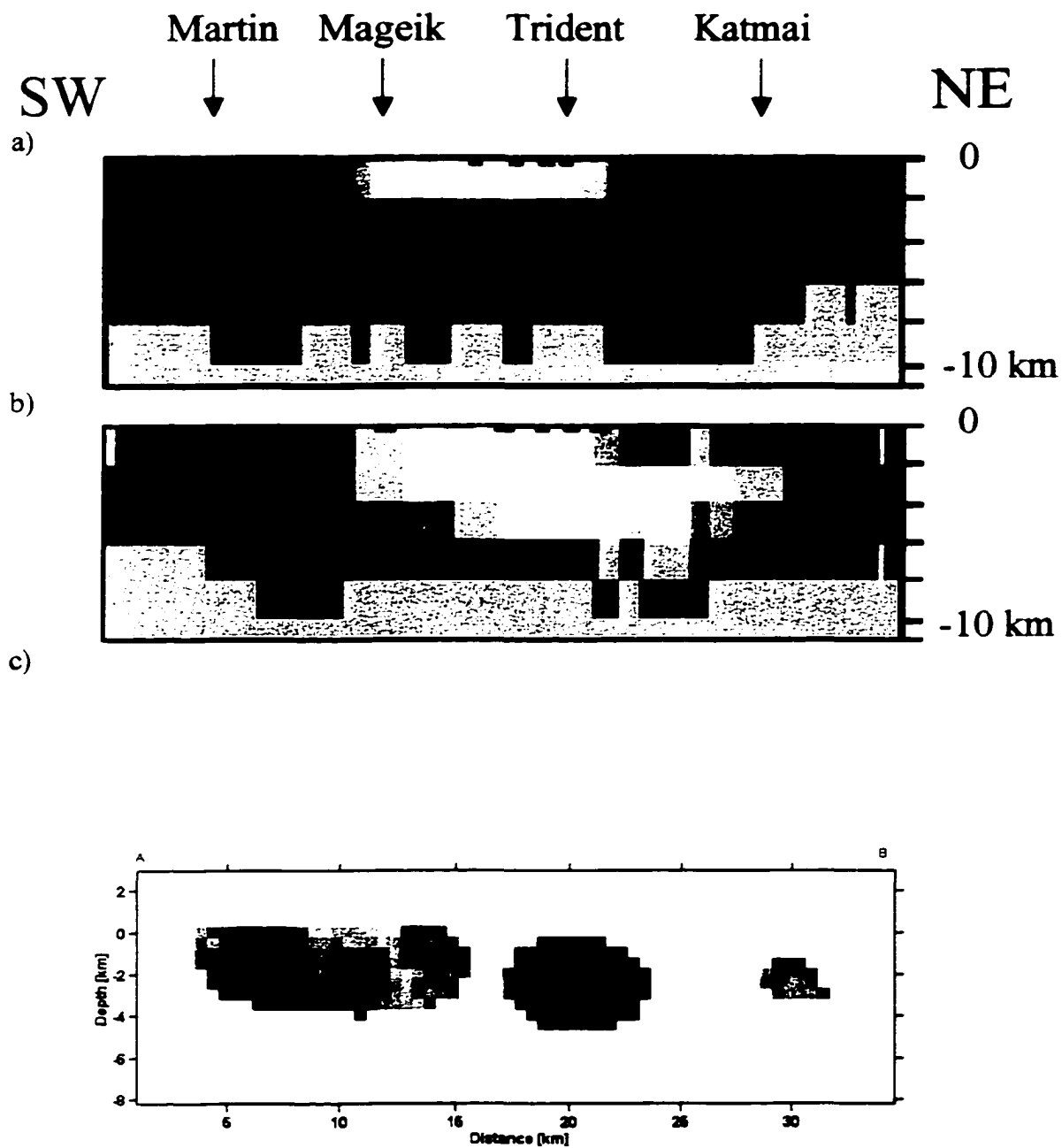


Figure 6.5: Cross-sections along the volcanic axis from Martin to Katmai caldera for velocity (a), attenuation (b), and b -value spatial mapping (c). Color scales are given in Figures 6.1-4.

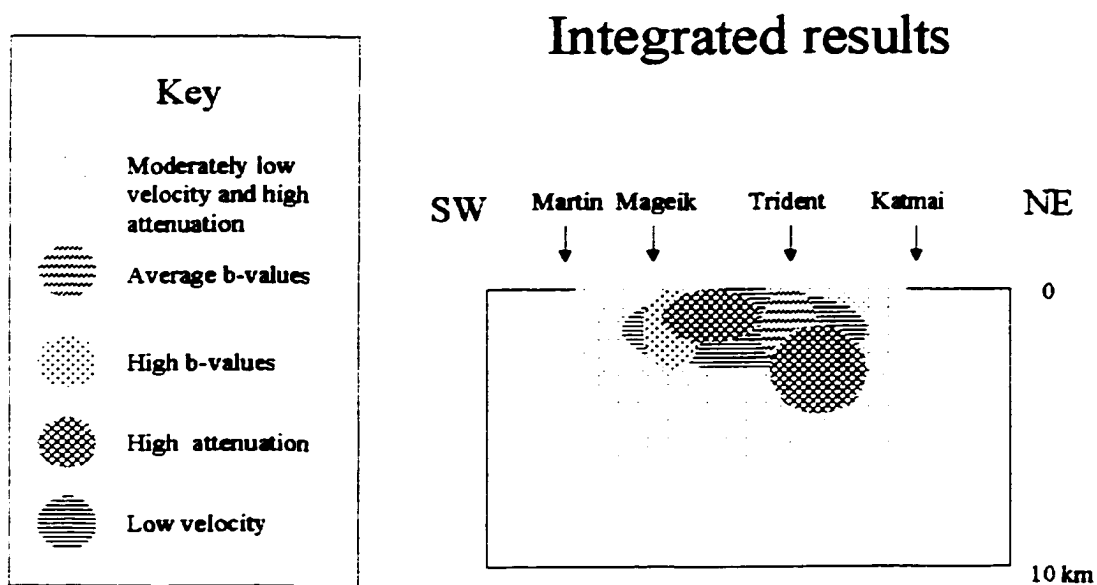


Figure 6.6: Integration of velocity, attenuation, and b -value results for cross-section along volcanic axis.

velocity distribution? Examination of velocities of common rock types at relevant confining pressures of about 1 kbar (Handbook of physical properties of rocks, v. 2, 1982, and references therein) suggest velocities of 3.95-5.29 km/s for sandstones and siltstones. Alternatively, a single measurement of the velocity of andesite at the same confining pressure yields a velocity of 5.27 km/s. These limited data suggest that the volcanic rocks at Katmai should have faster or similar P-wave velocities compared to sandstones and siltstones observed outboard of the volcanic axis. Hence, lithologic variations probably cannot account for the observations.

The observations near the surface could indicate the existence of a shallow hydrothermal system. Power et al, (1998) showed that a strong low velocity anomaly occurred beneath an active geothermal system at Spurr volcano, Alaska. Such a geothermal system might produce high attenuation and low velocities in the first kilometer or so below the surface (Evans and Zucca, 1988). Fumarolic activity is observed at Trident, and Mageik consistent with this hypothesis. However, it is not likely that these effects extend to greater than a kilometer or two below the surface where higher confining pressures preclude the existence of steam in pores and fractures.

Prior experimental and theoretical studies suggest that the presence of partially melted rock at depths greater than a few kilometers below the surface will result in higher b -values, lower relative velocities, and increased attenuation. Alternatively, a solid with fractures filled with water might produce higher attenuation, moderately lower velocities and higher b -values. Such conditions are likely in volcanic environments and could produce the results of Figure 6.6 from about 2-6 km below sea level.

Moderately low velocities and associated moderate attenuation occur along the volcanic axis between the surface and 6 km below sea level (rectangle, Figure 6.6). These observations probably result from higher fracture density, higher water content, and perhaps residual melt in old intrusions. Repeated intrusions may have deformed and fractured the rocks in the immediate vicinity of the volcanic axis. This high fracture density, and an inferred abundance of water from overlying glaciers and degassing magmas may have produced a general trend of lower velocity and higher attenuation between Martin volcano and Katmai caldera.

Beneath Mageik, Novarupta and Trident volcanoes, a zone of higher attenuation and lower velocities exist. This zone has stronger anomalies than observed along the general volcanic axis and the subsurface conditions are probably different there. If the observations result from a magma system at shallow depth (i.e. 0-6 km depth), then what is the character of this magma system? Based on work by Mavco (1980) one might expect the shallow magma chamber to contain anywhere from 10-40% melt based on the ~10% reduction in velocities. If the body contained 10% partial melt for the extent of the system and the dimensions of the magma body are 15 km (Katmai caldera to Mageik) by 10 km (Novarupta to Observation mountain) and extend from sea level to 6 km below sea level, then the total portion of magma within the observed anomaly would be $\sim 90 \text{ km}^3$ (10% of the total velocity and attenuation anomaly of 900 km^3). Hildreth et al. (1983) determined a total volume for the 1912 eruption of about 13 km^3 (dry rock equivalent). Given the estimates of partial melt and the distribution of the observed structure, it is

surmised that the 1912 eruption could have been fed by this inferred magma system, but probably could not have produced the collapse at Katmai caldera located ~10 km away.

A further indication of the character of the inferred magma system is supplied by our *b*-value analysis. The bulk of the data for the *b*-value calculation at Mageik volcano come from two swarms: one during the 1996 October swarm and the second associated with the December 1998 swarm (Figures 4.7 and 5.5). The highly localized nature of the swarms suggests that a single magma chamber between Martin and Trident is unrealistic. The volume occupied by the swarm itself is less than about 15 km³, about 2% of the volume occupied by the velocity and attenuation anomaly (900 km³). Instead, the swarms and associated *b*-value anomalies are restricted to one small part of the velocity and attenuation anomaly suggesting multiple intrusions rather than a single chamber. This inference is further supported by results by Lu et al. (1997). The deformation signature they observed was modeled as a Mogi point source located at shallow depth and on the south-west flank of Trident volcano. Lu et al.'s (1997) anomaly is basically centered on the velocity and attenuation anomalies of this study (Figure 6.6). The results are also coincident with results by Coombs et al., (in press) which suggest that Trident eruptive products were derived from shallow depth.

High *b*-values at Mageik volcanoes and low *b*-values at Trident volcano offer an interesting conundrum. Why do two regions where magma is inferred to exist have such completely different frequency-magnitude distributions? The variation might be ascribed to the timing of the intrusive event. The high *b*-values associated with the Mageik *b*-value anomaly are associated with the two swarms in October 1996 and December 1998

(Figure 5.5), while the most recent intrusion at Trident may have occurred earlier, between 1993 and 1995 (Lu et al., 1997). Perhaps high b -values are observed immediately after an intrusive event while the attenuation and velocity results are longer-lived features.

The evidence suggests that at least two younger magma chambers exist. The most recently active one is beneath Mageik volcano, while the second magma chamber is beneath Southwest Trident and was probably last intruded between 1993-1995 (Lu et al., 1997). A generalized cartoon cross-section of the Katmai volcanoes (Figure 6.6) shows the main subsurface features.

The depth and extent of subsurface features at Katmai is not well resolved because parameters of this study are limited to the region above 8 km depth. Prior geophysical results, however, suggest that the volcanic system at the Katmai group volcanoes extends to far greater depth. For example, gravity results obtained by Kienle (1970) were subsequently modeled by Saltus et al. (1991) as a 4.5 km radius sphere centered approximately 7-9 km below sea level and having a density contrast of 500 kg/m³. In addition, Ward, et al. (1991) found a 0.2-0.9 second delay in the arrival times for earthquakes recorded on a station located at Katmai pass. The three-dimensional velocity model in this study (Chapter 2) does not yield this total anomaly. For example, if vertical rays impinged the new three-dimensional velocity structure at Katmai pass compared to a non-volcanic ray path (beneath station ACH for this example), then only about 0.2 seconds of velocity contrast could occur. Additional low velocity material is required and must be located at greater depth. Deeper volcanic structures are also

inferred in a study of S-wave screening (Matumoto, 1971) using local and regional seismicity. The anomalies were centered on Katmai and included 4 bodies, one at depths of 20 to 30 kilometers, beneath Katmai pass and the others at depths less than 10 km and centered at: 1) Martin-Mageik, 2) beneath Trident, Katmai caldera and Griggs, and 3) beneath Snowy volcano.

The prior geophysical results require deeper volcanic structures, while the new attenuation (Chapter 2) results suggest that the anomalous structures do not extend beyond about 6 km depth. The observations suggest that both shallow and deep volcanic systems exist beneath the Katmai volcanoes. This inference is provisional, however, because the critical 6-8 km layer for the attenuation inversion and the 4-8 km layers for the velocity inversion are less well constrained.

6.3 Models for the 1912 eruption

As a final point of discussion, two models for the 1912 eruption were forwarded in recent papers. One, by Hildreth and Fierstein (2000), suggests that a large compositionally zoned magma chamber was resident beneath Katmai caldera, and erupted via a propagating sill and dike at Novarupta dome. The alternate model, by Eichelberger and Izbekov (2000) suggests that a large rhyolite dike intruded both a shallow dacite-andesite magma chamber beneath Mount Katmai and the surface at Novarupta, producing the large eruption, and caldera collapse. How do these models compare with the new velocity, attenuation and *b*-value results? The Hildreth and Fierstein (2000) model

requires a large magma chamber beneath Katmai caldera. If such a chamber existed at the beginning of the 20th century, it is reasonable that some manifestation should be seen in the subsurface structure today. If so, then it is only imaged as a generalized feature of the volcanic axis (Figure 6.6). Unfortunately, the region in question is on the edge of both the velocity and attenuation models (Figures 2.5, 2.7, 2.9, 3.14, 3.16 and 3.18) and might exist, yet remain unresolved. A dike of the nature proposed by Eichelberger and Izbekov (2000) is probably not resolvable by the techniques described in this thesis. However, the smaller scale magma chamber, proposed in the alternate model, might produce the moderately low velocities and moderately high attenuation seen in the vicinity of Katmai caldera.

One interesting aspect of both models could be expressed in the attenuation result of Chapter 3. The dike structure common to both models must have propagated through undeformed rock before reaching the new vent at Novarupta. This feature is expressed in Figure 6.6 as the deeper (2-6 km) high attenuation structure beneath Trident volcano. Inspection of the layer 3 attenuation results (Figure 6.3b) shows that the high attenuation structure is centered beneath Novarupta dome (Figure 6.3b) and is not related to a strong velocity anomaly (Figure 6.3a). The strong attenuation and low velocity feature might result from a solidified dike and fault system common to both the Hildreth and Fierstein (2000) and Eichelberger and Izbekov (2000) models. The highly fractured zone probably contains no resident magma, having been long solidified and never re-injected, hence producing only marginally low velocities. However, the region beneath Novarupta may contain abundant fluid filled cracks, producing the strong attenuation result.

6.4 Conclusions

This thesis uses established techniques for estimating the P-wave velocity (Lees, 1989, Moran 1997), P-wave attenuation (Witlinger et al. 1983; Lees and Lindley, 1994), and b -value (Wiemer and Benoit, 1996; Wiemer and McNutt, 1997) structure in three-dimensions at the Katmai group of volcanoes. Results of these studies indicate that low velocities and high attenuation occur beneath Mageik, Novarupta, Trident and Katmai caldera in the depth range 0-4 km below sea level at this same depth range, high b -values are observed beneath Mageik volcano, intermediate b -values are observed beneath Martin and Katmai caldera and low b -values are observed at Trident volcano. The P-wave velocity (Chapter 2) and attenuation (Chapter 3) studies in conjunction with prior gravity (Kienle, 1970), and S-wave attenuation results (Matumoto, 1971) demonstrate the existence of a large shallow subsurface structure extending from Mageik volcanoes to Katmai caldera. This structure is probably composed of several smaller scale structures, as indicated by the localized character of the b -value distributions (Chapter 4 and 5) and prior deformation results (Lu et al., 1997). The totality of the data suggest that the Katmai volcanoes between Mageik and Trident are underlain by a series of partially molten magma bodies which are isolated from each other, at least within the time scale of the geophysical data used for this interpretation (i.e. 1970-2000).

6.5 References

Beikman, H.M., Geologic map of Alaska, Dept. of Interior-U.S. Geol. Surv., 1980.

Benz, H.M., Chouet, B.A., Dawson, P. B., Lahr, J.C., Page, R.A., and Hole, J.A., Three-dimensional P and S wave velocity structure of Redoubt volcano, Alaska, *J. Geophys. Res.*, 101, 8111-8128, 1996.

Coombs, M.L., Eichelberger, J.C. and Rutherford, M.J., Magma storage and mixing conditions for the 1953-68 eruption of Southwest Trident volcano, Katmai National Park, Alaska, *Bull. Volcanology*, in press.

Eichelberger, J.E. and Izbekov, P.E., Eruption of andesite triggered by dyke injection: contrasting cases at Karimsky volcano, Kamchatka and Mt. Katmai, Alaska, *Phil. Trans. R. Soc. Lond. A.*, 358, 1465-1485, 2000.

Evans, J.R. and Zucca, J.J., Active high-resolution tomography of compressional wave velocity and attenuation structure at Medicine Lake volcano, Northern California Cascade range, *J. Geophys. Res.*, 93, 15016-15036, 1988.

Gao, L.S., Poirier, J.P., and Aki, K., Attenuation due to partial melting: An experimental study on a model system, using the lab coda method, *J. Geophys. Res.*, 98, 1853-1860, 1993.

Gordon, R.B. and Davis, L.A., Velocity and attenuation of seismic waves in imperfectly elastic rocks, *J. Geophys. Res.*, 73, 3917-3935, 1968.

Handbook of physical properties of rocks, V. 2, 1982, R.S. Chermichael ed., CRC Press Inc., Boca Raton, Fl.

Hildreth, W, The compositionally zoned eruption of 1912 in the Valley of Ten Thousand Smokes, Katmai National Park, Alaska, *J. Volc and Geotherm. Res.*, 18, 1-56, 1983.

Hildreth, W, New perspectives on the eruption of 1912 in the Valley of Ten Thousand Smokes, Katmai National Park, Alaska, *Bull. Volcanology*, 49, 680-693, 1987.

Hildreth, W and Fierstein J, Katmai volcanic cluster and the great eruption of 1912, *Geol. Soc. Amer. Bull.*, 112, 1549-1620, 2000.

Ito, H., DeVilbiss, J. and Nur, A., Compressional and shear waves in saturated rocks during water-steam transition., *J. Geophys. Res.*, 84, 4731-4735, 1979.

Kienle, J., Gravity traverses in the Valley of Ten Thousand Smokes, Katmai National Monument, Alaska, *J. Geophys. Res.*, 75, 6641-6649, 1970.

Lees, J.M., Seismic tomography in Western Washington, Ph.D. Thesis, 173 p., Univ. of Wash., Seattle, 1989.

Lees, J.M and Lindley, G.T., Three-dimensional attenuation tomography at Loma Prieta: Inversion of t^* for Q , *J. Geophys. Res.*, 99, 6843-6863, 1994.

Lorenzen, R.J.L., Seismic tomography of Redoubt volcano, M.S. Thesis, 78 p. University of Alaska, Fairbanks, AK, 1994.

Lu, Z., Fatland, R., Wyss, M., Li, S., Eichelberger, J., Dean, K., Freymueller, J., Deformation of New Trident Volcano measured by ERS-1 SAR interferometry, Katmai National Park, Alaska, *Geophys. Res. Lett.*, 24, 695-698, 1997.

Matumoto, T., Seismic body waves observed in the vicinity of Mount Katmai, Alaska, and evidence for the existence of molten chambers, *Geol. Soc. Amer. Bull.*, 82, 2905-2920, 1971.

Mavco, G.M., Velocity and attenuation in partially molten rocks, *J. Geophys. Res.*, 85, 5173-5189, 1980.

Mogi, K., Magnitude-frequency relation for elastic shocks accompanying fractures of various materials and some related problems in earthquakes (2nd Paper), Bull. Earthquake Res. Inst., 40, 831-853, 1962.

Moran, S.C., Three-dimensional P-wave velocity structure in the greater Mount Rainier area from local earthquake tomography, Ph.D. Thesis, 168 p., Univ. of Wash., Seattle, 1997.

Okubo, P.G., Benz, H.M., Chouet, B., Imaging the crustal magma source beneath Mauna Loa and Kilauea volcanoes, Hawaii, Geology, 25, 867-870, 1997.

Power, J.A., Villasenor, A., Benz, H.M., Seismic image of the Mount Spurr magmatic system, Bull. Volcanology, 60, 27-37, 1998.

Saltus, R.W, Stone, D.B., Kienle, J., and Goodliffe, A.M., New gravity data at Katmai National Park, Alaska, suggest a magma body analogous to that at Geysers-Clear Lake region, California, EOS Trans. Amer. Geophys. U., 429, 1991.

Scholz, C.H., The frequency-magnitude relation of microfracturing in rock and its relation to earthquakes, Bull. Seis. Soc. Amer., 58, 399-415, 1968.

Toksoz, M.N., Johnson, D.H., Timur, A., Attenuation of seismic waves in dry and saturated rocks: I Laboratory Measurements, *Geophysics*, 44, 681-690, 1979.

Utsu, T., On seismicity, in : Report of cooperative research institute of the statistical mathematics 34, *Mathematical Seismology VII, Annals of the Institute of Statistical Mathematics*, Tokyo, 139-157, 1992.

Volarovitch, M.P. and Gurevich, G.I., Investigation of dynamic moduli of elasticity for rocks in relation to temperature, *Bull. Acad. Sci. U.S.S.R. Geophys.*, 4, 1-9, 1957.

Ward, P.A., Pitt, A.M. and Endo, E., Seismic evidence for magma in the vicinity of Mt. Katmai, Alaska, *Geophys. Res. Letts.*, 18, 1537-1540, 1991.

Warren, N.W. and Latham, G.V., An experimental study of thermally induced microfracturing and its relation to volcanic seismicity, *J. Geophys. Res.*, 75, 4455-4464, 1970.

Wiemer, S. and Benoit, J., Mapping the *b*-value anomaly at 100 km depth in the Alaskan and New Zealand subduction zones, *Geophys. Res. Lett.*, 23, 1557-1560, 1996.

Wiemer, S. and McNutt, S.R., Variations in the frequency-magnitude distribution with depth in two volcanic areas: Mount St. Helens, Washington, and Mt. Spurr, Alaska, *Geophys. Res. Lett.*, 24, 189-192, 1997.

Wiemer, S., Wyss, M. and McNutt, S.R., Temporal and three-dimensional spatial analysis of the frequency-magnitude distribution near Long Valley caldera, *Geophys. J. Int.*, 134, 409-421, 1998.

Wittlinger, H., Haessler, H, Granet, M., Three-dimensional inversion of Qp from low magnitude earthquake analysis, *Annales Geophysicae*, 1, 427-438, 1983.

Wyss, M., Towards a physical understanding of the earthquake frequency distribution, *Geophys. Roy. Astr. Soc.*, 31, 341-359, 1973.

Zucca, J.J and Evans, J.R., Active high-resolution compressional wave attenuation tomography at Newberry volcano, Central Cascade range, *J. Geophys. Res.*, 97, 11047-11055, 1992.